UNIVERSIDADE ESTADUAL DE CAMPINAS
Instituto de Física Gleb Wataghin

Felipe Boechat Mazzi

Microfabrication of Thin-Film Lithium Niobate Waveguides and Ring Resonators

Microfabricação de Guias de Onda e Cavidades Ópticas em Anel em Filmes Finos de Niobato de Lítio

Campinas
2023

Felipe Boechat Mazzi

Microfabrication of Thin-Film Lithium Niobate Waveguides and Ring Resonators

Microfabricação de Guias de Onda e Cavidades Ópticas em Anel em Filmes Finos de Niobato de Lítio

Dissertação apresentada ao Instituto de Física Gleb Wataghin da Universidade Estadual de Campinas como parte dos requisitos exigidos para a obtenção do título de Mestre em Física, na área de Física Aplicada.

Dissertation presented to the Institute of Physics Gleb Wataghin of the University of Campinas in partial fulfillment of the requirements for the degree of Master in Physics, in the area of Applied Physics.

Supervisor/Orientador: Prof. Dr. Felippe Alexandre Silva Barbosa

ESTE TRABALHO CORRESPONDE À VERSÃO FINAL DA DISSERTAÇÃO DEFENDIDA PELO ALUNO FELIPE BOECHAT MAZZI, E ORIENTADA PELO PROF. DR FELIPPE ALEXANDRE SILVA BARBOSA.

Campinas
2023

Ficha catalográfica
Universidade Estadual de Campinas
Biblioteca do Instituto de Física Gleb Wataghin
Lucimeire de Oliveira Silva da Rocha - CRB 8/9174

M459m

Mazzi, Felipe Boechat, 1999-
Microfabrication of waveguides and ring resonators in thin-film lithium niobate / Felipe Boechat Mazzi. – Campinas, SP : [s.n.], 2023.

Orientador: Felippe Alexandre Silva Barbosa.
Dissertação (mestrado) – Universidade Estadual de Campinas, Instituto de Física Gleb Wataghin.

1. Microfabricação. 2. Niobato de lítio. 3. Fotônica integrada. 4. Fotônica quântica integrada. I. Barbosa, Felippe Alexandre Silva, 1986-. II. Universidade Estadual de Campinas. Instituto de Física Gleb Wataghin. III. Título.

Informações Complementares

Título em outro idioma: Microfabricação de guias de onda e cavidades ópticas em anel em filmes finos de niobato de lítio
Palavras-chave em inglês:
Microfabrication
Lithium niobate
Integrated photonics
Integrated quantum photonics
Área de concentração: Física Aplicada
Titulação: Mestre em Física
Banca examinadora:
Felippe Alexandre Silva Barbosa [Orientador]
Newton Cesário Frateschi
Marcelo Martinelli
Data de defesa: 03-08-2023
Programa de Pós-Graduação: Física

Identificação e informações acadêmicas do(a) aluno(a)
- ORCID do autor: https://orcid.org/0000-0001-5357-3441
- Currículo Lattes do autor: http://lattes.cnpq.br/7843376720982312

INSTITUTO DE FÍSICA
GLEB WATAGHIN

MEMBROS DA COMISSÃO EXAMINADORA DA DISSERTAÇÃO DE MESTRADO DO ALUNO FELIPE BOECHAT MAZZI – RA 230415, APRESENTADA E APROVADA AO INSTITUTO DE FÍSICA GLEB WATAGHIN, DA UNIVERSIDADE ESTADUAL DE CAMPINAS, EM 03/08/2023.

COMISSÃO JULGADORA:

- Prof. Dr. Felippe Alexandre Silva Barbosa – Presidente e Orientador (IFGW/UNICAMP)

- Prof. Dr. Prof. Dr. Newton Cesario Frateschi (IFGW/UNICAMP)

- Prof. Dr. Marcelo Martinelli (Instituto de Física, Universidade de São Paulo)

OBS.: Ata da defesa com as respectivas assinaturas dos membros encontra-se no SIGA/Sistema de Fluxo de Dissertação/Tese e na Secretaria do Programa da Unidade.

CAMPINAS

2023

Agradecimentos

O período em que desenvolvi o trabalho registrado nesta dissertação foi um dos melhores da minha vida até aqui. Sem nenhuma dúvida, isso se deve acima de tudo às pessoas incríveis com quem pude conviver e aprender dentro e fora do laboratório. Sou infinitamente grato a elas por todo o crescimento e todas as boas lembranças que tornaram esse período tão marcante e tão significativo.

Agradeço aos meus pais, Andre e Jaqueline, e ao meu irmão Arthur, pelo apoio constante, incansável e incondicional, em todos os sentidos possíveis, e ao longo de toda a minha vida.

Ao meu orientador, prof. Felippe Barbosa, pela infinita paciência, dedicação e confiança que basearam as milhares de horas de conversa e instrução que me ensinaram tanto ao longo desses anos. Mais do que isso, lhe agradeço por proporcionar um ambiente de trabalho onde me senti genuinamente feliz e motivado para aprender e produzir.

Aos professores Leandro Tessler e Pierre Louis, pela disposição de transmitir seu conhecimento e entusiasmo pela ciência. Participar do IPT sob a mentoria de vocês, e ver isso se traduzir tanto em títulos mundiais quanto em uma comunidade, foi uma das experiências mais impactantes de toda a minha formação.

Aos demais professores do LPD, prof. Newton Frateschi, Gustavo Wiederhecker e Thiago Alegre, agradeço pelos conselhos e opiniões durante as bancas, seminários e conversas no corredor, e por fazer do LPD um excelente lugar para trabalhar.

Aos amigos com quem dividi o laboratório todos os dias: Bianca, Cauê, Carol, José, Léo, Pedros (Pinho e Ariston) e Rafael, agradeço pela amizade e companhia constantes que fizeram cada dia ser interessante e imprevisível, no melhor sentido possível. Igualmente, agradeço aos amigos que fiz ao redor da Unicamp: Gio, João Luiz, Denise, Giovanna, Giovanni, Nathália, por me mostrarem, cada um à sua maneira, formas tão diferentes e tão indispensáveis de apoio e amizade.

Aos amigos que transformaram Campinas na minha segunda casa desde os primeiros meses: Gabriel, Henrique, Igor, Léo, Vini, Milena. Seria impossível fazer justiça aqui à infinidade de histórias que vivemos juntos, e o quanto assistimos o crescimento uns dos outros. Obrigado por darem sentido a tudo isso. Passar esses anos perto de vocês foi uma das maiores sortes que já tive na vida.

Aos técnicos e funcionários do CCSNano, LNNano/CNPEM e IFGW, agradeço pelo apoio indispensável para realização desta pesquisa, e pela disposição de compartilhar seu tempo e conhecimento comigo.

Por fim, agradeço a absolutamente todos que dedicaram ou dedicam seu tempo, energia e talento para construir esse lugar extraordinário que é a UNICAMP. Amo esse lugar e desejo profundamente que continue a crescer e transformar a vida de cada vez mais pessoas.

Este trabalho foi realizado com apoio do Ministério da Ciência, Tecnologia e Inovações, do Conselho Nacional de Desenvolvimento Científico e Tecnológico – CNPq (130295/2021-3) e da Fundação de Amparo à Pesquisa do Estado de São Paulo (21/12438-7).

Resumo

Circuitos fotônicos integrados (PICs) fornecem uma plataforma eficiente e escalável para processamento e transmissão de informação. Esses circuitos se baseam na manipulação de ondas eletromagnéticas, em geral através da interação com materiais dotados de propriedades específicas. O niobato de lítio é particularmente apropriado para essa tarefa. Seus coeficientes eletro-óptico e não-linear elevados viabilizam processos de mistura de frequências e modulação de alta velocidade, com aplicações essenciais em telecomunicações e sensoreamento, e fazem desse material um candidato promissor para tecnologia de informação quântica baseada em fotônica. Niobato de lítio em filme fino (TFLN) em particular permite o forte confinamento dos campos eletromagnéticos, e disponibiliza novos graus de liberdade para o design de dispositivos. Diversos avanços importantes ocorreram na última década, como a demonstrações de perdas ultra-baixas e a geração de estados não-clássicos essenciais, tais como estados de fótons únicos, estados emaranhados e estados comprimidos. Neste trabalho, desenvolvemos uma receita para microfabricação de dispositivos fotônicos em niobato de lítio apropriada para infraestrutura local de sala limpa. Inversão periódica de domínios (periodic poling) foi implementada e um sistema de acoplamento de baixa perda foi construído e testado.

Abstract

Photonic Integrated Circuits (PICs) provide an efficient and scalable platform for processing and transmitting information. Such circuits rely on the manipulation of electromagnetic waves, often achieved via interaction with materials exhibiting specific properties. Lithium Niobate (LN) is particularly well-suited for this task. Its large nonlinear and electro-optical coefficients enable frequency-mixing and high-speed modulation processes, advancing applications in communications and sensing, and making it a promising candidate for photonics-based quantum information technology. Thin-Film Lithium Niobate (TFLN) in particular allows for tight confinement of the interacting fields and unlocks additional degrees of freedom for device design. Substantial progress has been made over the past decade, demonstrating ultra-low optical losses and the generation of key nonclassical states of light such as single-photon, entangled, and squeezed states. In this work, we develop a microfabrication recipe for photonic devices in thin-film lithium niobate suitable for local cleanroom infrastructure. Periodic poling of TFLN for quasi-phase-matching is successfully implemented, and a low-loss edge coupling setup is demonstrated and tested.

List of Acronyms

4WM	Four-wave Mixing
CCSNano	Center for Semiconductor Components
CMOS	Complementary Metal-Oxide-Semiconductor
CMP	Chemical-Mechanical Polishing
CNPEM	National Center for Research in Energy and Materials
CTI	Renato Archer Information Technology Center
CVD	Chemical Vapor Deposition
DFG	Difference-Frequency Generation
DPGC	Degenerate Parametric Down-Conversion
EBL	Electron Beam Lithography
EBPVD	Electron Beam Physical Vapor Deposition
FEM	Finite Element Method
FSR	Free Spectral Range
HF	Hydrofluoric Acid
HSQ	Hydrogen Silsesquioxane
ICP-RIE	Inductively Coupled Plasma Reactive Ion Etching
IQ	Institute of Chemistry at the University of Campinas
Lamult	Multiuser Laboratory at the Gleb Wataghin Physics Institute
LFDQ/Unicamp	Physics of Quantum Devices Laboratory
LNNano	National Nanotechnology Laboratory
LPD	Device Research Laboratory
NPDA	No Pump Depletion Approximation
OPA	Optical Parametric Amplifier
OPO	Optical Parametric Oscillator

OR	Optical Rectification
PAFM	Piezoresponse Atomic Force Microscopy
PDC	Parametric Down Conversion
PECVD	Plasma Enhanced Chemical Vapor Deposition
PECVD	Plasma Enhanced Chemical Vapor Deposition
PICs	Photonic Integrated Circuits
PML	Perfectly Matched Layers
PPLN	Periodically Poled Lithium Niobate
SAW	Surface Acoustic Wave
SEM	Scanning Electron Microscope
SFG	Sum-Frequency Generation
SHG	Second Harmonic Generation
SPM	Self-Phase Modulation
SVEA	Slowly Varying Envelope Approximation
TE	Transverse Electric
TFLN	Thin-Film Lithium Niobate
TM	Transverse Magnetic
TPA	Two-Photon Absorpition
XPM	Cross-Phase Modulation

Contents

1 Introduction **12**
1.1 Outline . . . 13

2 Nonlinear Optical Interactions in Photonic Devices **14**
2.1 Interactions between light and matter . . . 14
2.1.1 Maxwell's equations in matter . . . 15
2.1.2 The nonlinear polarization . . . 17
2.2 Nonlinear photonic devices . . . 21
2.2.1 The dielectric slab waveguide . . . 21
2.2.2 The rectangular waveguide . . . 24
2.2.3 Perturbation approach for coupled-mode theory . . . 25
2.2.4 Second harmonic generation in a TFLN waveguide . . . 28
2.3 Phase matching and quasi-phase-matching . . . 29

3 Nonclassical States of Light **32**
3.1 Quantization of the electromagnetic field . . . 32
3.2 Coherent states . . . 35
3.3 Field Quadratures . . . 37
3.4 Squeezed States . . . 39

4 Optical Parametric Oscillation **42**
4.1 Optical resonators . . . 42
4.1.1 Figures of Merit . . . 47
4.2 Resonator-enhanced parametric down-conversion . . . 48

5 Experimental Methods **52**
5.1 Lithium niobate: the silicon of photonics . . . 52
5.2 Microfabrication tools and techniques . . . 56

6 Photonic Design with Finite Element Method Simulations **58**
6.1 Photonic design with the Finite Element Method . . . 58
6.2 Phase-matching conditions . . . 60

7 Microfabrication of Lithium Niobate Photonic Devices **62**
7.1 Remarks about developing a recipe from scratch . . . 62
7.2 Process overview . . . 65
7.3 Electron beam lithography . . . 66
7.3.1 Goals and limitations . . . 67
7.3.2 Substrate preparation and spin coating . . . 68

7.3.3 Dose test and proximity corrections . . . 69
7.3.4 Development . . . 71
7.3.5 Writing on positive tone resists . . . 73
7.3.6 Future improvements . . . 75
7.4 Etching of lithium niobate . . . 75
7.4.1 Goals and limitations . . . 76
7.4.2 Overview of plasma-assisted dry etching . . . 77
7.4.3 Characterization of recipes . . . 78
7.4.4 Redeposition and cleaning . . . 82
7.4.5 Etched facets . . . 83
7.5 Periodic poling of Thin-Film Lithium Niobate . . . 84

8 Coupling Light into Photonic Chips **89**
8.1 Fiber-to-chip edge coupling of light . . . 89
8.2 Facet preparation . . . 91
8.3 Measuring Q-factors . . . 93

9 Conclusions and Outlook **96**

References **97**

A Perturbative Nonlinear Rectangular Waveguide **105**

Chapter 1

Introduction

The central goal of this project is the microfabrication of integrated optical cavities in thin-film lithium niobate (TFLN), aiming at applications in quantum information technology. Optical cavities are widely used in photonic integrated circuits for signal amplification and spectral filtering. Here, we seek to prepare cavities suitable for photon-pair generation via optical-parametric oscillation, an important building block for integrated quantum photonics.

Photonic integrated circuits offer a unique platform for the implementation of quantum information technology. Their environmental stability, scalability, and compatibility with well-established fabrication techniques make them stand out among alternatives in the field [1, 2, 3]. Great progress has been achieved in the last decade towards the integration of quantum photonics experiments, including the generation of single-photon [4], entangled [5] and squeezed [6, 7, 8] states of light. Yet, the on-chip generation and manipulation of quantum states of light remains a huge scientific challenge, with major technological implications for communication, simulation, computation, metrology, and sensing. [9].

This promise has motivated several materials to be considered as platforms for quantum photonic integrated circuits [10]. Among these, Lithium niobate stands out for its excellent material properties, including a wide bandgap, large refractive index, second and third-order optical nonlinearities, Pockels electro-optic coefficient, and piezoelectricity. In the classical domain, these properties have already consolidated lithium niobate as a central material for telecommunications, especially in the form of electro-optic modulators (EOMs) and surface acoustic wave devices (SAWs) [11]. These same properties also make it a promising workhorse for quantum photonics [12], as they enable efficient nonlinear optical processes, fast modulation, and low-loss transmission.

High-quality microfabrication of photonic devices on TFLN is crucial to achieve practical applications. In this project, optical resonators in TFLN are designed, fabricated, and measured using a complete microfabrication process developed from scratch in local cleanroom facilities. Periodic poling of TFLN for quasi-phase-matching is successfully studied and implemented, and a low-loss edge coupling setup is constructed and tested. The final process yields, to the best of our knowledge, the first TFLN integrated optical cavities fabricated in Latin America and paves the way for further optimization in the near future.

1.1 Outline

The first three chapters are concerned with the theoretical foundations for the project. In Chapter 2, I will present the foundation for a theoretical description of nonlinear optical interactions in integrated photonic devices, culminating in a description of second-harmonic generation in thin-film lithium niobate. In chapter 3, I will describe key concepts of quantum optics necessary to describe nonclassical states of light, form the quantization of the electromagnetic field to the definition of squeezed states. Finally, in Chapter 4, I will provide a theoretical description of Fabry-Perot optical cavities, which work as a model for the optical properties of ring resonators fabricated in this project. This will be combined with considerations in nonlinear optics to reach a theoretical description of the optical parametric oscillator, a central element of quantum photonic integrated circuits.

In Chapter 5, I will discuss the main experimental choices of the project. I will present a review of the properties, applications and important results in lithium niobate photonics, aiming to justify its use in the project. Next, the tools of microfabrication used in the project will be listed and briefly discussed. Finally, balanced homodyne detection will be presented and described as a tool to measure nonclassical light.

In Chapter 6, I will show key computational results that help set the necessary benchmarks for fabrication. Chapter 7 contains the heart of the experimental work in this project, where the development process for the microfabrication recipe is described in detail. Finally, Chapter 8 discusses the challenges and strategies for fiber-to-chip coupling of light, and presents the optical measurement of the fabricated devices.

Chapter 2

Nonlinear Optical Interactions in Photonic Devices

In this chapter, we will introduce the basic formalism to model and optimize nonlinear optic interactions in integrated photonic devices. The first section describes the basic principles of nonlinear optics, and how they arise from specific material properties. The second section will introduce the physics of integrated photonic devices such as dielectric waveguides, and combine it with the preceding results to model on-chip nonlinear interactions. Finally, the last section will discuss how quasi-phase-matching can be used to overcome material limitations and achieve efficient nonlinear conversion.

2.1 Interactions between light and matter

Nonlinear optics always deals with interactions between light and matter. When light encounters material media, the fields that make up the electromagnetic wave accelerate charges bound to atoms in the material. This gives rise to induced electric dipole moments. At sufficiently high intensities, this polarization will respond nonlinearly to the incident field. This mechanism lies at the heart of nonlinear optics and is the central concern of this section.

2.1.1 Maxwell's equations in matter

It is possible to clarify the influence of a material medium in the propagation of light by making modifications in Maxwell's Equations in vacuum [13]

$$\nabla \cdot \mathbf{E} = \frac{\rho}{\epsilon_0}, \quad \nabla \times \mathbf{E} = -\frac{\partial \mathbf{B}}{\partial t}, \quad \nabla \cdot \mathbf{B} = 0, \quad \nabla \times \mathbf{B} = \mu_0 \mathbf{J} + \mu_0 \epsilon_0 \frac{\partial \mathbf{E}}{\partial t}. \tag{2.1}$$

In this form, by setting the charge (ρ) and current (J) densities to zero, Maxwell's Equations can be manipulated to obtain wave equations for both the electric and magnetic fields,

$$\nabla^2 \mathbf{E} - \mu_0 \epsilon_0 \frac{\partial \mathbf{E}}{\partial t^2} = 0, \quad \nabla^2 \mathbf{B} - \mu_0 \epsilon_0 \frac{\partial \mathbf{B}}{\partial t^2} = 0, \tag{2.2}$$

which predict electromagnetic waves propagating with the speed of light, given by $c = (\mu_0 \epsilon_0)^{-1/2}$.

In a material medium, additional sources of electric field will appear in the form of charge densities. These contributions can be considered separately by rewriting the charge density as

$$\rho = \rho_f + \rho_b = \rho_f - \nabla \cdot \mathbf{P}, \tag{2.3}$$

where the first term corresponds to free charges that may exist in the material in the form of moving electrons or ions. The second term corresponds to the "bound" charges arising due to the push and pull on electron clouds, inducing a dipole moment density along the path of light. Such polarization density $\mathbf{P}$ is the source for bound-charge density (ρ_b) and lies at the heart of nonlinear optics. [1]. In the linear regime, it is related to the electric field by the electric susceptibility χ_e of the material, which is set as zero for the vacuum, such that

$$\frac{1}{\epsilon_0}\mathbf{P} = \tilde{\chi}^{(1)}\mathbf{E} + \tilde{\chi}^{(2)}\mathbf{E}^2 + \tilde{\chi}^{(3)}\mathbf{E}^3 + \ldots \tag{2.4}$$

Once this separation of sources is established, it becomes natural to use Equation 2.3 to rewrite Gauss's Law by defining $\mathbf{D} = \nabla \cdot (\epsilon_0 \mathbf{E} + \mathbf{P})$, such that

$$\nabla \cdot \mathbf{D} = \rho_f, \tag{2.5}$$

[1] The dipole moment points away from negative charges, therefore a diverging $\mathbf{P}$ indicates an accumulation of negative charges, which is why $\nabla \cdot \mathbf{P}$ appear with a negative sign on Equation 2.3.

where **D** is the electric displacement field, whose divergence is null in the absence of free charges in a material.

To complete the rewriting of Maxwell's Equations, a similar transformation can be done for the magnetic field. Here, we separate the current contributions as

$$\mathbf{J} = \mathbf{J}_f + \mathbf{J}_b + \mathbf{J}_p = \mathbf{J}_f + \nabla \times \mathbf{M} + \frac{\partial \mathbf{P}}{\partial t}. \tag{2.6}$$

The first term accounts for the free currents that may be present in the material. The second term arises due to the induction of magnetic dipoles in matter, resulting in a magnetic dipole density **M**. The circulation of this density gives rise to the bound currents. The last term relates to the changes in the bound electric charges modeled by the polarization **P**.

Once again, this separation of sources in Equation 2.6 motivates the definition of a "new" field, and a magnetic susceptibility χ_m,

$$\mathbf{H} \overset{\text{def}}{=} \left(\frac{1}{\mu_0}\mathbf{B} - \mathbf{M} \right) = \frac{1}{\mu_0(1+\chi_m)}\mathbf{B} = \frac{1}{\mu}\mathbf{B}, \tag{2.7}$$

such that Ampère's Law can be rewritten as

$$\nabla \times \left(\frac{1}{\mu_0}\mathbf{B} - \mathbf{M} \right) = \mathbf{J}_f + \frac{\partial}{\partial t}\left(\mathbf{P} + \epsilon_0 \mathbf{E}\right) \quad \Rightarrow \quad \nabla \times \mathbf{H} = \mathbf{J}_f + \frac{\partial \mathbf{D}}{\partial t}. \tag{2.8}$$

Leading to the following final form to write Maxwell's Equations in matter

$$\nabla \cdot \mathbf{D} = \rho_f, \quad \nabla \times \mathbf{E} = -\frac{\partial \mathbf{B}}{\partial t}, \quad \nabla \cdot \mathbf{B} = 0, \quad \nabla \times \mathbf{H} = \mathbf{J}_f + \frac{\partial \mathbf{D}}{\partial t}. \tag{2.9}$$

From which we can also write wave equations for both electric and magnetic fields. By using the definitions of Equations 2.5 and 2.7, it is clear that they can be made identical to the previous wave equations, except for the change from μ_0 and ϵ_0 to μ and ϵ (respectively, the magnetic permeability and the electrical permittivity of a given medium), such that the phase velocity of the electromagnetic wave changes to

$$v = \frac{1}{\sqrt{\mu\epsilon}}, \tag{2.10}$$

and the ratio to the phase velocity in a vacuum defines the refractive index

$$n = \frac{c}{v} = \sqrt{(1+\chi_m)(1+\chi_e)}.. \tag{2.11}$$

Notice that this simple, dimensionless quantity arises naturally from the modifications introduced to Maxwell's Equation. In this linear, dispersionless regime, the refractive index completely describes the changes imposed on the propagation of light by the presence of a material medium. Just from direct comparison to the vacuum wave equations, we see that the phase velocity is changed from c to c/n and the wavelength is changed from λ to λ/n. Other phenomena related to interactions with material media, such as refraction and reflection, can also readily be studied with reference to n by closer inspection of the equations given above. Furthermore, the dependence of the material's properties χ_e and χ_m on the frequency of the optical signal will lead to material dispersion.

However, in order to account for nonlinear optical phenomena, we must consider a more complete picture of the interactions of light and material media. At sufficiently high intensities, higher-order terms of the electric field must be considered to compute the polarization, giving rise to frequency-mixing. At this point, it is helpful to consider in greater detail the physical mechanism behind the interaction of electromagnetic fields with the bound charges it encounters in materials.

2.1.2 The nonlinear polarization

Lorenz's oscillator model for the atom [14] is an intuitive and powerful description of the optical response of bound charges in a material medium. Here, we will briefly use it as a smooth introduction to the nonlinear optical responses of materials, and to the tensorial nature of the nonlinear optical susceptibility.

In Lorenz's model, electrons are treated as if they were bound to the atomic nucleus by "springs" with specific strengths. Thus, the system consists of a damped-driven harmonic oscillator, governed by an equation like

$$\ddot{x}(t) + 2\gamma\dot{x}(t) + \omega_0^2 x + ax^2 = -\frac{eE(t)}{m},. \tag{2.12}$$

Notice that we introduced a nonlinearity simply by adding a quadratic term to the restoring force. As a consequence, if an optical field of the form

$$E(t) = e^{-i\omega_1 t} + e^{-i\omega_2 t} + \text{c.c.} \tag{2.13}$$

is applied, then solving equation 2.12 by perturbation methods will yield one linear solution of the form

$$x^{(1)}(t) = x_1^{(1)} e^{-i\omega_1 t} + x_2^{(1)} e^{-i\omega_2 t} + \text{c.c.}, \tag{2.14}$$

and a series of second-order solutions whose frequencies can be computed by squaring the input field. Assuming unit amplitude for all components, this leads to

$$\begin{aligned} x^{(2)}(t) = [E(t)]^2 &= (e^{i\omega_1 t} + e^{i\omega_2 t} + e^{i\omega_2 t} + e^{-i\omega_2 t})(e^{i\omega_1 t} + e^{-i\omega_1 t} + e^{i\omega_2 t} + e^{-i\omega_2 t}) \\ &= 4 + e^{2i\omega_1 t} + e^{2i\omega_2 t} + 2e^{i(\omega_1+\omega_2)t} + 2e^{i(\omega_1-\omega_2)t} + c.c.. \end{aligned} \tag{2.15}$$

The linear response of the harmonic oscillator corresponds to the polarization $\mathbf{P}$ shown in Equation 2.3. The oscillator is driven by the incident electric field, and "damped" by specific material properties. The higher-order responses to the driving force, which will become significant once oscillations amplitudes are large enough, correspond to the nonlinear polarization $\mathbf{P}_{NL}$.

Physically, this nonlinear optical response does in fact give rise to a myriad of phenomena. Each of the terms in Equation 2.15 models an actual second-order nonlinear process, mixing the frequencies in the original signal in several of ways. The constant corresponds to the Optical Rectification (OR) of both fields, the following two terms correspond to Second Harmonic Generation (SHG), and the last two terms correspond to Sum-Frequency Generation (SFG) and Difference-Frequency Generation (DFG). A similar solution can be carried out to obtain third-order processes, which will mix the input frequencies in different ways.[2] Thus, materials exhibiting nonlinear optical responses are capable of mixing the frequencies of the optical fields that traverse through them.

Translating this back into Maxwell's Equations, we are motivated to model nonlinear optical phenomena by expanding the "complete" polarization $\mathbf{P}$ as a power series in terms of the

[2] In this case, the restoring force was modeled by a quadratic term, corresponding to a noncentrosymmetric potential ($U(x) \neq U(-x)$). To represent a centrosymmetric potential, a cubic restoring force must be used, and the first non-vanishing nonlinear terms will be third-order. This simple consideration accounts for the physical fact that only noncentrosymmetric materials exhibit second-order nonlinear optical susceptibilities.

electric field. In simplified notation, this gives rise to

$$\frac{1}{\epsilon_0}\mathbf{P} = \tilde{\chi}^{(1)}\mathbf{E} + \tilde{\chi}^{(2)}\mathbf{E}^2 + \tilde{\chi}^{(3)}\mathbf{E}^3 + \dots, \tag{2.16}$$

where we have dropped the subscript in χ_e since it is no longer necessary to distinguish between the optical and magnetic susceptibilities[3].

In Equation 2.16, the expansion coefficients are n-th order susceptibilities corresponding to $(n+1)$-th-rank tensors. The tensor nature of the coefficients reflects the polarization dependencies and symmetries of the susceptibilities and is, therefore, a consequence of material properties. In the following subsection, we will show how these tensors act to mix different polarization components of the interacting fields.

In more precise notation, we may write each frequency component of the nonlinear polarization vector, considering terms up to third order, in the following way [15]:

$$\frac{1}{\epsilon_0}P_{NL,i}(\omega) = \sum_{\alpha,\beta}\sum_{j,k}\tilde{\chi}^{(2)}_{ijk}(\omega,\omega_\alpha,\omega_\beta)E_j(\omega_\alpha)E_k(\omega_\beta) + \sum_{\alpha,\beta,\gamma}\sum_{j,k,l}\tilde{\chi}^{(3)}_{ijkl}(\omega,\omega_\alpha,\omega_\beta,\omega_\gamma)E_j(\omega_\alpha)E_k(\omega_\beta)E_l(\omega_\gamma). \tag{2.17}$$

where the indices i, j, k, l will span the three spatial coordinates, and m, n will span all frequencies such that $\omega = \omega_\alpha + \omega_\beta$ (including ω_γ) in the third-order case.

For optical frequencies much smaller than the material's resonance, Kleinman's symmetry can be utilized to neglect the dispersion of the susceptibilities [15], meaning the ω_i dependencies can be dropped, greatly simplifying Equation 2.17. Further simplification arises from symmetry considerations for the susceptibility tensor $\tilde{\chi}^{(2)}$.

Let us consider an example of practical importance for this work, that of SHG in Lithium Niobate. Assuming an input optical field of frequency ω given by

$$\vec{E}(t) = E_1(t)\hat{x} + E_2(t)\hat{y} + E_3(t)\hat{z}, \tag{2.18}$$

We shall use the second-order term in Equation 2.17 evaluated at frequency 2ω. For simplicity, we omit the time and frequency dependence of the field components. The summation over frequency components is eliminated, as there is only one non-zero contribution at ω, we then

[3]This is not an arbitrary choice, rather it is due to the typically low values of magnetic susceptibility, as compared to its electric counterparts.

sum over all nine combinations of spatial components,

$$\begin{aligned}\frac{1}{\epsilon_0}P_{NL,i}(2\omega) &= \sum_{j,k}\tilde{\chi}^{(2)}_{ijk}E_j(\omega)E_k(\omega)\\ &= \chi^{(2)}_{i11}E_1E_1 + \chi^{(2)}_{i12}E_1E_2 + \chi^{(2)}_{i13}E_1E_3 + \chi^{(2)}_{i21}E_2E_1 + \chi^{(2)}_{i22}E_2E_2 +\\ &+ \chi^{(2)}_{i32}E_2E_3 + \chi^{(2)}_{i31}E_3E_1 + \chi^{(2)}_{i32}E_3E_2 + \chi^{(2)}_{i33}E_3E_3.\end{aligned} \tag{2.19}$$

Major simplifications arise from symmetry considerations for the susceptibility tensor $\tilde{\chi}^{(2)/}$. This leads to a contracted notation where the rank-3 tensor $\tilde{\chi}^{(2)}$ can be reduced to a two-dimensional matrix with elements d_{ij}. In the case of Lithium Niobate, we are left with only three non-vanishing [16], distinct elements, such that

$$\begin{pmatrix}P^{(NL)}_x(2\omega)\\ P^{(NL)}_y(2\omega)\\ P^{(NL)}_z(2\omega)\end{pmatrix} = \begin{pmatrix}0 & 0 & 0 & 0 & d_{31} & -d_{22}\\ -d_{22} & d_{22} & 0 & d_{31} & 0 & 0\\ d_{31} & d_{31} & d_{33} & 0 & 0 & 0\end{pmatrix}\begin{pmatrix}E_1^2\\ E_2^2\\ E_3^2\\ 2E_2E_3\\ 2E_3E_1\\ 2E_1E_2\end{pmatrix} dxdy \tag{2.20}$$

This is a general expression for the nonlinear polarization term related to second-harmonic generation in Lithium Niobate. Thus, we arrive at the main takeaway of this section. Equation 2.20 demonstrates how the nonlinear susceptibility mixes frequency components in a polarization-sensitive manner, as determined by material properties.

Once the nonlinear polarization has been computed, it can be plugged into Maxwell's Equations to compute the amplitudes and propagation of the generated waves. We simply follow the standard procedure to obtain a wave equation from Equation (2.9), thus

$$\nabla^2\mathbf{E} - \mu_0\frac{\partial^2}{\partial t^2}\mathbf{D} = 0. \tag{2.21}$$

Where we have assumed that the term $\nabla(\nabla\cdot\mathbf{E})$ has a negligible contribution [15]. But now we write $\mathbf{D} = \epsilon_0\mathbf{E} + \mathbf{P}^{(\mathrm{L})} + \mathbf{P}^{(\mathrm{NL})} = \epsilon\mathbf{E} + \mathbf{P}^{(\mathrm{NL})}$, which translates to

$$\nabla^2\mathbf{E} - \mu_0\epsilon\frac{\partial^2}{\partial t^2}\mathbf{E} = \mu_0\frac{\partial^2}{\partial t^2}\mathbf{P}^{(\mathrm{NL})} \tag{2.22}$$

which is simply a driven wave equation, where the nonlinear polarization acts as a source term on the right-hand side. Using the expression for $\mathbf{P}^{(\mathrm{NL})}$ given in Equation 2.20, this equation can be solved in a straight-forward way to obtain a description for so-called free-space nonlinear optical interactions.

While much insight can be gained from this solution, here we are interested in considering nonlinear interactions in integrated photonic devices. Thus, we must first solve Maxwell's Equations for boundary conditions typical of these systems. Once this is done, we can follow a very similar procedure to account for nonlinearities.

2.2 Nonlinear photonic devices

The development of nonlinear optics [17] is closely related to the invention of the laser [18]. Indeed, nonlinear optical phenomena only become significant at high optical intensities, such as those provided by lasers. Integrated photonic devices offer an additional way to enhance optical intensity in nonlinear media: by confining light in wavelength-sized dielectric devices.

These devices provide miniaturizable, scalable and versatile platforms to fulfill several tasks of information technology with high efficiency, environmental stability and low power consumption. These advantages have made such devices ubiquitous in data and telecommunications [19, 20], sensing [21], and increasingly present in quantum information science [1].

Modelling nonlinear optical interactions in integrated devices is a necessary step prior to design and fabrication. The simplest dielectric integrated device is the idealized slab waveguide as shown in Figure 2.1(a). Most of the key features of "real" waveguides can be understood and often approximated by these systems. Thus, we begin this section with a short overview of its solutions and key physical properties.

2.2.1 The dielectric slab waveguide

A dielectric slab waveguide consists of a stacking of three materials: substrate, core and cover, such that the core has the highest refractive index of all three. A theory of these waveguides begins by taking Equation 2.21 for the electric field in a material medium,

$$\nabla^2\mathbf{E} - \mu\epsilon\frac{\partial^2\mathbf{E}}{\partial t^2} = 0, \tag{2.23}$$

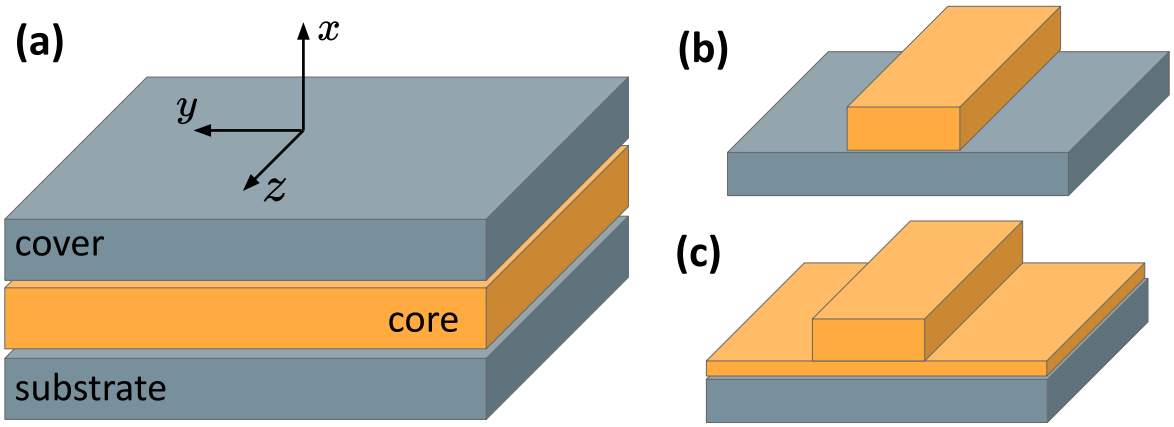

Figure 2.1: (a) A diagram representing the dielectric slab waveguide, constituted of substrate, core, and cover layers. (b) A rectangular ridge waveguide, represented with no cover layer. (c) A rectangular rib waveguide, where shallow etching of the core layer leads to the formation of a thin slab-like layer.

note that setting $\nabla \cdot \mathbf{E} = 0$, as needed to obtain this wave equation, is ensured in the linear optics regime for an isotropic, source-free medium. Considering the system described in Figure 2.1(a), we propose an ansatz based on symmetry considerations,

$$E_y(x, z, t) = E_y(x)e^{i(\omega t - \beta z)}. \tag{2.24}$$

Alternatively, the same can be done for the **H**-field. By proposing a solution of this form, we are assuming that the electric field is always polarized along the infinite y direction as the wave propagates. This corresponds to a Transverse Electric (TE) mode, where electric field component is always zero in the propagation direction. If we do the same for the magnetic field, the result would be a Transverse Magnetic (TM) mode.

Noting the definition for the refractive index in Equation 2.11, and substituting the ansatz in Equation 2.24 back in the wave equation, this yields

$$\frac{\partial^2 E_y}{\partial x^2} + \left(k_0^2 n_i^2 - \beta^2\right) E_y = 0. \tag{2.25}$$

A physically meaningful guided mode should have an oscillatory solution inside the core, and exponentially decaying solutions in the substrate and cover. In this case, we define

$$\begin{cases} \gamma_i = \sqrt{\beta^2 - k_0^2 n_i^2}, & \Rightarrow \quad E_y(x) = E_0 e^{-\gamma_i x}, \text{ in the cover and substrate} \\ \kappa = \sqrt{k_0^2 n_{\text{core}}^2 - \beta^2}, & \Rightarrow \quad E_y(x) = E_0 e^{\pm i\kappa x}, \text{ in the core.} \end{cases} \tag{2.26}$$

By demanding that the tangential components of **E** and **H** be continuous at the interfaces, we arrive at two transcendental equations, corresponding to families of TE and TM modes. If h is the core height for the slab waveguide core, then [22]

$$\tan(h\kappa) = \frac{\gamma_c + \gamma_s}{\kappa\left[1 - \frac{\gamma_c\gamma_s}{\kappa^2}\right]}, \quad \text{(TE modes)} \qquad \tan(h\kappa) = \frac{\kappa\left[\frac{n^2}{n_s^2}\gamma_s + \frac{n^2}{n_c^2}\gamma_c\right]}{\kappa^2 - \frac{n^2}{n_c^2 n_s^2}\gamma_c\gamma_s} \quad \text{(TM modes).} \tag{2.27}$$

All variables in these equations can be parameterized in terms of κ, which in turn can be plugged into Equations 2.26 to compute the spatial distribution and propagation constant (β) of each mode. It is common to refer to each mode by its effective refractive index n_{eff},

$$n_{\text{eff}} = \frac{\beta}{k_0}, \quad k_0 = \frac{2\pi}{\lambda}, \tag{2.28}$$

which fully characterizes a given slab waveguide mode, apart from boundary conditions and material properties. Equation 2.28 defines the effective refractive index as the fractional component of the wavevector in the propagation direction. Note that this implies that modes with lower effective refractive index have larger transverse components. It is therefore natural that higher-order modes have lower effective refractive indices. Throughout this work, the effective index will be used as a central parameter to characterize optical modes in integrated devices.

The distinction between TE and TM is of essential for photonic design. In Section 2.1.2 we showed that the nonlinear susceptibility mixes frequencies in a polarization-sensitive manner, therefore we can expect TE and TM modes to differ in their efficiency for nonlinear processes on that basis alone. Furthermore, these modes will also experience waveguide dispersion effects in distinct ways, meaning that phase-matching conditions will differ for each of them when considering a nonlinear process.

One key distinction that facilitates the identification of such modes, is the presence of discontinuities. To obtain Equation 2.27, we assumed that the tangential components of the **E**

and **H** fields were continuous along the material interfaces. However, in the absence of free charges, the normal components of the **D** field obey

$$(\mathbf{D}_1 - \mathbf{D}_2) \cdot \hat{n}_{1,2} = \epsilon_1 E_{1,\perp} + \epsilon_2 E_{2,\perp} = 0, \tag{2.29}$$

which implies in a discontinuity when the permittivity $\epsilon_i = \epsilon_0(1+\chi_e)$ changes between media. In general, there is no equivalent discontinuity for the magnetic field, since the magnetic permeability χ_m does not change between most dielectric medic used in photonics applications.

For rectangular waveguides, the solution can not be computed analytically, and the distinction between TE and TM modes is not as straightforward. One such system is the rectangular dielectric waveguide, of major practical interest for integrated photonics.

2.2.2 The rectangular waveguide

Section 2.2.1 has introduced most of the basic vocabulary and notation for the treatment of optical waveguides. However, experiments will always deal with waveguides with a finite transverse profile, which the slab waveguide can only approximate.

Consider a rectangular waveguide, as represented in Figure 2.1(b) and (c). In this case, we are dealing with a system exhibiting only translational symmetry in the z direction for the amplitude, thus we propose a solution of the form

$$\mathbf{E}(x, y, z) = \mathbf{E}(x, y)e^{i(\omega t - \beta z)}, \tag{2.30}$$

in which no specific polarization direction has been assumed, contrary to the slab waveguide ansatz (Equation 2.24). Plugging into the wave equation, as shown in Section 2.2.1, we arrive at

$$\left(\frac{\partial^2}{\partial x^2} + \frac{\partial^2}{\partial y^2}\right)\mathbf{E}(x, y) + \left(n_i^2 k_0^2 - \beta^2\right)\mathbf{E}(x, y) = 0. \tag{2.31}$$

While there are approximation methods to solve Equation 2.31 [23] in certain parameter regions, we rely on the Finite Element Method do obtain a solution, as implemented in COMSOL Multiphysics ®, as detailed in Chapter 6.

The solution follows a procedure similar to the slab waveguide. We may think of Equation 2.31 as an eigenvalue problem, where the eigenvalues are the propagation constants, and the field profiles are the eigenvectors. As such, it is useful to write each solution of the rectangular

waveguide as

$$\mathbf{E}(x,y,z,t) = \sqrt{P_m}A(z,\omega)\mathbf{F}_m(x,y)\exp\left(-i\left[\beta_m z - \omega t\right]\right). \tag{2.32}$$

In this notation, the field distribution along the transverse plane is normalized by the total field power, and denoted by $\mathbf{F}(x,y)$. The $A(z,\omega)$ amplitude has crucial physical significance. This factor will model changes in the amplitudes of specific modes during propagation. These changes may arise as a consequence of perturbation to the original set of waveguide modes, either due to optical nonlinearities, defects in the waveguide geometry, or the presence of adjacent waveguides.

2.2.3 Perturbation approach for coupled-mode theory

We now come to the most important result of this chapter, a simple and general theory of perturbations to the polarization in waveguides. We begin by restating the Wave Equation 2.2 for the electric field,

$$\nabla^2\mathbf{E} - \mu\epsilon\frac{\partial^2\mathbf{E}}{\partial t^2} = 0, \tag{2.33}$$

and introducing a notation to address power-normalized mode profiles $\mathbf{F}(x,y)$ and $\mathbf{G}(x,y)$. These are defined as

$$\mathbf{F}_m(x,y) = \frac{1}{\sqrt{P_m}}\mathbf{E}_m(x,y) \quad \text{and} \quad \mathbf{G}_m(x,y) = \frac{1}{\sqrt{P_m}}\mathbf{H}_m(x,y). \tag{2.34}$$

In this framework, considering only linear polarization, the total fields in a waveguide could be written as

$$\mathbf{E}(\mathbf{r},\omega) = \sum_m A_m\mathbf{F}_m(x,y)e^{-i(\beta_m z-\omega t)} \quad \text{and} \quad \mathbf{H}(\mathbf{r},\omega) = \sum_m A_m\mathbf{G}_m(x,y)e^{-i(\beta_m z-\omega t)},, \tag{2.35}$$

where the amplitudes $A_m = \tilde{A}_m\sqrt{P_m}$ have units of square-root power, and $\tilde{A}_m$ are their dimensionless counterparts. Here, if we plug the expansions back into the wave equation, the result yields the familiar

$$\left[\left(\frac{\partial^2}{\partial x^2} + \frac{\partial^2}{\partial y^2}\right) + \left(n_i^2 k_{0,m}^2 - \beta_m^2\right)\right] A_m\mathbf{F}_m(x,y)e^{-i(\beta_m z-\omega t)} = 0, \tag{2.36}$$

which tells the full story of the unperturbed system. To introduce the perturbation, we recover the wave Equation 2.22, which was obtained by considering

$$\mathbf{D} = \epsilon\mathbf{E} + \mathbf{P}^{(\mathrm{NL})}, \tag{2.37}$$

except this time we take a more general case of a perturbation to the original polarization. Accordingly, we replace $\mathbf{P}^{(\mathrm{NL})}$ by $\mathbf{P}_{\mathrm{pert}}$ and, as in the previous case, arrive at

$$\nabla^2\mathbf{E} - \mu_0\epsilon\frac{\partial^2}{\partial t^2}\mathbf{E} = \mu_0\frac{\partial^2}{\partial t^2}\mathbf{P}_{\mathrm{pert}}. \tag{2.38}$$

Now, we will introduce a z-dependency on the amplitudes $A_m(z)$ in 2.35 to model the effects of perturbations. As stated earlier, these could be defects in the waveguide geometry, local changes in refractive index, the presence of adjacent waveguides or, more importantly, the nonlinear optical response of a material. By adding the z-dependency, it is anticipated that such perturbations will allow optical power to flow between different modes m.

With this subtle change, the second-order derivative with respect to z will yield many "new" terms. Thus, the result of plugging the fields in Equation 2.38 is now

$$\sum_m \left[\frac{\partial^2}{\partial z^2}A_m(z) - 2i\beta\frac{\partial}{\partial z}A_m(z)\right]\mathbf{F}_m(x,y)e^{-i(\beta_m z-\omega t)} + \sum_m \left[\left(\frac{\partial^2}{\partial x^2}+\frac{\partial^2}{\partial y^2}\right) + \left(n_i^2k_0^2 - \beta_m^2\right)\right]A_m(z)\mathbf{F}_m(x,y)e^{-i(\beta_m z-\omega t)} = \mu_0\frac{\partial^2}{\partial t^2}\mathbf{P}_{\mathrm{pert}},$$

clearly, the left-hand side term in the bottom row will vanish, as it satisfies the unperturbed wave equation, therefore

$$\sum_m \left[\frac{\partial^2}{\partial z^2}A_m(z) - 2i\beta_m\frac{\partial}{\partial z}A_m(z)\right]\mathbf{F}_m(x,y)e^{-i(\beta_m z-\omega t)} = \mu_0\frac{\partial^2}{\partial t^2}\mathbf{P}_{\mathrm{pert}}. \tag{2.39}$$

Note that, physically, all the dependency of the amplitude $A_m(z)$ with respect to the propagation direction z is a consequence of the perturbation $\mathbf{P}_{\mathrm{pert}}$. As in most perturbation theories, the validity of this assumption hinges on the perturbation being "weak" enough. Thus, we assume that the amplitudes of the modes vary slowly along the propagation, such that the second-order derivative with respect to z can be neglected. This is often referred to as the

Slowly Varying Envelope Approximation (SVEA). By doing so, we arrive at

$$\sum_m 2i\beta_m \left[\frac{\partial}{\partial z}A_m(z)\right]\mathbf{F}_m(x,y)e^{-i(\beta_m z-\omega t)} = -\mu_0\frac{\partial^2}{\partial t^2}\mathbf{P}_{\text{pert}}. \tag{2.40}$$

Next, we employ a common "trick" to exploit the orthogonality of the modes in the **slab** waveguide [24]. Namely, we take the dot product of both sides of the equation with respect to a different mode profile $\mathbf{F}_n^*(x,y)$, and integrate in the plane perpendicular to the propagation direction

$$\sum_m 2i\beta_m \left[\frac{\partial}{\partial z}A_m(z)\right]e^{-i(\beta_m z-\omega t)}\iint_{-\infty}^{\infty}\mathbf{F}_m(x,y)\cdot\mathbf{F}_n^*(x,y)\,dxdy = -\mu_0\frac{\partial^2}{\partial t^2}\iint_{\infty}^{\infty}\mathbf{P}_{\text{pert}}\cdot\mathbf{F}_n^*(x,y)\,dxdy. \tag{2.41}$$

So far, this demonstration has been general to both idealized slab waveguides and "real", rectangular waveguides. To simplify the orthonormality relation, however, we will now carry out the integral on the left-hand side assuming that the system behaves as a slab waveguide, with well-defined pure TE(TM) modes, such that $\mathbf{F}_m = F_{m,j}\,\hat{\mathbf{j}}$ and $\mathbf{G}_m = G_{m,i}\,\hat{\mathbf{i}}$. Then, **G**(x,y) can be written in terms of **F**(x,y) using Faraday's law, such that

$$\frac{1}{2}\iint_{-\infty}^{\infty}\mathbf{F}_m^*\times\mathbf{G}_n\,dxdy = \delta_{mn} \quad\Rightarrow\quad \iint_{-\infty}^{\infty}\mathbf{F}_m(x,y)\cdot\mathbf{F}_n^*(x,y)\,dxdy = \frac{2\omega\mu_0}{\beta_m}\delta_{mn}. \tag{2.42}$$

In the rectangular waveguide, the same orthonormality relation (in terms of a cross-product) applies, but it cannot be rewritten in terms of a single dot-product, as shown here. However, a different procedure can be used to arrive at the exact same result obtained in this section without recourse to the slab waveguide [25], by using a different set of approximations. For completion, this approach is also carried out in detail in Appendix A.

Now, plugging Equation 2.42 into Equation 2.41 and carrying out the summation, we arrive at

$$\frac{\partial}{\partial z}A_m(z) = \frac{i}{4\omega}e^{i(\beta_m z-\omega t)}\frac{\partial^2}{\partial t^2}\iint_{\infty}^{\infty}\mathbf{P}_{\text{pert}}\cdot\mathbf{F}_m^*(x,y)\,dxdy. \tag{2.43}$$

This is the central equation for the theory of coupled modes. It is able to predict how the amplitude of a given mode m will change along the propagation direction z given the presence of a specific perturbation $\mathbf{P}_{\text{pert}}$ to the linear polarization of the material where the light is propagating. Notice that the strength of the coupling between modes is fundamentally propor-

tional to the spatial overlap between the perturbation source and the mode being considered, as calculated by the surface integral on the right-hand side.

Specific properties of coupled mode theory will appear for the case of nonlinear optical effects once the perturbation $\mathbf{P}_{\text{pert}}$ is replaced by the nonlinear polarization $\mathbf{P}^{(\text{NL})}$ shown in Equation 2.20. These properties will be central for considerations on device design, and on the desirable material properties for optimal nonlinear performance.

2.2.4 Second harmonic generation in a TFLN waveguide

In this subsection, we will apply the general Equation 2.43 to the case of second harmonic generation in a thin-film lithium niobate waveguide. This is a case of great practical interest given our context. First, because the phase matching conditions for SHG are the same as for Degenerate Parametric Down-Conversion (DPGC), which is a standard process for photon-pair generation, and a major motivation for this project. Second, SHG is a thresholdless process, relatively easy to measure optically, requiring a single pump source and with reasonably low phase mismatch for lithium niobate for the NIR-telecom transition, which makes it an ideal candidate for testing our first fabricated devices.

In section 2.1.2, the nonlinear polarization up to second order was computed for the second-harmonic frequency 2ω, given an input at ω. The final expression in Equation 2.20 contains three separate components of the second-order nonlinear susceptibility tensor, d_{22}=2.4 pm/V, d_{31}=−4.52 pm/V and d_{33}=31.5 pm/V [26]. Since the d_{33} component is significantly larger than its counterparts, we consider only its contribution, thus looking solely at the crystalline z-component[4] of the nonlinear polarization,

$$\begin{aligned}\frac{1}{\epsilon_0}P_{NL,z}(2\omega) &= -d_{22}\left(E_1^2 - E_2^2 + 2E_1E_2\right) + d_{31}\left(E_1^2 + E_2^2 + 2E_2E_3 + 2E_1E_3\right) + d_{33}\left(E_3^2\right) \\ &\approx d_{33}E_3^2.\end{aligned}$$

Therefore, adjusting for the notation developed in the previous section, the perturbation to be substituted into Equation 2.43 is

$$\mathbf{P}_{\text{pert}} = \mathbf{P}^{(\text{NL})} = \epsilon_0 d_{33}\left[A_\omega(z)\right]^2\left[F_\omega(x,y)\right]^2 e^{-2i(\beta_\omega z-\omega t)}\,\hat{\mathbf{z}}_0, \tag{2.44}$$

[4]Not to be confused with the propagation component, also referred to as z. Henceforth, only the components of the field parallel to the d_{33} axis are considered.

such that, once the time derivatives are computed,

$$\frac{\partial}{\partial z}A_{2\omega}(z) = -\frac{i\omega}{2}\left[A_{\omega}^{2}(z)\right]e^{i[\beta_{2\omega}-2\beta_{\omega}]z}\epsilon_0 d_{33}\iint_{\infty}^{\infty}\left[F_{\omega}(x,y)\right]^{2}\left[F_{2\omega}^{*}(x,y)\right]\,dxdy. \tag{2.45}$$

The equation can be integrated from $z = 0$ to $z = L$ assuming that the initial power at the second-harmonic frequency is zero, and employing the No Pump Depletion Approximation (NPDA), where pump power is $A(z) = |A_{\omega}(0)|^2 = P_0$. As a result, the SHG conversion efficiency η is given by

$$\eta = \frac{|A_{2\omega}|^2}{|A_{\omega}(0)|^2} = \left|\frac{i\omega}{2}\epsilon_0 d_{33}\iint_{\infty}^{\infty}\left[F_{\omega}(x,y)\right]^{2}\left[F_{2\omega}^{*}(x,y)\right]\right|^{2} P_0 L^2 \mathrm{sinc}^2\left[\left(\beta_{2\omega}-2\beta_{\omega}\right)L\right]. \tag{2.46}$$

This expression summarizes the relevant physics for SHG. The surface integral requires the original and generated mode to have good spatial overlap, that is, to have similar mode profiles on the transverse plane. Given that $F(x, y)$ represents the normalized fields, this integral is also largest when the optical modes are confined in a small area, thus representing high optical intensity, typical of integrated devices.

Finally, efficiency is highly sensitive to the phase mismatch of the interacting modes

$$\Delta\beta = \beta(2\omega) - 2\beta(\omega), \tag{2.47}$$

in other words, the waves must maintain a specific phase relation to ensure that the contributions from different parts of the crystal will add up constructively along the propagation direction. The same condition can also be stated in terms of the conservation of momentum between the interacting photons.

2.3 Phase matching and quasi-phase-matching

In the presence of phase matching, the efficiency of the nonlinear conversion will increase monotonically along the propagation direction. However, in the absence of phase matching, the interacting fields will accumulate a phase difference, causing the optical power to fluctuate between the interacting modes.

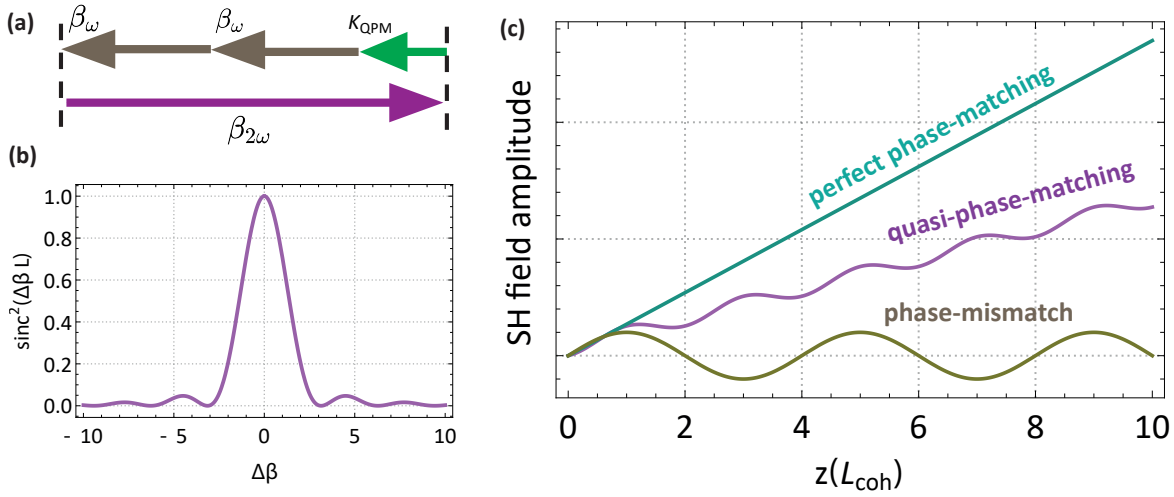

Figure 2.2: (a) A schematic representation of quasi-phase-matching in terms of propagation constants. (b) The $\text{sinc}^2(\Delta\beta L)$ term in the efficiency of SHG as a function of the phase mismatch for a fixed propagation length. (c) A schematic representation of how the SH field amplitude changes along the propagation direction under perfect phase matching, quasi-phase-matching and arbitrary phase-mismatch.

More specifically, once the waves have propagated over a specific coherence length proportional to the phase mismatch,

$$L_{coh} = \frac{2\pi}{\Delta\beta}, \tag{2.48}$$

the inverse process will be favored over the "forward" process. It can be readily seen from Equation 2.45, that the equation governing the inverse process to SHG differs only by a phase change [27]. This is shown in Figure 2.2(c).

Notably, if there were no sources of dispersion acting in the system, phase-matching conditions would always be satisfied. After all, the propagation constants would only be linear functions of the optical frequency, as in

$$\beta = n_{\text{eff}}\frac{\omega}{c}. \tag{2.49}$$

In reality, however, the effective index must be written as $n_{\text{eff}}(\omega)$, to indicate its dependence on the several sources of dispersion that exist in a dielectric waveguide.

In integrated photonics, it is often possible to engineer the device geometry to introduce new sources of dispersion to compensate for the phase mismatch, thereby achieving "modal" phase-matching. When this dispersion engineering is either impractical or impossible, the alternative is to implement quasi-phase-matching.

In quasi-phase-matching, the material properties of the nonlinear crystal are changed periodically to guarantee parametric gain. When the interacting fields accumulate a phase difference of π, such that the optical power is about to begin flowing back into the pump mode, the sign of nonlinear optical susceptibility is inverted. This is done by inverting the crystalline orientation along a given direction, effectively inverting the sign of d_{33} in Equation 2.45 [28].

The impact of this periodic modulation in the nonlinear efficiency is shown in Figure 2.2(c). The net effect on the nonlinear susceptibility is to create an "effective" coefficient d_{eff}, which differs from the original d_{33} by a factor of roughly $2/\pi$. In this sense, the cumulative quasi-phase-matching efficiency is limited to around 63% of the phase-matched case. This periodic inversion is referred to as Periodic Poling [29, 30, 31]. Its experimental implementation is a major point of interest for this project and will be discussed in detail in the subsequent chapters.

Chapter 3

Nonclassical States of Light

The quantum nature of light is the link tying this project together. It is the bridge between the platform and the application. Both integrated photonics and quantum information technology exist independently. The applications of integrated photonics go far beyond the use of nonclassical light, and much has been achieved in quantum information technology without recourse to photonics-based platforms. Yet, it is the quantum nature of light that allows these "fields" to intersect to form the subject matter of this project: integrated quantum photonics. In this chapter, we will introduce the basic formulation for a quantum theory of light and highlight the key properties of nonclassical states.

3.1 Quantization of the electromagnetic field

The quantization of the electromagnetic field is achieved in a relatively straightforward manner. Here, we will follow a procedure similar to the one often described in the literature [32, 33, 34, 35]. Before a mathematical formulation is introduced, it is useful to describe the process intuitively. In less rigorous terms, the field will be decomposed into its spectral components, and placed inside a closed cavity with periodic boundary conditions. Note that the volume of this cavity can later be taken to infinity to recover a continuous spectrum.

Once this is done, the total field is described as a superposition of modes with specifically allowed wavevectors, such that the total energy inside the cavity reduces to a sum over the amplitude contributions of each mode. By a change of variables, this total energy is shown to be equivalent to the Hamiltonian of a group of uncoupled harmonic oscillators, whose "position" and "momentum" phase space quadratures now correspond roughly to real and imaginary

parts of the electric field amplitude. Finally, the quantization is achieved by imposing canonical commutation relations to these quadratures, which become operators acting on a Hilbert space.

Now we proceed to a more rigorous description of the quantization process. For simplicity, we will employ Gaussian units, such that Maxwell's Equations are written as

$$\nabla \cdot \mathbf{B} = 0, \quad \nabla \times \mathbf{E} = -\frac{1}{c}\frac{\partial \mathbf{B}}{\partial t}, \quad \nabla \cdot \mathbf{E} = 4\pi\rho, \quad \nabla \times \mathbf{B} = \frac{4\pi}{c}\mathbf{J} + \frac{1}{c}\frac{\partial \mathbf{E}}{\partial t}, \tag{3.1}$$

and center the discussion on the vector potential $\mathbf{A}(\mathbf{r}, t)$. In the Coulomb gauge,

$$\nabla \cdot \mathbf{A}(\mathbf{r}, t) = 0, \text{ and } \Phi = 0 \quad \Rightarrow \quad \mathbf{E} = -\frac{1}{c}\frac{\partial \mathbf{A}}{\partial t} \text{ and } \mathbf{B} = \nabla \times \mathbf{A}. \tag{3.2}$$

In this case each plane wave solution for the vector potential is given by

$$\mathbf{A}(\mathbf{r}, t) = \hat{\mathbf{e}} A_0 e^{i(\mathbf{k}\cdot\mathbf{r} - \omega_k t)} + \text{c.c.}. \tag{3.3}$$

Now, by confining the electromagnetic field to a cube of edge length L and volume $V = L^3$, and imposing periodic boundary conditions, the allowed values for the wavevector become $\mathbf{k} = 2\pi n/L\hat{\mathbf{i}}$ where n is the set of all integers. Accordingly, the expansion for the vector potential will be given by

$$\mathbf{A}(\mathbf{r}, t) = \frac{1}{V}\sum_{\mathbf{k},s} \hat{\mathbf{e}} A_{\mathbf{k},s} e^{i(\mathbf{k}\cdot\mathbf{r} - \omega t)} + \text{c.c.}, \tag{3.4}$$

where s gives one of two polarizations for each direction $\mathbf{k}$. As stated before, we want to see the implications of this change to the expression of the total energy. In the general case, the energy of the electromagnetic field in a volume V is given by [36]

$$H_0 = \frac{1}{8\pi}\int_V \left[\mathbf{E}^2 + \mathbf{B}^2\right] d^3r. \tag{3.5}$$

by using Equation 3.4 for the confined vector potential and Equations 3.2 to write $\mathbf{E}$ and $\mathbf{B}$ in terms of $\mathbf{A}$, the total energy is rewritten as

$$H = \frac{V}{2\pi}\sum_{\mathbf{k},s} k^2 \left|\mathbf{A}_{\mathbf{k},s}\right|^2. \tag{3.6}$$

This result follows from direct substitution and use of the orthogonality relation between plane waves. Notice that the "quantization cavity" has given us a system whose energy comes from a sum over amplitude contributions of specific modes.

A clear physical interpretation arises once we define some additional quantities

$$p_{\mathbf{K},s}(\mathbf{r},t) = \sqrt{\frac{kV}{\pi\hbar c}}\mathrm{Im}\left[\mathbf{A}_{\mathbf{k},s}(\mathbf{r},t)\right], \text{ and } q_{\mathbf{K},s}(\mathbf{r},t) = \sqrt{\frac{kV}{\pi\hbar c}}\mathrm{Re}\left[\mathbf{A}_{\mathbf{k},s}(\mathbf{r},t)\right] \tag{3.7}$$

Notice that this particular choice of coefficients is such that the final form of the total energy is

$$H = \sum_{\mathbf{k},s}\frac{\hbar\omega_k}{2}\left[p^2_{\mathbf{k},s}(\mathbf{r},t) + q^2_{\mathbf{k},s}(\mathbf{r},t)\right] \tag{3.8}$$

which is identical to the Hamiltonian for a set of independent harmonic oscillators, whose "position" and "momenta" are given by $p_{\mathbf{k},s}$ and $q_{\mathbf{k},s}$. The natural consequence here is that the Hilbert space describing the quantized electromagnetic field is isomorphic to the Hilbert space of a quantum harmonic oscillator.

Notice that, by direct comparison to Equation 3.6, we can relate the amplitude $\mathbf{A}_{\mathbf{k},s}$ of each mode to a corresponding "number of photons" n, as in

$$n_{\mathbf{k},s} \leftrightarrow \frac{\omega_k}{2\pi\hbar c^2}|\mathbf{A}_{\mathbf{k},s}|^2 \quad \text{for} \quad n_{\mathbf{k},s} \gg 1 \tag{3.9}$$

Thus, we may think of photons as excitations to different modes of this quantum harmonic oscillator. The equivalence is taken further by defining creation and annihilation operators, which raise or lower the "population of photons" in a given mode, definable in terms of the quadratures in Equation 3.7, then

$$\hat{a}_{\mathbf{k},s}(\mathbf{r},t) = \frac{1}{\sqrt{2}}\left[\hat{q}_{\mathbf{k},s}(\mathbf{r},t) + i\hat{p}_{\mathbf{k},s}(\mathbf{r},t)\right], \tag{3.10}$$

$$\hat{a}^\dagger_{\mathbf{k},s}(\mathbf{r},t) = \frac{1}{\sqrt{2}}\left[\hat{q}_{\mathbf{k},s}(\mathbf{r},t) - i\hat{p}_{\mathbf{k},s}(\mathbf{r},t)\right]. \tag{3.11}$$

Note that the "hat" has been added to the notation to communicate that these quantities are now operators acting on the Hilbert space. Their behavior in this space follows from imposing the canonical quantization relation to $\hat{p}_{\mathbf{k},s}$ and $\hat{q}_{\mathbf{k},s}$, and consequently to $\hat{a}$ and $\hat{a}^\dagger$ as well,

$$[\hat{q}_{\mathbf{k},s}, \hat{p}_{\mathbf{k}',s'}] = i\delta_{\mathbf{k}\mathbf{k}'}\delta_{ss'} \quad \leftrightarrow \quad [\hat{a}_{\mathbf{k},s}, \hat{a}^\dagger_{\mathbf{k}',s'}] = \delta_{\mathbf{k}\mathbf{k}'}\delta_{ss'}. \tag{3.12}$$

From these definitions, it is straightforward to show that the Hamiltonian for the field is

$$\hat{H} = \sum_{\mathbf{k},s} \hbar\omega_k \left(\hat{a}_{\mathbf{k},s}\hat{a}^{\dagger}_{\mathbf{k},s} + \frac{1}{2} \right). \tag{3.13}$$

These results conclude the basic quantization of the electromagnetic fields. The state of the field is now described by a vector in Hilbert space where all the fields $\hat{\mathbf{E}}$, $\hat{\mathbf{B}}$ and $\hat{\mathbf{A}}$ are operators, defined in terms of the creation and annihilation operators, as in

$$\mathbf{A}(\mathbf{r},t) = \sum_{\mathbf{k},s} \sqrt{\frac{2\pi\hbar c}{kV}} \hat{a}_{\mathbf{k},s}\mathbf{e}_{\mathbf{k},s} e^{i(\mathbf{k}\cdot\mathbf{r}-\omega t)} + \text{h.c.}, \tag{3.14}$$

$$\mathbf{E}(\mathbf{r},t) = i\sum_{\mathbf{k},s} \sqrt{\frac{2\pi\hbar\omega_k}{V}} \hat{a}_{\mathbf{k},s}\mathbf{e}_{\mathbf{k},s} e^{i(\mathbf{k}\cdot\mathbf{r}-\omega t)} + \text{h.c.}, \tag{3.15}$$

$$\mathbf{B}(\mathbf{r},t) = i\sum_{\mathbf{k},s} \sqrt{\frac{2\pi\hbar\omega_k}{V}} \hat{a}_{\mathbf{k},s} \left(\mathbf{k}\times\mathbf{e}_{\mathbf{k},s}\right) e^{i(\mathbf{k}\cdot\mathbf{r}-\omega t)} + \text{h.c.}, \tag{3.16}$$

To further explore the Hilbert space where these operators live, it is necessary to define specific states. In the next section, it will be shown that this search leads us to a new class of states called "coherent states", defined by Roy Glauber in two seminal papers published in 1963 [37, 38].

3.2 Coherent states

In Equations 3.15 and 3.16, the **E** and **B** fields are defined in terms of the non-hermitian annihilation operator $\hat{a}_{\mathbf{k},s}$ and its hermitian conjugate. Following the usual procedure for the quantum harmonic oscillator, it would be natural to take this as motivation to define a new, hermitian operator

$$\hat{n}_{\mathbf{k},s} = \hat{a}^{\dagger}_{\mathbf{k},s}\hat{a}_{\mathbf{k},s}. \tag{3.17}$$

Which can act on a vector in Fock space to "count" the number of photons in a given mode. In other words, if a field defined by N modes with n_i photons in each mode is given by

$$|\{n_i\}\rangle = \prod_i \left(|n_1\rangle \otimes |n_2\rangle \otimes \ldots |n_N\rangle\right) \tag{3.18}$$

then the mean number of photons in a given mode j is given by $n_j = \langle\{n_i\}| \hat{a}^{\dagger}_j\hat{a}_j |\{n_i\}\rangle$.

At first sight, it would therefore be natural to claim that the operators defined hitherto live in Fock space. However, notice that **E** field in Equation 3.15 is a function of the annihilation operator $\hat{a}_{\mathbf{k},s}$. Yet, if the mean value of a is taken with respect to a Fock state, we get

$$\langle n|\, \hat{a}_{\mathbf{k},s}\, |n\rangle = 0. \tag{3.19}$$

Indeed, Fock states are not able to represent fields with classical-like properties, such as well-defined amplitudes and phases [33]. While they are useful to describe experiments that count discrete numbers of photons, they are not suitable to represent fields that might be measured in most experiments.

We are then motivated to search for a class of states which fulfills this task. Naturally, given the expressions for quantized **E** and **B** fields, one would expect these states to be eigenstates of the annihilation operator,

$$\hat{a}\,|\alpha\rangle = \alpha\,|\alpha\rangle\,. \tag{3.20}$$

Combining this property alone with a standard expansion of a general coherent state in the Fock basis,

$$|\alpha\rangle = \sum_n \langle n|\alpha\rangle\,|n\rangle\,, \tag{3.21}$$

it is possible to show that [39]

$$|\alpha\rangle = e^{-\frac{1}{2}|\alpha|^2} \sum \frac{\alpha^n}{\sqrt{n}}\,|n\rangle\,. \tag{3.22}$$

This implies that the mean number of photons in a coherent state is given by

$$\langle\alpha|\,\hat{n}\,|\alpha\rangle = \sum_n n p_n \quad \Rightarrow \quad p_n = e^{-|\alpha|^2}\frac{|\alpha|^n}{n!}. \tag{3.23}$$

In that sense, the coherent states are a Poissonian superposition of Fock states. In other words, they are composed of states with discrete numbers of photons.

Considerations about the statistics alone can also be used to define coherent states. Indeed, understanding this property is essential to motivate one of the central nonclassical states of interest to quantum information: squeezed states. To achieve this, we must introduce a pair of phase space variables describing a phase space and discuss their statistical properties.

3.3 Field Quadratures

So far, we have justified our interest in coherent states for their classical-like nature. As eigenstates of the annihilation operators, they are easily related to fields with well-defined amplitude and phase, as indicated by Equation 3.15. In fact, we have that,

$$\langle\alpha|\,\hat{a}\,|\alpha\rangle = \alpha. \tag{3.24}$$

Like any other complex quantity, the α parameter that completely determines a coherent state has an in-phase and an out-of-phase component. For any complex number z, we know that

$$\mathrm{Re}(z) = \frac{1}{2}(z + z^*) \quad \text{and} \quad \mathrm{Im}(z) = \frac{1}{2}i(z^* - z). \tag{3.25}$$

Thus, simply adjusting to our previous normalization choices, it is natural to define the following operators to "extract" the real and imaginary components of α out of a coherent state

$$\hat{X} = \left(\hat{a} + \hat{a}^\dagger\right), \quad \text{and} \quad \hat{Y} = i\left(\hat{a}^\dagger - \hat{a}\right), \tag{3.26}$$

which are dimensionless equivalents to the quadrature operators defined in Equation 3.10 and 3.11. These operators will inherit the commutation relation from $\hat{a}$ and $\hat{a}^\dagger$, such that, from Equation 3.12, it follows that

$$\left[\hat{X}_{\mathbf{k},s}, \hat{Y}_{\mathbf{k},s}\right] = 2i\delta_{\mathbf{k}\mathbf{k}'}\delta_{ss'}, \tag{3.27}$$

as expected for their equivalence to the "position" and "momentum" operators defined earlier. By taking the mean value of the operators with respect to a coherent state, the result is

$$\langle\alpha|\,\hat{X}\,|\alpha\rangle = 2\mathrm{Re}(\alpha) \quad \text{and} \quad \langle\alpha|\,\hat{Y}\,|\alpha\rangle = 2\mathrm{Im}(\alpha), \tag{3.28}$$

as expected from their definition.

Equation 3.28 indicates that measuring the field quadratures $\hat{X}$ and $\hat{Y}$ is equivalent to measuring the in-phase and out-of-phase components of α, thereby completely characterizing the coherent state. We are therefore motivated to suggest a phase space representation where $\hat{X}$ and $\hat{Y}$ are the coordinates. However, some considerations still must be made concerning the irreducible uncertainty of these measurements.

One can show that, given a pair of $\hat{A}$ and $\hat{B}$ observables [40],

$$\langle(\Delta^2\hat{A})\rangle\langle(\Delta^2\hat{B})\rangle \geq \frac{1}{4}\left|\langle[\hat{A},\hat{B}]\rangle\right|. \tag{3.29}$$

This follows directly from the Schwarz inequality and the definition of hermitian operators. Applying this to the dimensionless field quadratures using Equation 3.27, then

$$\Delta^2\hat{X}\Delta^2\hat{Y} \geq 1. \tag{3.30}$$

A coherent state implies in a particular distribution of uncertainty between the two quadratures. The variances of $\hat{X}$ and $\hat{Y}$ with respect to a coherent state can easily be computed to show that

$$\Delta^2\hat{X} = \langle\alpha|\,\hat{X}^2\,|\alpha\rangle - \left(\langle\alpha|\,\hat{X}\,|\alpha\rangle\right)^2 = 1. \tag{3.31}$$

In a similar way, it can be shown that $\Delta^2\hat{Y} = 1$.

Thus, coherent states represent a minimum uncertainty state, in which Equation 3.30 becomes an equality, and the uncertainty is equally distributed among the two quadratures.

Now, it is natural to represent the coherent field as a region in phase space, as shown in Figure 3.1. Indeed, it represents the smallest possible region, given that it minimizes the uncertainty relation. We show in Figure 3.1(b) a state with excess noise, and in Figure 3.1(c) a squeezed state, which is also a minimum uncertainty state, and will be discussed in the next section.

A field with excess noise and a squeezed state are also represented in Figure , as its properties will be discussed in the subsequent section

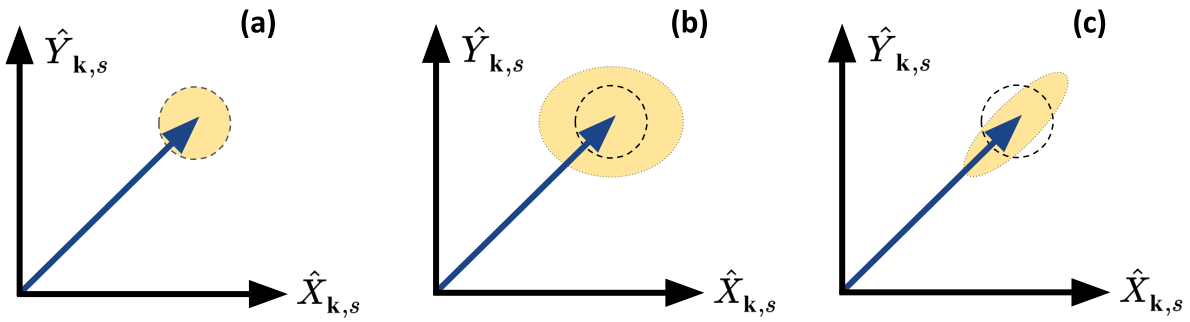

Figure 3.1: Phase space representation of a single mode of the quantized electromagnetic field. (a) a coherent state, representing minimum uncertainty displaced vacuum, (b) a state with excess noise in both quadratures, (c) a squeezed state, exhibiting minimum total uncertainty distributed unequally among the two quadratures

The quadratures represent real properties of the electromagnetic field and can be measured experimentally. A more general representation will include a rotation in phase space such that

$$\hat{X}_\theta = \hat{a}^\dagger e^{i\theta} + \hat{a}e^{-i\theta}, \text{ and} \tag{3.32}$$

$$\hat{Y}_\theta = i\left(\hat{a}e^{i\theta} - \hat{a}^\dagger e^{-i\theta}\right), \tag{3.33}$$

indicating that the quadratures can be connected by a simple phase space rotation of $\theta = \pm\pi/2$. Nevertheless, it is conventional to refer to $\hat{X}$ as the amplitude quadrature and to $\hat{Y}$ as the phase quadrature. This will become clearer once we note that, in the limit where the mean number of photons is much greater than the fluctuations in the quadratures $\alpha \gg \Delta\hat{X}$, the fluctuations $\delta\hat{X}$ do in fact correspond to fluctuations in the amplitude of a classical field.

3.4 Squeezed States

The manipulation of the statistical properties of quadratures of the electromagnetic field lies at the heart of continuous-variable quantum information [41, 42]. Squeezed states are a clear example of how nonclassical states can be defined by the characteristics of their field quadratures.

Conceptually, squeezed states can be understood by referring to Figure 3.1. In a squeezed state, the variance of one quadrature is decreased at the expense of increasing the variance of its counterpart [43]. While the total area is preserved, in compliance with the uncertainty principle stated in Equation 3.30, the amount of noise can be (in principle) arbitrarily reduced in a given quadrature of interest.

On their own, squeezed states offer important applications in quantum metrology. Reduced quadrature noise can increase the sensitivity of high-precision interferometers capable of detecting gravitational waves [44]. Similarly, squeezed states can enhance error correction protocols, enabling so-called "quantum limited" error correction and paving the way for fault-tolerant quantum computing [45, 46].

However, squeezed states are also building blocks in the preparation of other nonclassical states of light [47]. including entangled states and heralded single-photon sources [48]. This is the case because squeezed light can be generated with high efficiency and control via photon-pairs generated by Parametric Down Conversion (PDC) in experimental protocols

well-established since the 1980s [49, 50, 51]. Once these states have been created, additional "processing" such as linear-optical manipulation, interference, and selective measurement are sufficient to yield other nonclassical states.

Thus, in addition to being a useful tool on its own, squeezed light generation is also an indispensable tool for photonics-based quantum information. This project is heavily focused on the optimization of integrated platforms capable of realizing nonlinear optical processes suitable for the generation of such states. Naturally, a squeezing operator must "squeeze" the uncertainty of one quadrature and "stretch" its counterpart. It is possible to show that the operator

$$\hat{S}(\xi) = \exp\left(\xi \hat{a}^{\dagger 2} - \xi^* \hat{a}^2\right), \quad \xi = re^{i\phi}, \tag{3.34}$$

where r is the squeezing parameter, fulfills this task [48, 33, 35].

By decomposing this exponential using the Baker-Campbell-Hausdorff formula, and using the fact that $\hat{a}\,|0\rangle = 0$, the action of this operator on a vacuum state is found to be

$$|\xi\rangle = \hat{S}(\xi)\,|0\rangle = \frac{1}{\sqrt{\cosh(r)}} \exp\left(e^{i\phi} \tanh(r) \frac{\hat{a}^{\dagger 2}}{2}\right) |0\rangle\,. \tag{3.35}$$

This result can be combined with the properties of $\hat{a}$ and $\hat{a}^\dagger$ stated above to calculate the mean values of field quadratures with respect to this "squeezed vacuum state". After some manipulation, we arrive at

$$\Delta^2 \hat{X} = e^{2r} \quad \text{and} \quad \Delta^2 \hat{Y} = e^{-2r}, \quad \text{such that} \quad \Delta\hat{X}\Delta\hat{Y} = e^{2r}e^{-2r} = 1, \tag{3.36}$$

thereby preserving the minimum uncertainty property of coherent states, and redistributing uncertainty among quadratures without violating the uncertainty principle. Notice that the Hamiltonian describing degenerate Parametric Down-Conversion is [32, 52]

$$\hat{H} = \kappa\left(\hat{a}^2 - \hat{a}^{\dagger 2}\right), \tag{3.37}$$

such that the unitary evolution of a state subject to this Hamiltonian will be

$$\hat{U} = \exp\left(-i\kappa\left(\hat{a}^2 - \hat{a}^{\dagger 2}\right)\right) \tag{3.38}$$

which is identical to the squeezing operator shown above.

In this chapter we have introduced the basic concepts of quantum optics, culminating in a description of squeezed states in terms of field quadrature operators. These quadratures are at the center of continuous variable quantum information, and their manipulation is the central long-term motivation for the experimental work described in the following sections. As stated above, nonlinear optical processes are simply a platform for the experimental implementation of these transformations. In the following chapter, we will introduce a key resource for the efficient realization of such processes: the optical resonator, and its application as an optical parametric oscillator.

Chapter 4

Optical Parametric Oscillation

The Optical Parametric Oscillator (OPO) has been an important part of the photonics toolbox since its first demonstration in 1965 [53]. In simple terms, these machines combine the tunability, finesse, and power efficiency of optical resonators with the frequency-mixing capabilities of nonlinear optical processes. As a result, OPOs provide an excellent coherent and tunable light source for applications in imaging, spectroscopy, and quantum optics, among others.

In this chapter, we will describe the basic physics of optical resonators, culminating in a classical description of the Optical Parametric Oscillator. Finally, we will briefly discuss the quantum properties of the optical parametric oscillator, and show how they can lead to nonclassical states. This theoretical foundation will be used throughout this project in order to set the goals for microfabrication and to define the figures of merit for optical measurement.

4.1 Optical resonators

An optical resonator is an array of mirrors positioned in such a way that the incoming light is reflected by all the mirrors and then interacts back with the incoming beam. For all practical purposes, the terms “optical resonator”, “optical cavity”, and “Fabry-Perot resonator” are being used interchangeably. In this project, we will only fabricate integrated resonators in the shape of rings, although the theoretical description can be easily generalized for all shapes of cavities as long as they fall under the description given above.

Figure 4.1 shows a simple scheme for a general Fabry Perot cavity. The incoming field is partially transmitted and reflected by the first mirror, characterized by transmission and

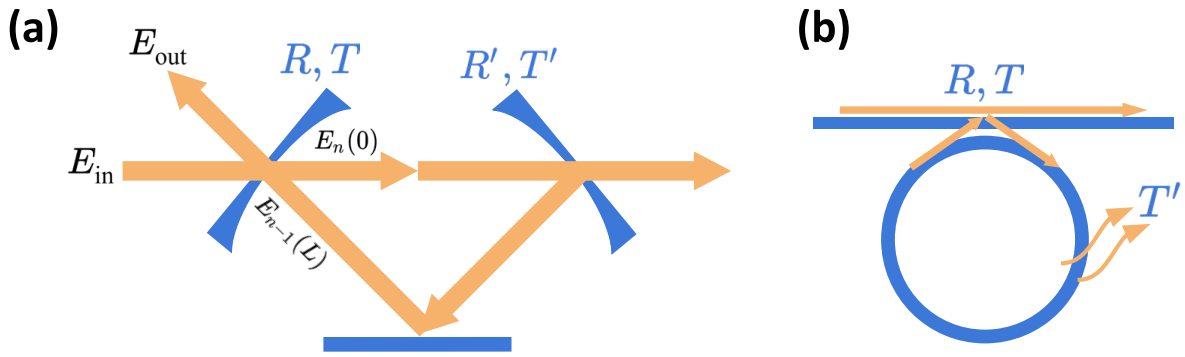

Figure 4.1: Scheme representation for the Fabry-Perot resonator. (a) An idealized system for modeling purposes, (b) the corresponding variables in the real system of interest, where light is coupled from a dielectric optical waveguide into a ring resonator.

reflection coefficients R and T. For this first mirror, transmission is equivalent to light entering the cavity, while reflected light never enters it.

Once inside the cavity, the light is reflected and transmitted across all the remaining mirrors according to coefficients R' and T'. The entire array of mirrors can be modeled by a single pair of coefficients, where T' now corresponds to light being permanently "lost". In a real system, this might refer to the combined effect of scattering losses induced by material roughness, or absorption losses defined by material properties. The total "reflection" of the cavity will therefore consist of the interference between a series of fields that have undergone different numbers of round trips around the cavity.

To describe this system mathematically, we first note that the incoming and outgoing fields undergo beamsplitter transformations in the first mirror [54, 55, 56],

$$E_{out} = \sqrt{T}E_{n-1}(L) - \sqrt{R}E_{in}, \quad \text{and} \quad E_n(0) = \sqrt{R}E_{n-1}(L) + \sqrt{T}E_{in} \tag{4.1}$$

where the arguments in parenthesis refer to a unidimensional position along the cavity's length.

We must study the changes in the field just after entering the cavity and just before leaving it. That is, to find the coefficient $T(L)$ such that $E_n(L) = T(L)E_n(0)$.

From physical considerations alone, we expect this coefficient to consider: (1) the phase shift due to propagation according to the wavevector $\beta = \mathbf{k} \cdot \hat{\mathbf{z}}$, (2) an amplitude attenuation along the propagation, defined as an exponential decay with coefficient α, and (3) losses due to imperfect reflection by the internal mirror. We expect (2) and (3) to be joined together in a

single term later on. With these considerations, we may write

$$E_n(L) = e^{i\beta(\omega)L} e^{-\frac{\alpha}{2}L} \sqrt{1-T'} E_n(0). \tag{4.2}$$

Now, we can expand the function $\beta(\omega)$ as a Taylor series centered on some resonance frequency ω_0 of the optical resonator. If the detuning is written as $\delta\omega = \omega - \omega_0$, then

$$\exp\left(i\beta(\omega)L\right) = \exp\left(iL\sum_{n=0}^{\infty}\beta^{(n)}\frac{\delta\omega^n}{n!}\right) = \prod_{n=0}^{\infty}\exp\left(i\beta^{(n)}(\omega_0)\frac{\delta\omega^n}{n!}\right). \tag{4.3}$$

By the very definition of a resonance frequency, we know that $\beta(\omega_0)L = 2\pi n$, where $n \in \mathbb{Z}$. Thus, by assuming that the system is operating near-resonance, we may consider only terms up to the first order in $\delta\omega$, such that

$$\exp\left(i\beta(\omega)L\right) = \exp\left(i\beta^{(1)}\delta\omega L\right) = \left(1 + i\beta^{(1)}\delta\omega L\right). \tag{4.4}$$

If a similar consideration is done to the attenuation coefficient α and to the transmission of the intracavity mirror T', then Equation 4.2 becomes

$$E_n(L) = \left(1 + i\beta^{(1}\delta\omega L\right)\left(1 - \frac{\alpha L}{2}\right)\left(1 - \frac{T'}{2}\right)E_n(0), \tag{4.5}$$

and if the multiplication is carried out and all second-order terms with respect to $\delta\omega$, α and T' (or their products) are discarded once again,

$$E_n(L) = \left(1 + i\beta^{(1)}\delta\omega L - \frac{1}{2}\left(T' + \alpha L\right)\right)E_n(0). \tag{4.6}$$

Finally, this result must be substituted back into the beam-splitter equation. To do this, we replace n by $n-1$ in the previous expression, such that

$$\begin{aligned} E_n(0) &= \sqrt{R}E_{n-1}(L) + \sqrt{T}E_{in}, \\ &= \left(1 - \frac{T}{2}\right)\left(1 + i\beta^{(1)}\delta\omega L - \frac{1}{2}(T' + \alpha L)\right)E_{n-1}(0) + \sqrt{T}E_{in}, \\ &\approx \left(1 + i\beta^{(1)}\delta\omega L - \frac{1}{2}(T + T' + \alpha L)\right)E_{n-1}(0) + \sqrt{T}E_{in}. \end{aligned} \tag{4.7}$$

This expression now allows us to write the total change in the field between two consecutive round-trips

$$\begin{aligned}\delta\omega E &= E_n(0) - E_{n-1}(0),\\ &= \left(1 + i\beta^{(1)}\delta\omega L - \frac{1}{2}(T + T' + \alpha L)\right) E_{n-1}(0) + \sqrt{T}E_{in} - E_{n-1}(0),\\ &= \left(i\beta^{(1)}\delta\omega L - \frac{1}{2}(T + T' + \alpha L)\right) E_{n-1}(0) + \sqrt{T}E_{in}.\end{aligned} \tag{4.8}$$

By defining a "total losses" term $l = (T + T' + \alpha L)/2$, then

$$\delta\omega E = \left(i\beta^{(1)}\delta\omega L - \frac{l}{2}\right) E_{n-1}(0) + \sqrt{T}E_{in}. \tag{4.9}$$

Since $\beta^{(1)}$ is the inverse of the group velocity, the factor $L\beta^{(1)}$ is equal to the total round-trip time t_R. By dividing the whole equation by t_R,

$$\frac{\delta\omega E}{t_R} = \left(i\delta\omega - \frac{\gamma}{2t_r}\right) E_{n-1}(0) + \sqrt{\frac{T}{t_R}}\frac{E_{in}}{\sqrt{t_R}}. \tag{4.10}$$

Now, we consider the limit where the number of round-trips is virtually infinite. We will redefine the loss terms to their quotients relative to the round-trip time, such that $\gamma \to l/t_R$ and $\gamma_{in} \to T/t_R$.

Finally, the intracavity field becomes dE and each round-trip time becomes dt, therefore

$$\frac{dE}{dt} = \left(i\delta\omega - \frac{\gamma}{2}\right) E + \sqrt{\gamma_{in}}E_{in}. \tag{4.11}$$

We can simplify this notation further by noting that the field intensity can be related to the average number of photons α by some coefficient, as in

$$E \propto \hbar\omega\alpha = K\alpha, \tag{4.12}$$

while the incoming field is written as

$$\alpha_{in} = \lim_{t_R \to 0}\left(K\frac{E_{in}}{\sqrt{t_r}}\right), \quad |\alpha_{in}|^2 = \frac{\bar{n}}{t_R} \tag{4.13}$$

where $\bar{n}$ is the mean number of photons. This leads to the final expression for the Fabry-Perot equation

$$\frac{d\alpha}{dt} = \left(i\delta\omega - \frac{\gamma}{2}\right)\alpha + \sqrt{\gamma_{in}}\alpha_{in}. \tag{4.14}$$

Most properties of interest arise when we consider the Fabry-Perot to be operating at the steady state, where $d\alpha/dt = 0$. In this case,

$$\alpha = \frac{\sqrt{\gamma_{in}}\alpha_{in}}{\left(\frac{\gamma}{2} - i\delta\omega\right)}, \tag{4.15}$$

and by also defining the total reflected field α_{out} and using 4.1, the total reflectance of the Fabry-Perot is

$$R_{FB} = \left|\frac{\alpha_{out}}{\alpha_{in}}\right|^2 = 1 - \frac{\mu\gamma_{in}}{\delta\omega^2 + \frac{1}{4}(\gamma)}. \tag{4.16}$$

In the interest of applications, it makes sense to distinguish between internal losses and coupling losses. Therefore, it is useful to separate the total losses term into $\gamma t_r = \gamma_i n + T' + \alpha L = \gamma_{in} + \mu$

$$R_{FB} = 1 - \frac{\mu\gamma_{in}}{\delta\omega^2 + \frac{1}{4}(\gamma_{in} + \mu)}. \tag{4.17}$$

This is an extremely relevant distinction, as the physical sources of γ_{in} and μ are quite distinct in real integrated ring resonators, even though their effect on the expression of the Fabry Perot reflectance is the same. The "coupling losses" γ_{in} are related to the strength of the coupling between waveguide and ring, as shown in Figure 4.1. This strength can be controlled by adjusting the distance between the two devices, and the phase matching and spatial overlap between the modes, which can be accurately modeled with Equation 2.43.

On the other hand, the internal losses μ are typically due to imperfections. Optical absorption can occur both due to intrinsic material properties, such as the bandgap energy of a material, and to imperfections in the crystalline structure, which might be mitigated by processes such as annealing. Additionally, scattering of the optical field will inevitably occur due to the roughness of the photonic devices. Both of these will contribute equally to the "total losses".

One important result of this section, is that μ and γ_{in} can in principle be measured separately. By simple inspection of Equation 4.17, we calculate

$$R_{min} = \left(\frac{\gamma_{in} - \mu}{bw}\right)^2, \quad \text{and} \quad bw = \gamma_{in} + \mu, \tag{4.18}$$

where R_{min} is the minimum reflectance of the resonator, and bw is the full width at half-maximum. Thus, by measuring R_{min} and bw, we can calculate γ_{in} and μ, but we can not tell them apart by just one measurement.

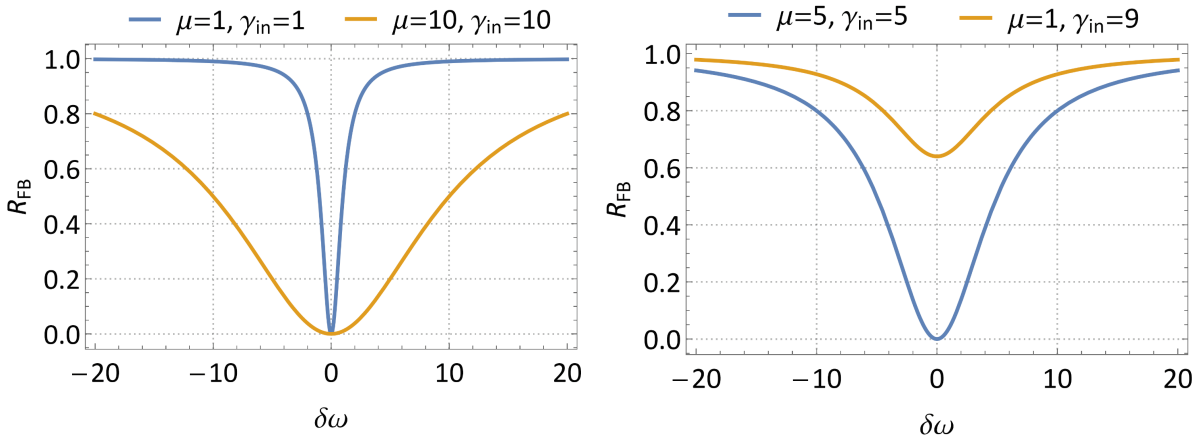

Figure 4.2: The reflectance of the fabry-perot as a function of detuning for different parameter combinations. The width of the Lorentzian curves depends only on the total losses γ, while the extinction ratio R_{min} depends on the difference between internal losses and coupling losses.

4.1.1 Figures of Merit

For a project focused on microfabrication, optical resonators offer one additional application: they greatly facilitate the assessment of fabrication quality regarding losses. As shown in the previous section, simply measuring the transmission of an optical resonator along a spectral region allows us to estimate losses of all kinds.

To interpret the results of such measurements, and to compare them with expectations, we must define a few figures of merit.

The Free Spectral Range (FSR) of the resonator is the spectral separation between adjacent resonance peaks. Since two consecutive resonances are characterized by

$$\beta(\omega_n)L = 2\pi n, \quad \text{and} \quad \beta(\omega_{n+1})L = 2\pi(n+1), \quad n \in \mathbb{Z} \tag{4.19}$$

we can calculate the FSR by subtracting the two equations,

$$\frac{\partial\beta}{\partial\omega}(\delta\omega)L = 2\pi. \tag{4.20}$$

Recalling the definition of the group velocity, and noting that $\delta\omega = 2\pi\text{FSR}$

$$\frac{\delta\omega}{v_g}L = 2\pi \Rightarrow \quad \text{FSR} \quad = \frac{c/n_g}{L}. \tag{4.21}$$

From then on, the *Finesse* of the resonator is defined as

$$\mathcal{F} = \frac{\text{FSR}}{bw}. \tag{4.22}$$

Notably, $\mathcal{F}$ is a measure of the resonator's ability to "trap" light. High finesse is related to sharp resonance peaks and consequently low total losses.

A second, more crucial figure of merit in characterizing losses on optical resonators, is the quality factor Q

$$Q = \frac{f_n}{bw}, \tag{4.23}$$

where f_r is a specific resonant frequency. The quality factor can also be defined as the ratio between the energy stored in an oscillator, and the energy dissipated by it per oscillation cycle. In the regime of low optical loss, the Q factor can be approximated as [57]

$$Q = \frac{2\pi f_0}{\gamma'}\frac{L}{c/n_g} \tag{4.24}$$

where γ' is the total *fractional* power loss per oscillation. Current state-of-the-art ring microresonators in lithium niobate, capable of achieving optical parametric oscillations with reasonable power threshold, exhibit intrinsic Q factor in the range of $6{\times}10^5$. Assuming operation at λ =1550nm in a resonator with a 100μm-radius, the necessary fractional loss to achieve this is $\gamma' \approx 0.85\%$.

4.2 Resonator-enhanced parametric down-conversion

Consider now that a non-centrosymmetric crystal is placed in the interior of the optical resonator. This crystal exhibits a second-order optical nonlinearity and may therefore enable processes such as second harmonic generation and parametric down-conversion, with efficiencies given by the formalism developed in Chapter 2.

In this section, we will briefly follow the procedure in [58] to show how the presence of this crystal changes the behavior of the optical resonator. The procedure is extremely similar

to that of the previous section. We will build on the same notation in order to facilitate the demonstration.

Parametric down-conversion describes an interaction between three optical modes: pump (α_0), signal (α_1), and idler (α_2). We must write equations for the evolution of all three. The interaction with the $\chi^{(2)}$ nonlinear crystal will change the fields such that

$$\bar{\alpha}_0 = \alpha_0 \exp(i\beta_0 L_c) - 2\chi^*_{eff}\alpha_1\alpha_2 \exp((\beta_1 + \beta_2)L_c) \tag{4.25}$$

$$\bar{\alpha}_1 = \alpha_1 \exp(i\beta_1 L_c) + 2\chi_{eff}\alpha_0\alpha^*_2 \exp((\beta_0 - \beta_2)L_c) \tag{4.26}$$

$$\bar{\alpha}_2 = \alpha_2 \exp(i\beta_2 L_c) - 2\chi_{eff}\alpha_0\alpha^*_1 \exp((\beta_0 - \beta_1)L_c) \tag{4.27}$$

Where χ_{eff} is a coefficient contemplating the efficiency of the nonlinear interaction and L_c is the optical length of the crystal. The remaining round-trip will have the same effect on all fields,

$$\bar{\bar{\alpha}}_i = \sqrt{R'_i R_i} \exp\left(i\omega_i \frac{L - n_c L_c}{c}\right) \bar{\alpha}_i + \sqrt{T_i}\alpha_i^{(in)}. \tag{4.28}$$

As in the previous case, the resonance condition comes down to $\bar{\bar{\alpha}}_i = \alpha_i$. To solve this, we simply plug Equations 4.25,4.26, and 4.27 into Equation 4.28.

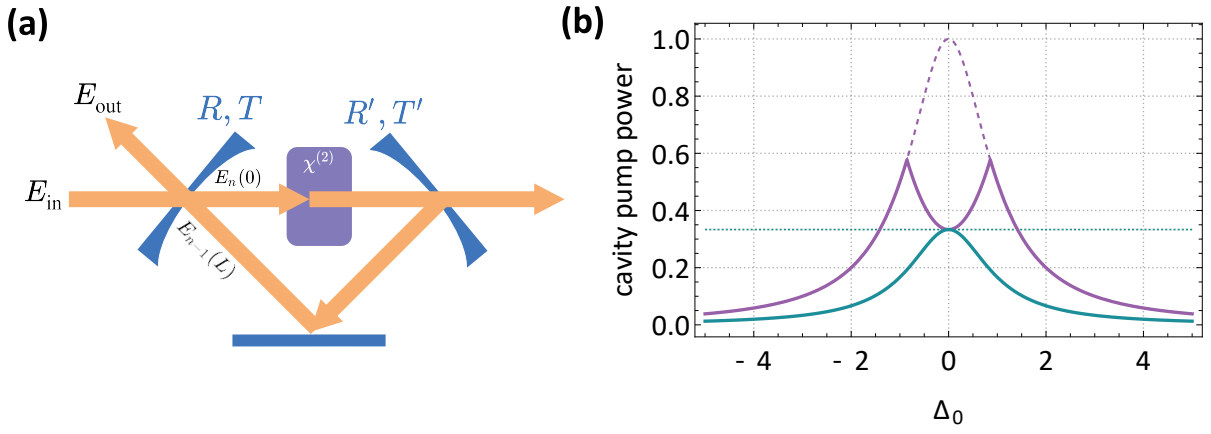

Figure 4.3: (a) An optical parametric oscillator modeled as a Fabry-Perot Cavity with a nonlinear optical crystal in its interior. (b) The total intracavity pump power as a function of detuning for an OPO. The dashed horizontal line indicates the threshold power. Below the threshold level, the OPO behaves as a completely linear cavity. Above the threshold, all the resonant pump power is converted into signal and idler modes. The dashed purple line indicates the expected behavior in the absence of nonlinear optical effects.

The solution is obtained by expanding the propagation coefficients around a resonance, and taking terms up to first-order with respect to detuning, total losses, and coupling losses.

After some manipulation, the equations will be reduced to

$$\alpha_0\gamma_0\left(1 - i\delta\omega_0'\right) = -2\chi^*\alpha_1\alpha_2 + \sqrt{2\gamma_{in}}\alpha_0^{(in)}, \tag{4.29}$$

$$\alpha_1\gamma_1\left(1 - i\delta\omega_1'\right) = 2\chi\alpha_0\alpha_2^*, \quad \alpha_2\gamma_2\left(1 - i\delta\omega_2'\right) = 2\chi\alpha_0\alpha_1^*. \tag{4.30}$$

Where $\delta\omega_i' = \delta\omega_i/\gamma_i$ are the detunings normalized by total losses.

The last two equations form a linear system that always admits a trivial solution $\alpha_1 = \alpha_2 = 0$. However, there is a range of values for which nontrivial solutions exists. In these cases, nonlinear gain supersedes losses at each round-trip, and power is effectively transferred between optical modes.

Multiplying Equation 4.26 by the complex conjugate of Equation 4.27,

$$\alpha_1\gamma_1(1 - \delta\omega_1')\alpha_2^*\gamma_2(1 + i\delta\omega_2') = 4|\chi|^2\alpha_1\alpha_2^*|\alpha_0|^2, \tag{4.31}$$

dividing by $\alpha_1\alpha_2$ (thus assuming $|\alpha_1|, |\alpha_2| \neq 0$), and taking the imaginary part,

$$(\delta\omega_1' - \delta\omega_2')\gamma_1\gamma_2 = 0. \tag{4.32}$$

Thus, the solution only exists when $(\delta\omega_1' - \delta\omega_2') = \delta\omega' = 0$. That is, the normalized detuning must be the same for the generated fields in order for oscillation to occur. Now taking the real part of 4.31

$$\gamma_1\gamma_2(1 - \delta\omega'^2) = 4|\chi^2||\alpha_0|^2. \tag{4.33}$$

Therefore, when oscillation occurs, the intracavity pump field is given by

$$|\alpha_0|^2 = \frac{\gamma_1\gamma_2(1 + \delta\omega'^2)}{4|\chi|^2}. \tag{4.34}$$

In other words, the power in the pump mode is constant above the threshold. Now, finally, the threshold can be calculated by plugging this result into Equation 4.25,

$$|\alpha_0^{(in)}|_{th}^2 = \frac{\gamma_0^2\gamma_1\gamma_2}{8|\chi|^2\gamma_0}(1 + \delta\omega^2)(1 + \delta\omega_0^2). \tag{4.35}$$

Equation 4.35 gives the threshold of incident pump power above which the oscillation begins to occur. Since the pump power inside the cavity is constant above this level, we know

that all additional optical power will be converted into signal and idler modes. These properties are shown in Figure 4.3, where the total pump power inside the oscillator is shown as a function of detuning. The oscillation threshold is shown as a dashed horizontal line.

In practical terms, it is relevant to note that the threshold power in Equation 4.35 increases with the square of the total pump losses. For an integrated optical resonator, this means that high-loss microfabrication will require the use of high optical powers in order to reach parametric oscillation. This power is often limited both by the availability of sources and by the insertion losses of photonic chips.

Optical Parametric Oscillators have been used since 1965 [53] to enhance optical parametric processes. As opposed to a "single-pass" system such as an Optical Parametric Amplifier (OPA), the OPOs allow for the conversion to be finely tuned by adjusting phase matching conditions. Furthermore, the optical resonator allows for higher optical intensity to accumulate in the nonlinear material, increasing the conversion efficiency.

As a photon-pair source, the Optical Parametric Oscillator has proven to be the "most efficient source of quadrature squeezed light" [47]. As discussed in section 3.4, this has consolidated the OPO as a widely-used nonclassical light source, being implemented for multiple applications, including quantum random number generation [59], quantum cryptography [60] and simulation [61, 62].

Chapter 5

Experimental Methods

In the previous chapter, the use of integrated photonic devices for the generation of nonclassical states of light has been thoroughly justified, modeled, and explained. Here, I will introduce the essential experimental methods chosen for our contribution to this major scientific and technological challenge.

In the first section, the choice of Lithium Niobate as a material platform will be justified, both by the material properties themselves and by the current state-of-the-art in literature. In the second section, we present a general overview of the necessary tools for microfabrication on $LiNbO_3$. Next, we discuss methods for fiber-to-chip coupling of light. Finally, a technique to measure continuous variables in nonclassical light will be discussed.

5.1 Lithium niobate: the silicon of photonics

Lithium Niobate ($LiNbO_3$) is an artificial ferroelectric crystal, synthesized for the first time in 1949 [63]. In the past decade, it has been described as "the silicon of photonics" [64]. To put it simply, this is because its material properties enable the efficient implementation of a diverse set of useful processes for information technology. In this section, we will describe in greater detail what these properties are, which specific implementations have been enabled by them, and how they compare to other relevant materials.

An ideal candidate for a material platform for integrated photonics should fulfill several requirements. Some of the most common properties of interest for photonic integrated circuits, both for classical and quantum applications, are:

- **Wide transparency window**: transparency in key regions enables low loss transmission of light, due to limited material absorption. Several factors play a role in determining a material's transparency, including the presence of defects and impurities, Two-Photon Absorpition (TPA), the vibrational modes of the crystalline structure, and the bandgap energy. The latter is often used as a good figure of merit for assessing the transparency of the material. Large bandgap energy means higher-frequency photons can propagate in the material without being absorbed to excite electrons to the conductance band.

- **Large refractive index**: the refractive index contrast between core and cladding materials in a dielectric waveguides sets the level of optical confinement. This will enhance the optical intensity in the nonlinear material, contributing to more efficient nonlinear optical effects.

- **Large $\chi^{(2)}$ and $\chi^{(3)}$ nonlinearities**: the $\chi^{(2)}$ coefficient sets the efficiency of second-order nonlinear processes like SHG, PDC, SFG and DFG. Similarly, $\chi^{(3)}$ coefficients set the efficiency of third-order nonlinear processes such as Self-Phase Modulation (SPM), Cross-Phase Modulation (XPM) and Four-wave Mixing (4WM). A material exhibiting large values for both coefficients can enable for versatile frequency-mixing processes by combining second and third-order nonlinear effects.

- **Large Pockels coefficient**: the Pockels coefficients are second-order ($\chi^{(2)}$) properties which set the efficiency of electro-optic interaction. This is a crucial asset for high-speed electro-optic modulation of light and microwave-optical photon transduction, which are crucial for applications at the interface between electronics and photonics.

- **Large piezoelectric coefficients**: this coefficient determines the efficiency of piezoelectric effects, where an applied electric field induces mechanical strain in a material, or vice-versa. This is a crucial property for applications in acousto-optics, such as Surface Acoustic Wave (SAW) devices and filters.

- **Ease of processing**: the effectiveness of standard microfabrication processes will heavily rely on material properties such as chemical reactivity, electrical conductivity, and endurance to stress and temperature. Compatibility with Complementary Metal-Oxide-

Semiconductor (CMOS) technology is also extremely attractive for easy integration will well-established CMOS microelectronic chips and scalable fabrication techniques.

Countless applications can be unlocked by any single one of these properties. However, a balanced combination of many or all of them will make for a better material for integrated photonics. Table 5.1 shows the parameter values for a series of common photonic materials. The data supports the characterization of lithium niobate as a highly versatile and efficient photonic material.

	AlN	**Si**	**Si_3N_4**	**TFLN**	**GaAs**
bandgap (eV)	6.2	1.1	5.0	4.0	1.4
refractive index	2.08(e)	3.48	2.00	2.21(e)	3.38
$\chi^{(2)}$ (pm/V)	6.2	0	0	54	237
$\chi^{(3)}$ ($10^{-19}m^2/W$)	3.5	40	2.4	1.0	260
Pockels coefficient (pm/V)	1.0	0	0	30.9	1.5
piezoelectricity (pC/N)	5.5	0	0	68	2.7

Table 5.1: Table comparing the material properties of common photonic materials [65]. When applicable, the parameters shown correspond to 1550nm wavelengths and room temperature.

Materials can have countless advantages and disadvantages beyond these parameters. For instance, III-V materials such as GaAs and InP are compatible with highly-developed semiconductor laser technology, allowing for the integration of electrically-driven pump sources [66]. Likewise, silicon Nitride exhibits excellent CMOS compatibility, both due to its similarity with standard CMOS materials like silicon and silicon dioxide, and because it can be deposited via Chemical Vapor Deposition (CVD) processes, such as Plasma Enhanced Chemical Vapor Deposition (PECVD). Thus, a multitude of factors must be taken into account while determining a suitable material platform for photonic applications.

Nevertheless, lithium niobate has proven to be a widely applicable material for both classical and quantum applications [12]. Its use can clearly be separated into three major technological generations: bulk $LiNbO_3$, weakly confining $LiNbO_3$ waveguides, and tightly confining Thin-Film Lithium Niobate (TFLN) waveguides. These generations were enabled by specific technological improvements, as described in Table 5.2.

The improvements between each generation are typical of the miniaturization process that has defined the field of integrated photonics. Namely, increased optical confinement leads

Generation	Years	Enabled by	Dimensions
Bulk LN	1960s-1970s	synthesis of $LiNbO_3$ [63], optical grade polishing	1mm-1cm
weakly confining LN waveguides	1970s-2010s	ion-diffusion [67], proton exchange [68]	1μm-1mm
tightly confining TFLN waveguides	2010s-now	crystal ion slicing [69], wafer bonding, Ar milling [70]	<1μm

Table 5.2: The three major generations of photonic devices in Lithium Niobate. While 680nm lithium niobate thin-films are fabricated since 2004, most successful results in the current generation of devices follow the use of Ar ion milling beginning in 2009.

to orders-of-magnitude improvements in nonlinear efficiency and reduces device footprint. Miniaturization also enables scalable fabrication and great environmental stability compared to free-space optical setups. Additionally, microfabrication of the devices unlocks additional degrees of freedom in device geometry, paving the way for highly versatile design through dispersion engineering.

Benchmark	Year
Periodic poling in TFLN	2016 [71]
TFLN electro-optic modulator with CMOS compatible voltage	2018 [72]
On-chip heralded single-photon generation	2020 [4]
On-chip TFLN optical parametric oscillator	2021 [73]
Ultra-low TFLN loss waveguides (<1 db/m)	2022 [74]
Quadrature squeezing in TFLN OPA	2022 [7, 6]

Table 5.3: Major benchmarks in the construction of a toolbox for (3rd generation) Integrated Photonic Circuits on Thin-Film Lithium Niobate (TFLN). The years presented refer to the first demonstration of each benchmark, to the best of my knowledge.

Across its generations, Lithium Niobate has found several applications, greatly impacting both research and industry environments. In the telecommunications industry, it is widely used for electro-optic modulation in fiber-optics communication [75], enabled by its large Pockels coefficient. As a piezo-electric material, it is used for surface acoustic wave devices, acting as filters and resonators in wireless communication systems [76], and as sensors and actuators in medical and industrial settings [77]. In Table 5.3, it is clear that recent results in the current generation of TFLN devices are quickly evolving toward a toolbox for integrated

quantum photonics, thus qualifying Lithium Niobate as a major platform for quantum information technology [3, 9].

In this section, I have presented the historical and scientific context justifying the use of lithium niobate in this project. In the next section, I will briefly address the basic microfabrication tools that define our work with this material.

5.2 Microfabrication tools and techniques

The miniaturization of integrated circuits, famously captured by Gordon Moore's 1965 predictions [78], has been one of the major technological achievements of the past century. As the number of devices per microchip has grown by at least six orders of magnitude over the past five decades, so grew the processing power, scalability, cost-effectiveness, and stability that define the current generation of information technology. Such remarkable progress has been enabled by a myriad of innovations in chemistry, materials science, optics, computer science, and more [79]. The set of processes and techniques arising from these innovations constitute the field of microfabrication.

Technology	Equipment	Facility
Electron Beam Lithography	Raith eLine	CCSNano LNNano (CNPEM)
Photolithography	Microwriter ML3 Pro Karl Suss MJB3	CTI CCSNano
ICP-RIE	Oxford Plasmalab 100 Oxford Plasma Pro NGP80	CCSNano LNNano
SEM	SEM Hitachi S-3400N FEG-SEM Tescan Mira 3 MXU Jeol JSM 6340 F	CCSNano CTI IQ/Unicamp
Atomic Force Microscopy	Nanosurf EasyScan2 Flex	Lamult
Thin-film Measurement	Filmetrics F54	CCSNano
Surface Profiler	Dektak 150 Veeco Dektak DXT S Bruker	Lamult LNNano (CNPEM)
EBPVD	AJA ATC2200-HY	LFDQ
Dicing Saw	DAD3220	CNPEM

Table 5.4: Main microfabrication tools and facilities used in this project. No single facility possesses all the necessary tools. Acronyms in the table refer to Inductively Coupled Plasma Reactive Ion Etching (ICP-RIE), Electron Beam Physical Vapor Deposition (EBPVD) and Scanning Electron Microscope (SEM).

Photonic Integrated Circuits (PICs) have inherited much of the microfabrication technology used in microelectronics. In both cases, the process is centered on optical and electron-beam lithography, dry and wet etching, and chemical and physical deposition. The assessment of fabrication quality is done with techniques such as scanning electron microscopy, atomic force microscopy, thin-film measurement, optical microscopy and surface profiling. Finally, the post-processing of samples generally includes a combination of cleaving, dicing saw cuts, and Chemical-Mechanical Polishing (CMP).

As a project centered on the development of a TFLN microfabrication recipe from scratch, a major component of this work lies in adapting established techniques to local cleanroom infrastructure. The details of this process and the particularities of each technique are, therefore, at the core of this project's contributions, and will be discussed in the subsequent chapters. The main techniques and tools used for this project are shown in Table 5.4, as well as the facilities where they are located.

In addition to the facilities of Device Research Laboratory (LPD) (both for cleanroom processes and optical setups), the facilities used in this project (and mentioned in Table 5.4) were the Center for Semiconductor Components (CCSNano), the National Nanotechnology Laboratory (LNNano), Renato Archer Information Technology Center (CTI), Multiuser Laboratory at the Gleb Wataghin Physics Institute (Lamult), Physics of Quantum Devices Laboratory (LFDQ/Unicamp), National Center for Research in Energy and Materials (CNPEM), and the Institute of Chemistry at the University of Campinas (IQ).

Chapter 6

Photonic Design with Finite Element Method Simulations

Computational modeling of electromagnetic fields is a crucial element in the development of photonic integrated circuits. Dispersion properties, the efficiency of nonlinear optical processes, and the flow of optical power through different paths can all be manipulated and fine-tuned by careful design of device geometry.

As the attention paid to TFLN devices by the scientific community soared, an immense amount of simulation results were published over the past decade [80, 81, 11]. Consequently, the basic design features and fabrication requirements for most applications of TFLN devices are very clear and well-established. Therefore, as a first-generation project in our local context, we have been focused on achieving the basic fabrication capabilities for a wide range of applications, rather than realizing any specific design.

Nevertheless, in this chapter, we will present some relevant results that independently verify and set benchmark goals for microfabrication. These results also provide an important foundation for future group efforts to develop and refine specific applications of TFLN PICs.

6.1 Photonic design with the Finite Element Method

For computational purposes, optical ring resonators will be modeled as bent waveguides with periodic boundary conditions. The frequency components of the electric and magnetic fields

are then given by

$$\mathbf{E}(\mathbf{r},\omega) = \sum_m A_m(\omega)\mathbf{F}_m(x,y,\omega)e^{i\beta_m(\omega)z}, \quad \mathbf{H}(\mathbf{r},\omega) = \sum_m A_m(\omega)\mathbf{G}_m(x,y,\omega)e^{i\beta_m(\omega)z}, \tag{6.1}$$

which can be computed numerically using the Finite Element Method (FEM) as implemented by the COMSOL Multiphysics software ©. In this case, Maxwell's Equations (as shown in Chapter 2) are solved for the specific geometry and material properties [1] of photonic devices, assuming only linear polarization.

The spatial field modes $\mathbf{F}(x,y,\omega)$ and $\mathbf{G}(x,y,\omega)$ are the normalized eigenfunctions, and the propagation modes $\beta_m(\omega)$ are the eigenvalues which can be computed to completely describe the unperturbed system. From then on, well-established models of interactions between optical modes in integrated devices [25, 22, 15] (described in detail in Chapter 2) can be used to compute the efficiency and characteristics of processes introduced by those perturbations.

These include primarily the nonlinear polarization, but also other perturbations such as gratings and the presence of adjacent waveguides. These interactions between optical modes are modeled in Equation 6.1 by the changes in amplitudes $A_m(\omega,z)$ along the propagation direction.

In simple terms, the Finite Element Method is a strategy for solving partial differential equations [84]. In our case, the time derivatives appearing in wave equations are computed by reference to frequency components, such that only spatial variables remain. Then, the space is divided into smaller parts defined by an adjustable mesh, i.e. the "finite elements". For a steady-state problem such as the one we are interested in, the partial differential equation is approximated by an algebraic equation in each of these smaller elements. Later, these equations are assembled into a larger system of equations that can be solved with well-known computational methods to model the entire problem [2].

[1] As a general rule, supplying the program with an analytic expression, such as the Sellmeier equation for the refractive index as a function of wavelength and temperature, as found in [82, 83] is sufficient.

[2] In our implementation in COMSOL Multiphysics ©, the boundary conditions are defined by so-called Perfectly Matched Layers (PML) [85].

6.2 Phase-matching conditions

In Figure 6.1, the phase mismatch for second harmonic generation between fundamental TM modes (TM_{00}) is computed for a series of waveguide widths in a wavelength range of around 1500 nm.

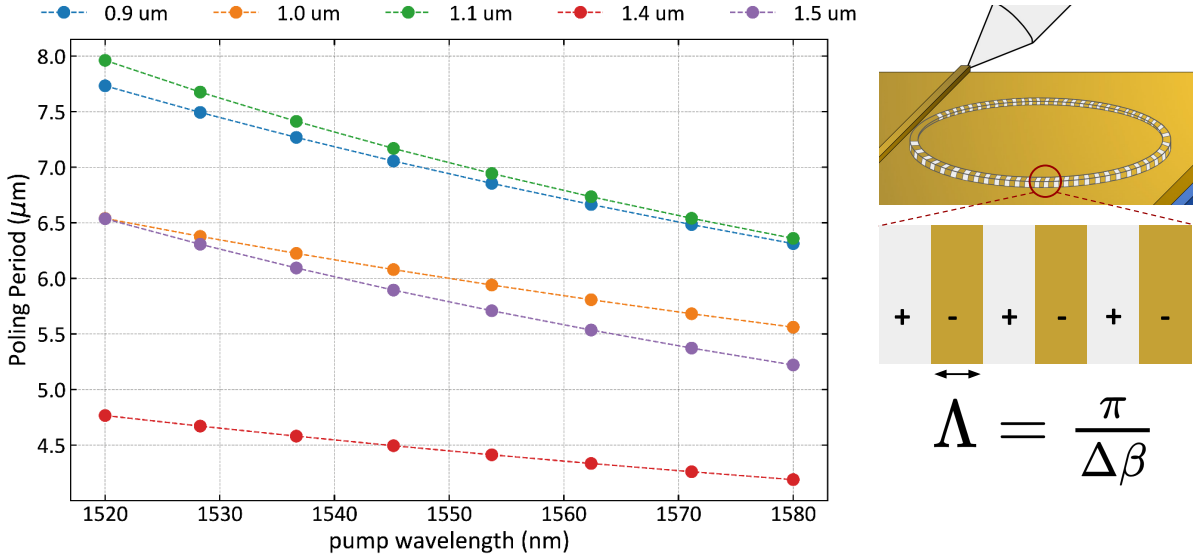

Figure 6.1: Finite Element Method simulation of the necessary poling periods for Second Harmonic Generation (TM_{00}-TM_{00} for different waveguide widths. In all cases, we simulate an air-cladded device, with an etching depth of 300 nm, over a 100 nm lithium niobate layer, and a 75° sidewall angle (typical value in literature).

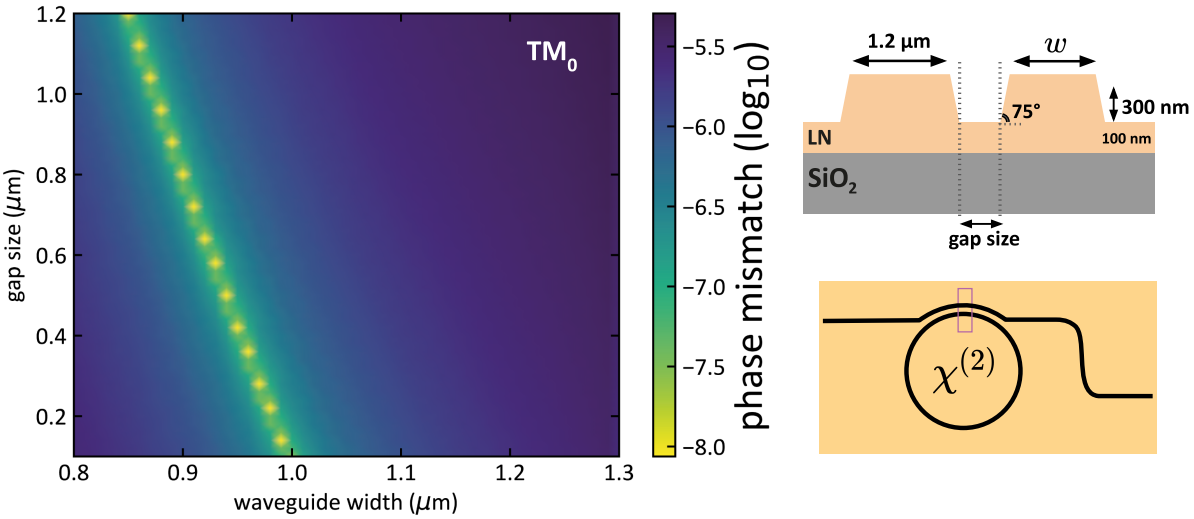

Figure 6.2: An example of a simulation to determine the necessary feature resolution for the microfabrication process. Phase matching between waveguide and ring resonator can be achieved with gaps larger than 300 nm for waveguide widths larger than 900 nm.

The phase mismatch values are then used to compute the necessary spatial periodicity of the ferroelectric domain inversion process (periodic poling). We find that, in the most challenging scenarios, a spatial resolution of about 4 microns must be achieved in the periodic poling of lithium niobate.

Figure 6.2 shows a simulation of phase mismatch for several geometries of a ring resonator-to-waveguide coupler. Here, each of the devices (ring and waveguide) is simulated as a separate bent waveguide with a slightly different radius. In order to compute the coupling coefficients, it is necessary to also calculate the modes when both devices are present, since they act as perturbations to each other due to the penetration of evanescent fields. Nevertheless, in this simulation, only the phase mismatch between the two separate devices is computed, in order to estimate the necessary feature resolution for efficient coupling. In future processes, the design must be finely tuned to the specific application.

We find that, for waveguide widths larger than 900 nm, efficient coupling can be achieved with gap sizes larger than 300 nm. Thus setting an upper bound for the desired feature resolution to be accomplished in the fabrication process. These results will be used as initial benchmarks for the optimization of our fabrication recipe. It will be shown that all of these requirements have been achieved experimentally, thus creating a powerful toolbox for experiments with photonic integrated circuits.

Chapter 7

Microfabrication of Lithium Niobate Photonic Devices

In this chapter, I will present the main experimental results of this project, which are centered on the development of a microfabrication recipe for PICs in thin-film lithium niobate.

As a relatively new and challenging material platform, the fabrication of such devices has been heavily centered in developed countries. In this sense, the efforts described in this chapter are largely concerned with realizing key benchmarks of TFLN fabrication in local cleanroom infrastructure. Indeed, the devices yielded by the final process are, to the best of our knowledge, the first of their kind in Latin America. As such, their development has required extensive adaptation and experimentation, which are not always easily captured in systematic writing.

7.1 Remarks about developing a recipe from scratch

At first sight, the general techniques for fabrication in Thin-Film lithium niobate are well-established in the literature [86, 74]. However, identifying the specific parameters of each technique can be a huge challenge, and several significant limitations of local cleanroom infrastructure had to be overcome. As a result, processes reported in the literature can only very rarely be reproduced with major adaptation.

Furthermore, given a finite amount of time, a pragmatic approach to optimization must be adopted. Since the validation of the process as a whole requires all steps to reach a minimum working level, the optimization of each step must be truncated at some reasonable point. Thus,

the "final" process proposed in this project is only final in the sense that it yields working results and sets a starting point and direction for future improvement. It must not be understood as an optimal process.

It is also important to note that techniques in microfabrication generally involve interactions between complex systems, which can rarely be modeled precisely. Thus, each iteration of an optimization process is often reduced to an "informed" trial and error loop, based on reference to the relevant literature, physical intuition, and direct previous experience.

It must also be noted that the implementation of a process requires a specific sequence of several tools and steps. In order to optimize a single step, all the preceding ones must be executed again for every single iterations. There are several consequences to this fact: (1) long time intervals are often unavoidable between consecutive iterations; (2) samples have to be transported between different facilities in order to access the necessary tools, as shown in Table 5.4; and (3) reproducibility must be ensured along all preceding steps to allow conclusions to be drawn from each iteration.

All of these factors ensure that the development of microfabrication recipes from "scratch" is a highly sinuous and time-consuming process. Given a finite amount of time, external factors such as equipment malfunction as well as scheduling and resource limitations will often override technical and scientific considerations for some experimental choices.

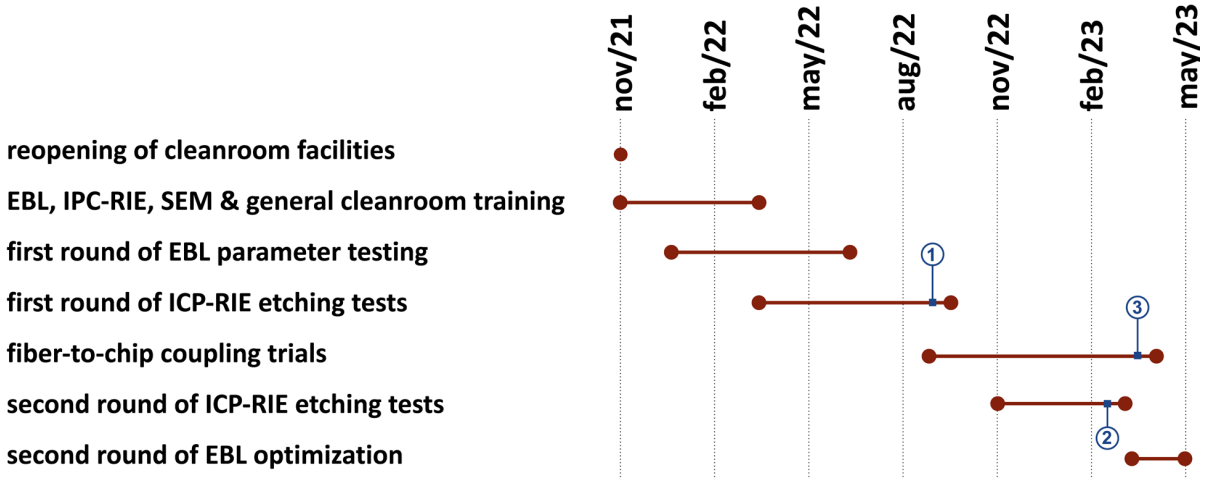

Figure 7.1: Timeline and table of main benchmarks in the development of microfabrication and post-processing recipes. Circled numbers 1-3 indicate cross-references with Table 7.1

Figure 7.1 shows a timeline of the benchmark achievements in the recipe development process, clearly illustrating its nonlinear nature. Notice that optimization rounds for each technique progress until specific benchmarks are attained. The specific dates of each of these

achievements are shown in Table 7.1, which provides a clear picture of how the process unfolded over a period of seventeen months.

Date		Fabrication and Processing Benchmarks
2021	**Nov 20th**	First 30kV EBL round in TFLN sample at CCSNano
	Dec 9th	First round of ICP-RIE argon based etching of TFLN
2022	**Feb 21st**	First realization of electric-field induced periodic poling of TFLN
	May 11th	First successful trial of fiber-to-chip coupling setup with Si_3N_4 chip from foundry
	Jun 28th	First fabricated TFLN resonator. 80 nm-deep etching achieved at 0.16 selectivity
	Aug 24th	First sucessful development of 100 nm features with EBL
	Aug 29th	120 nm-deep etching achieved at 0.40 selectivity at 0.2 nm/s etch rate (1)
	Sep 14th	First Au lift-off on TFLN sample using EBL
	Nov 11th	First execution of aligned dicing saw cuts in TFLN samples for edge coupling
2023	**Mar 28th**	300 nm-deep etching achieved at 0.63 selectivity and 0.8 nm/s etch rate (2)
	Apr 19th	First coupling of light into locally fabricated TFLN device
	Apr 25th	First characterization of TFLN optical resonator (3)

Table 7.1: Table of main benchmarks in the development of the microfabrication recipe during a seventeen-month period. Circled numbers indicate cross-references with Figure 7.1.

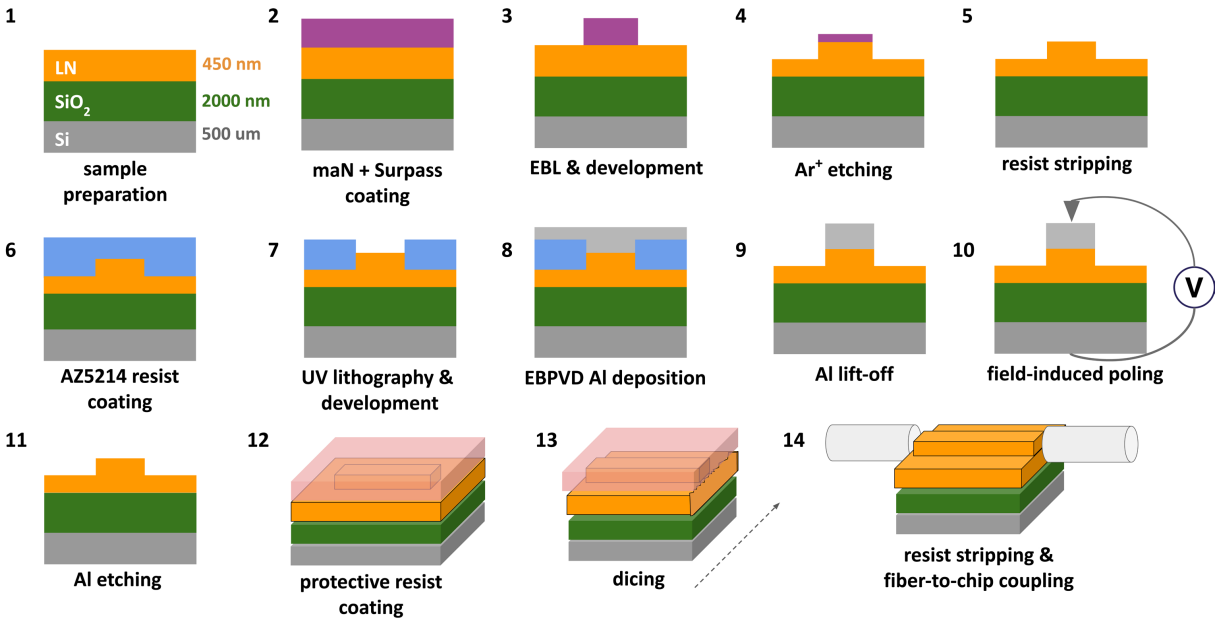

Figure 7.2: A diagram outlining in detail the microfabrication process for integrated photonic devices in z-cut thin-film lithium niobate. Steps 1-5 relate to the fabrication of the device itself, 6-11 relate to periodic poling of lithium niobate and 12-14 refer to post-processing for edge-coupling.

7.2 Process overview

An outline of the full microfabrication process is shown in Figure 7.2. These are the steps that will be discussed in the remaining sections. The specific sequence of these steps is also a partial result of this project, and an optimal version could in principle require a different approach.

The samples used in this project consist of a 500μm-thick substrate layer of silicon, covered by a 2μm-thick layer of silicon dioxide (SiO_2), covered by a layer of z-cut lithium niobate ($LiNbO_3$) which will vary between 400nm and 500nm. We started from 4-inch wafers (purchased from external supplier), diced into 10x10 mm squares. Our microfabrication process consists in the following steps (with their corresponding diagrams in Figure 7.2):

- **(1-2) Sample preparation and coating:** the sample is cleaned and thoroughly dried to remove organic residues and humidity. An adhesion promoter and a thin layer of e-beam resist are spin-coated onto the sample.

- **(3) Electron Beam Lithography:** the sample is exposed to an electron beam which draws the desired pattern in the resist. For a negative tone resist (as shown in Figure 7.2), the exposed areas become resistant to the subsequent wet etching step with a developer solution.

- **(4-5) ICP-RIE Plasma Etching:** The patterned resist layer is used as a mask for dry etching of the $LiNbO_3$ substrate. A plasma of chemically inert Argon ions is created by an RIE power, which accelerates ions toward the sample. High-density plasma is achieved and maintained by a separately controlled adjustable RF antenna (ICP power). As a result, the sample is anisotropically etched in the vertical direction. After etching, the sample must be cleaned to remove redeposition.

- **(6-7) Aligned-exposure:** A new layer of positive tone photoresist is spin-coated into the sample, and a second round of aligned lithography is carried out on top of the previously etched devices, followed by a development step. This can be done with either optical or e-beam lithography, depending on the resolution requirements. Due to the use of positive-tone resist, the developed sample will have “holes” aligned with specific positions where electrodes must be defined.

- **(6-9) Aluminum deposition and lift-off:** An electron beam is targeted into an aluminum target to evaporate the metal, which is then directed onto the sample. As a result, a thin layer of aluminum is deposited on top of the sample, such that the lithographically defined "holes" are filled with metal. The resist layer is then removed with acetone in the lift-off step, "washing away" the portion of the aluminum layer in direct contact with the resist.

- **(10) Electric field-induced periodic poling:** A high-voltage is applied to the deposited aluminum electrodes to achieve electric-field-induced crystalline domain inversion of lithium niobate. Due to the periodic nature of the patterned electrodes, this process is referred to as "periodic poling".

- **(11-14) Post-processing:** The aluminum layer is then removed via wet-etching, and the sample is cleaned again. A protective layer of resist is spin-coated onto the sample, which is then cut with a diamond blade in a dicing saw to expose facets for fiber-to-chip coupling;

- **(Extra) Silicon dioxide cladding deposition:** Ideally, step 12 will be replaced by the deposition of a silicon dioxide layer via Plasma Enhanced Chemical Vapor Deposition (PECVD). In this case, for both protection and symmetrical optical isolation with respect to the original layer of SiO_2 underneath the $LiNbO_3$ layer.

All of these processes were carried out and tested for this project and will be discussed in greater detail in the following sections.

7.3 Electron beam lithography

The microfabrication process begins with Electron Beam Lithography (EBL). This is a standard technique for high-resolution patterning of resist masks and is widely used in integrated photonics [79].

EBL generally enables higher resolution compared with optical lithography, as the latter has its resolution limited by diffraction effects associated with larger wavelengths of optical photons compared to electrons. However, EBL is generally not used in large-scale foundry processes due to the very large exposure times associated with direct writing, and more bur-

densome operation requirements such as high vacuum. Thus, its use is generally restricted to research settings, and to the fabrication of masks for optical lithography.

The patterns written on the resist layer are transferred to the substrate in a subsequent etching step. Thus, the correct execution of the EBL step is crucial for device quality. Ideally, the patterned masks should enable good feature resolution, steep sidewall angles, and sub-nm roughness.

7.3.1 Goals and limitations

The acceleration voltage is a critical parameter in EBL. Electron beams accelerated by voltages in the 1-20 kV are generally used for scanning electron microscopy, where the information for imaging is obtained through secondary electrons, emitted by atoms excited by the original beam. On the other extreme, accelerating voltages above 100-300 kV are generally used for Transmission Electron Microscopy (TEM), where the acceleration must be high for the electron to be transmitted through the sample and detected at the other end to form an image. EBL lies in an intermediary range of 20-100kV, where electrons should ideally be accelerated with enough voltage to simply pass through the exposed resist layer, and then be conducted towards a ground away from the exposed regions.

The best EBL tools, operating at 100 kV voltages with well-calibrated processes and high-quality resists can reach feature resolutions around 10 nm. The EBL tool employed in this project (listed in Table 5.4), is limited to 30kV accelerating voltage. Furthermore, the maN-2400 series resist used is itself limited to a resolution around 30 nm. Several other factors must be optimized in order to reach the maximum resolution and quality: the exposure doses, sample preparation, proximity effects, spin-coating of the resist, pattering parameters (writefield size and alignment, speed, step size, direction and path), electron beam column parameters (aperture size and alignment, focus and astigmatism), and resist development.

While most applications, even for TFLN QPICs, do not require such extreme feature resolution, scattering losses can be greatly reduced by improvements in sidewall roughness, and dispersion effects are highly sensitive to sidewall angles. Thus, it is desirable to optimize EBL across all of these parameters. The final process described in this section reliably defined features down to 100 nm, yielding sidewall angles around 10° at 500 nm resist thickness. EBL-

related sidewall roughness can not easily be separated from roughness created by etching[1], but SEM images indicate sub-nm roughness in this process.

7.3.2 Substrate preparation and spin coating

EBL begins with the preparation of the substrate and coating of the resist. It was found that poor preparation of the resist may lead to poor adhesion of the resist layer and the collapse of the fabricated device, as shown in Figure 7.3. Similarly, improper coating can lead to inhomogeneity in resist thickness, which heavily impacts the quality of the mask.

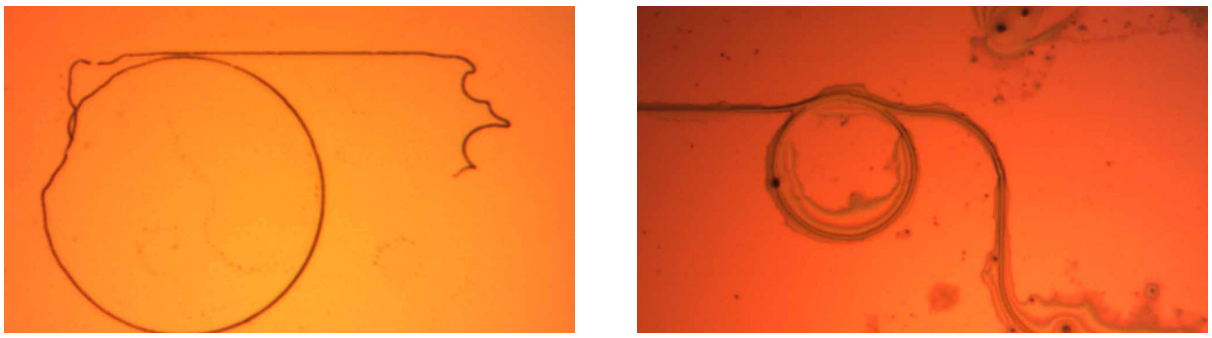

Figure 7.3: Two common failures in Electron Beam Lithography. On the left, a collapsed resist pattern due to poor adhesion, related to incorrect substrate preparation. On the right, an extreme case of poor development.

Before coating, the samples must undergo a standard organic cleaning. We found through trial and error that the samples should be coarsely cleaned with an electronics-grade cotton swab, immersed in boiling acetone (>60°C) for 5 minutes, and then sonicated. They must be immersed in IPA (propan-2-ol) immediately after, rinsed with DI water and dried with N_2 gun. Alternatively, the sample can be cleaned with a standard Piranha process, where the sample is immersed in a 3:1 mixture of sulfuric acid (H_2SO_4) and hydrogen peroxide (H_2O_2) at 100°C for 10 minutes.

After the sample is prepared, the SurPass 4000 ©adhesion promoter can be applied as recommended by the manufacturer. We also conducted tests with HMDS adhesion promoter, yielding similar results. In any case, before the resist is applied, the samples must be dried at 200°C for 10 minutes. Residual humidity in the sample is a major issue for resist coating, and can generally be detected in the sample through the presence of small, dark resist clots.

[1]In theory, it would be possible to use an appropriate Atomic Force Microscopy tool to measure the sidewall roughness directly in the resist layer after development.

After preparation, the samples were spin-coated with maN-2405 negative-tone resist, which is an easy-to-process, relatively inexpensive resist, with good resolution and etch resistance. In our 10x10 mm samples, the resist can not easily be made thicker than 500 nm without losing significant homogeneity, as shown in Figure 7.4. Therefore, we spin-coat the samples at 3000 rpm for 30 seconds, pipetting at least 10 droplets per coating with the sample already spinning at full speed.

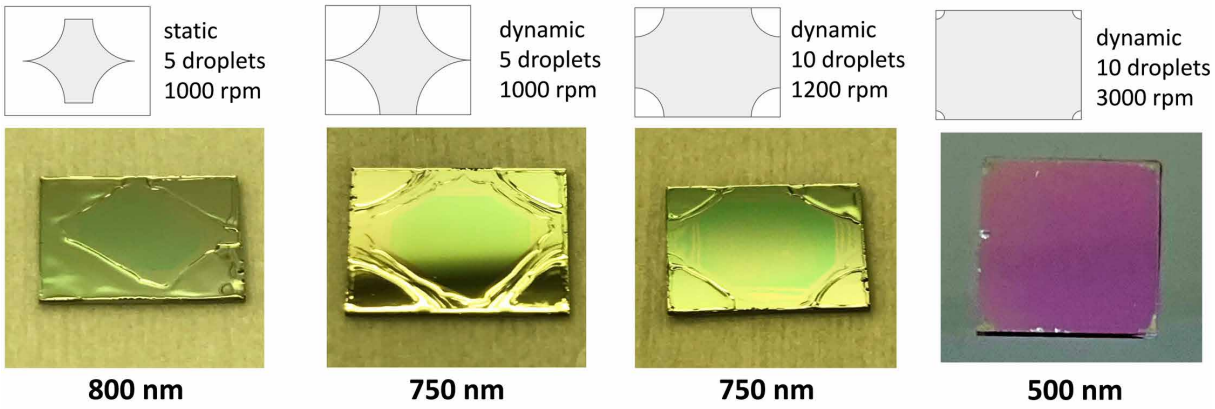

Figure 7.4: Resist coating results for different coating methods. Static and dynamic coating refer to the application of the resist before or after spinning has begun. Edge effects harm the homogeneity of the resist layer. Lower spinning speeds increase resist thickness, which reduces the demand for selectivity in etching but creates more uneven layers.

7.3.3 Dose test and proximity corrections

Next, we conducted extensive dose tests to find the best amount of charge per unit area to be set on the EBL tool. It is crucial to realize that different doses are required for features with different dimensions and surroundings. We converged on 100μC/cm^2 for 20 kV and 170μC/cm^2 for 30kV, applicable for waveguides (curved or not) in the range of around 1μm in width. These values work best while using an aperture size of 10μm and the minimum step size of 7.8 nm for a 500μm square write-field side (limited by maximum EBL frequency).

Dose test images are shown in Figure 7.5 and 7.6. While the first provides a first, coarse, approximation of the best dose using large features, the second test (combined with high-resolution imaging) was needed to adjust the dose for our specific purposes.

Proximity effects are a crucial obstacle to high-feature resolution in EBL. While an ideal EBL tool would expose only one point in the intended pattern at each step, the real tool will spread around each assigned point in an approximately Gaussian shape, as shown in Figure

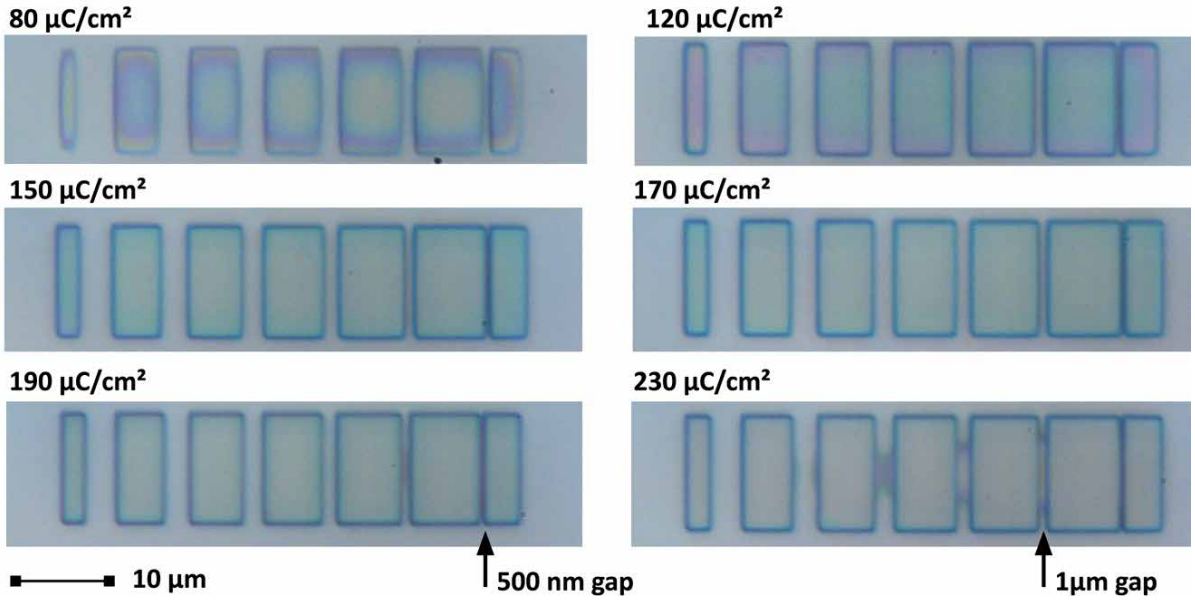

Figure 7.5: Optical microscope images of dose test for a square pattern in 500nm thick maN-2405 resist layer. The full test was conducted between 80 and 230 μC/cm^2 in steps of 10μC/cm^2. The lowest and highest doses are shown, as well as some intermediate steps around the best results.

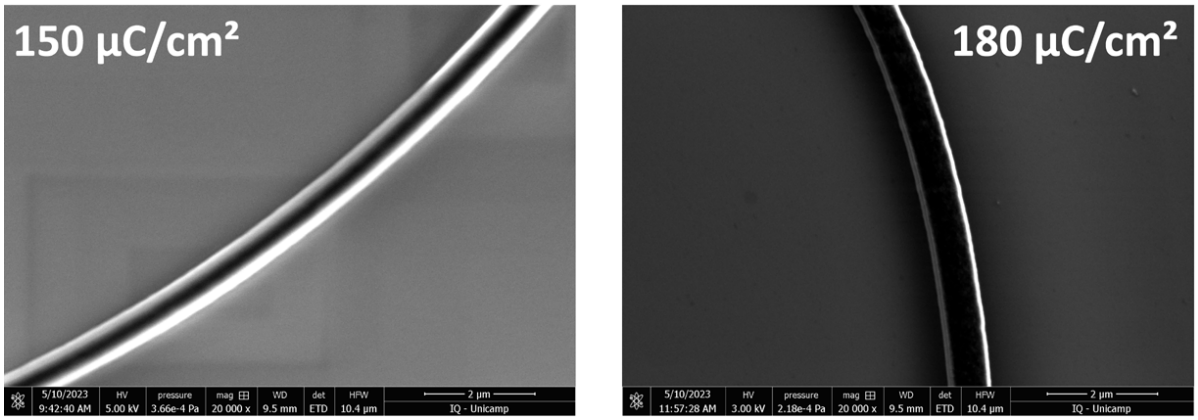

Figure 7.6: Scanning Electron Microscope (SEM) images of 1μm-wide resist masks for ring resonators in the same trial. 150μ/cm^2 dose leads to a triangular profile, while 180μ/cm^2 yields 10° sidewall angle. Optimization for smaller features requires more precise testing and finer parameter variation.

7.7. The dielectric nature of $LiNbO_3$ exacerbates this problem, as charge mobility is reduced, favoring the concentration of undesired charges in the substrate between exposure steps. Anti-charging agents are often employed in the literature to deal with this problem [74], but so far they have not been necessary to achieve our goals.

Proximity Effect Corrections (PECs) are a common way to address this issue. While we had access to the software dedicated to automated PECs, we found them to be counterproductive,

as they introduced new unexpected issues. In our final process, we implement only manual PECs based on dose adjustments found through trial and error for specific geometries. The 100 nm feature resolution range, which is sufficient for the applications in this project, can be achieved with no recourse to PECs of any kind.

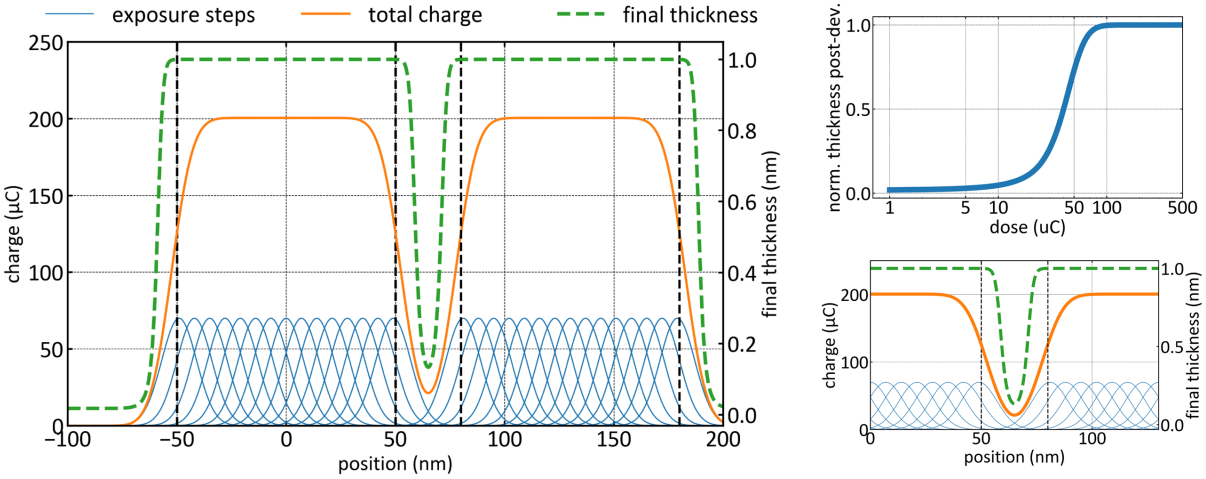

Figure 7.7: A numerical simulation of the charge distribution during Electron Beam Lithography of two 100 nm-wide structures separated by a 30 nm gap. Black vertical lines indicate the intended boundaries of the lithographically defined structure. The blue plot on the top right gives an exaggerated contrast curve for the resist. The bottom left plot gives a zoomed-in view of the gap.

7.3.4 Development

The last crucial step in the optimization of EBL is development. Ideally, development should completely remove all parts of the resist that were not exposed to the electron beam (or vice-versa for a positive-tone resist). We experimented with developers MIF-300, maD-525 and MIF-726, all based on Tetramethylammonium hydroxide (TMAH) solutions, with added surfactants in the case of MIF-726. The optimal development times were found to be 90s (MIF-300), 120s (maD-525) and 60s (MIF-726). In all cases, room temperature and vigorous manual agitation followed by 5-minute-long DI water rinsing yielded the best results.

By very far, MIF-726 exhibited the best performance, being the only one capable of realizing features smaller than 300 nm in the conditions mentioned above. This is most likely due to the reduced surface tension, which facilitates penetration into small gaps. MIF-726 agent greatly improved the overall homogeneity and reproducibility of the development process for all feature sizes.

Step	Details
Sample Preparation	Organic cleaning (acetone + IPA + DI water) Surpass 4000 spin-coating Drying at 200°C for 10 minutes
maN-2405 spin-coating	Spin-coating 30s @3000 rpm (for 500 nm thickness) Softbake 90s @90°C
EBL	30kV, 170μC/cm^2, 10μm aperture, 7.8 nm step size
Developer	MIF 726 1 min (manual agitation) Stopper DI water rinse >5 min

Table 7.2: Final EBL recipe for maN-2405 over thin-film lithium niobate. This recipe reliably yields at least 100 nm feature resolution.

The final results of the EBL process are shown in Figures 7.8 and 7.9, where waveguides and ring resonators are patterned with the desired characteristics, for multiple different geometries. Our device designs require upwards of 300 nm gaps between ring resonators and waveguides, which are reliably defined here. And SEM images (Figure 7.6) show steep sidewalls (<10°) and reasonably low roughness.

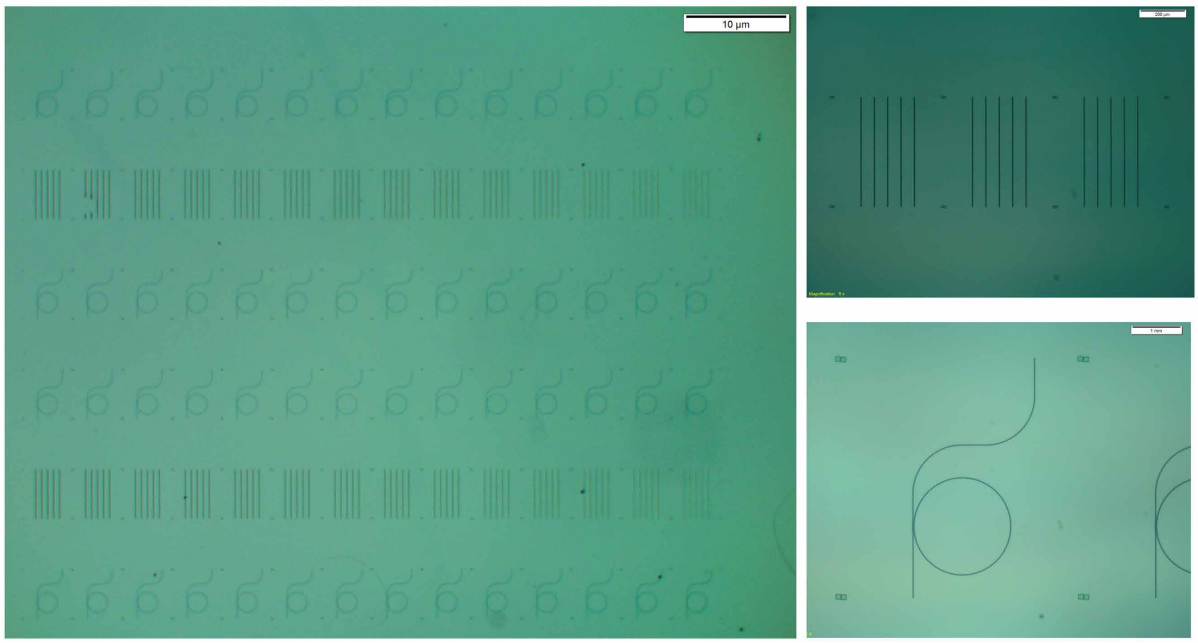

Figure 7.8: Post-development optical microscope images of the final results of EBL. The layout includes waveguides and ring resonators with different geometric features of interest for optical measurement (gap sizes, coupling lengths, widths, etc.). Devices are aligned in anticipation of dicing saw cuts.

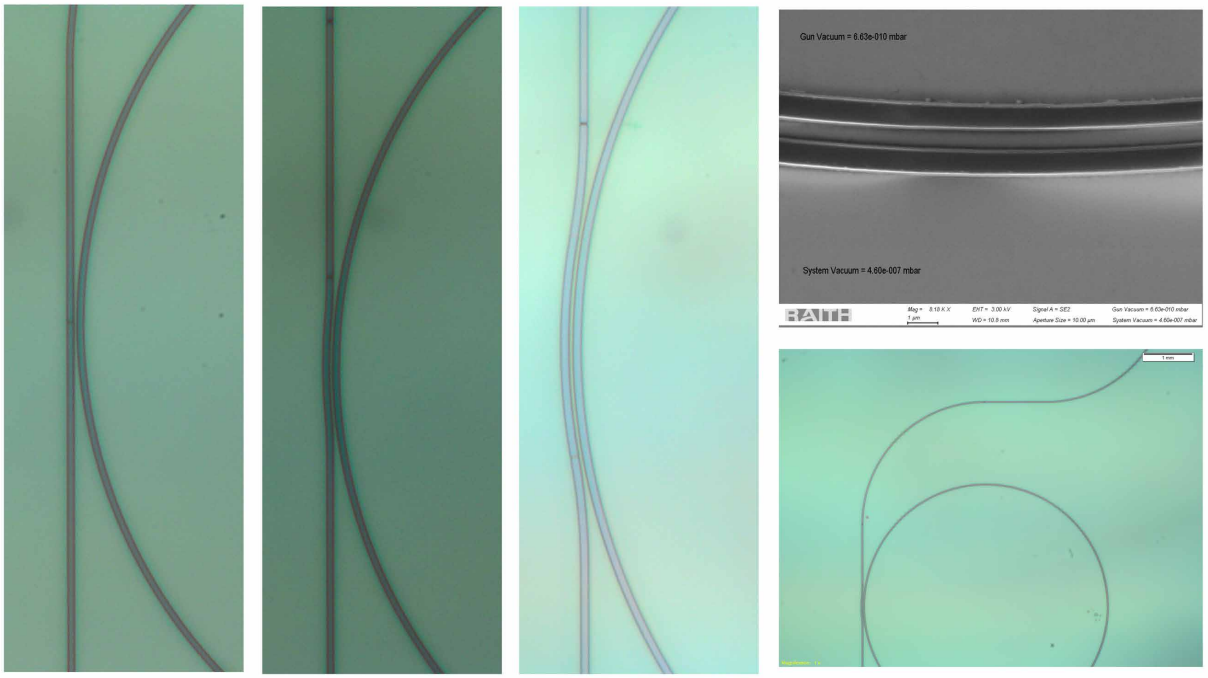

Figure 7.9: Post-development optical microscope images of the final results of EBL (only resist masks are shown, all structures are 1μm wide). 300 nm gaps are shown for different coupling lengths and a scanning electron microscope image of the coupling region. Although features down to 100 nm were successfully realized, they are not desirable for device design.

7.3.5 Writing on positive tone resists

The deposition of metals in specific spatial arrangements is an essential tool for microfabrication in integrated photonics. These electrodes are often used for "ad hoc" fine-tuning of optical devices via the thermo-optic effect. Furthermore, they are necessary for the realization of on-chip electro-optic modulators, which have been a central application of lithium niobate devices in the telecommunications industry.

Metal deposition is also an essential technique for integrated nonlinear optics, as they enable the realization of on-chip electric-field induced poling for quasi-phase-matched processes (see Chapter 2). For this particular application, precise spatial ordering and feature resolution are crucial, since the periodicity of domain inversion must be finely tuned to the specific nonlinear interaction of interest.

The smallest feature that must be resolved for successful deposition is proportional to the phase mismatch of the nonlinear processes, as in $\Lambda = \pi/\Delta\beta$. For second-harmonic generation based on an interaction between fundamental TM modes, we have calculated this value to be in the range of 4μm (see Figure 6.1), and optimal dispersion engineering can likely be used to make this width even larger.

For this process, we experimented with EBL as well as direct-writing optical lithography using Microwriter ML3 Pro at CTI. For an array of 90 devices similar to the one in Figure 7.10, the writing time is reduced to about 10 minutes, compared to about 4 hours in EBL using an aperture of 60μm at 30kV. While this is a significant improvement in terms of time, EBL yielded significantly better results, as optical lithography often failed to realize the smallest features. Additionally, the high-resolution imaging available in EBL tools allow for far more precise alignment of the metal electrodes to a previously etched layer of devices.

The recipe used for lift-off is shown in Table 7.3. It was developed by the technical staff at CCSNano, and only slight dose adjustments were needed to achieve our goals. We experimented with the deposition of gold (Au) and aluminum (Al) using EBPVD. While both methods produced good results, as shown in Figure 7.10, we found that aluminum can be easily removed from lithium niobate by immersion in AZ400K (concentrated) developer for 5 minutes. Gold, on the other hand, requires a thin layer of titanium (Ti) for proper adhesion, which has to be removed using hydrofluoric acid, also an etchant of lithium niobate.

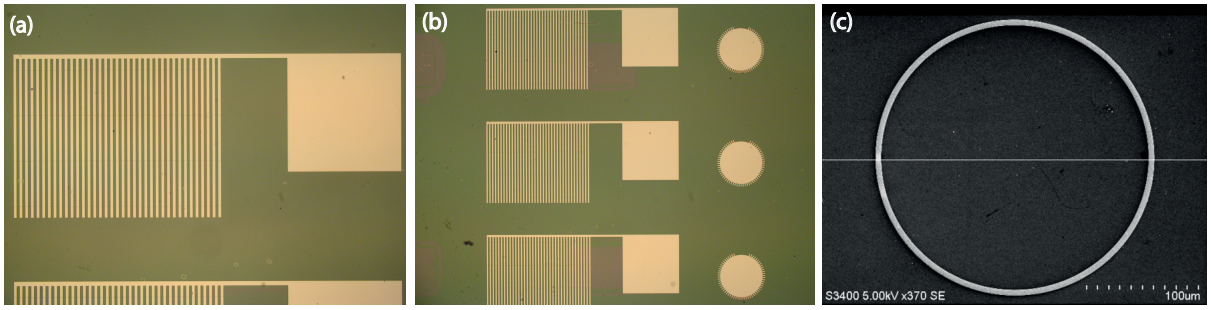

Figure 7.10: Metal electrode deposition via lift-off recipe with MMA/PMMA resist as shown in Table 7.3. (a) Aluminum electrodes for periodic poling of waveguides (the large rectangle is 250 μm wide). (b) Similar configurations for waveguides and gear-like configurations for ring resonators (200μm in diameter). (c) Gold deposition test.

The final process can reliably produce aluminum electrodes with spatial resolution above the requirements for most quasi-phase-matched processes. A much more fundamental limitation for the final resolution of periodic poling is dictated by the actual field-induced crystalline inversion process, as discussed in the subsequent sections.

Step	Details
MMA Coating (Ar-P 617.06)	Spin-coating 40s @4000 rpm (500 nm thickness) Softbake 5 min @180°C
PMMA Coating (Ar-P 679.04)	Spin-coating 40s @4000 rpm (300 nm thickness) Softbake 5 min @180°C
EBL	150μC/cm^2 @30 kV EHT
Developer	MIBK:IPA (1:3) 1 min Stopper IPA rinse >30s

Table 7.3: Recipes for EBL of positive-tone resists PMMA and MMA for lift-off. Credits for this recipe are due to the technical staff at CCSNano, up to a slight dose correction for $LiNbO_3$

7.3.6 Future improvements

As stated in Section 7.1, the time-scale and challenges of this project are not compatible with ultimate optimization. However, the achieved results leave us with clear indications of paths to improvement. The following changes should be tested to improve fabrication quality:

1. Implementation of multipass exposure. This technique has been reported to greatly improve line-edge roughness, thus significantly mitigating optical losses induced by scattering. [87].

2. Use of anti-charging agents such as Espacer©to mitigate even local proximity effects.

3. Use of smaller writefield to reduce minimum step size below 7.8 nm.

4. Perfect the implementation of automated PECs, aiming at improving roughness as well as feature resolution.

5. Experiment with different encoding for layout files besides GDS, as well as the number of points defining each polygon in the layout.

7.4 Etching of lithium niobate

In the etching step, the pattern defined lithographically using EBL is transferred to the lithium niobate substrate. The maximum achievable etching depths are determined by the selectivity of the resist mask, which was found to be highly sensitive to etching parameters. As a hard and relatively inert material, lithium niobate is notoriously difficult to etch [31], accordingly,

dry etching of lithium niobate was, by far, the most important hurdle faced during this project. In addition to achieving the necessary etching depth, an optimal etching process should yield steep sidewall angles and low sidewall roughness.

7.4.1 Goals and limitations

Dry chemical etching generally requires the use of fluorine-based compounds such as SF_6 and CHF_3. These compounds react with $LiNbO_3$ and lead to the redeposition of LiF, which acts as a soft "micro mask" during etching, leading to significant roughness and unwanted features [88, 89, 90, 31, 91]. When used for other applications, dry chemical etching with fluorine-based compounds is preceded by chemical treatment such as Proton Exchange. In this process, lithium ions are removed from the crystal through long-term, high-temperature immersion in proton-source acids. Additionally, the etching process is often intercalated with cleaning steps to remove the redeposited LiF redeposition.

Dry chemical etching is therefore not used in the literature for photonic-grade devices. Dry physical etching with Argon ions is the standard procedure for microfabrication of integrated photonic devices in TFLN [11, 92, 93]. Yet, etch rates of TFLN for argon are typically low (ranging from 4-40 nm/min) compared to most negative-tone high-resolution resists.

As a solution, successful low-loss photonic devices in TFLN invariably employ either ultra-high selectivity[2] Hydrogen Silsesquioxane (HSQ) resists, or silicon dioxide hard masks [94, 95, 74, 73]. In our case, neither of these options were available. HSQ resists were purchased but only arrived at the very end of this project, and the deposition of high-quality silicon dioxide relies on the availability of functioning PECVD tools. To the best of our knowledge, there are three of these PECVD systems in Brazil (including one at CCSNano), but none of them have been in operation up to May of 2023. Metallic hard masks are also not used for high-Q applications, as the inherent sidewall roughness of the mask is inevitably transferred to the device sidewalls [89].

However, as we show in this work, microfabrication of TFLN using only maN series (organic) resists is indeed feasible. We have found that there is a very narrow range of parameters at which very good etch rates and selectivity levels can be reached. In this case, the organic resist offers the advantage of being relatively inexpensive, having long shelf-life, being widely

[2]Selectivity here is defined as the ratio between the etch rates of thin-film lithium niobate and maN-2400 series resist. In this sense, higher selectivity is always desirable.

available, and being easy to store and process compared with the most commonly used alternatives. HSQ resists, for example, are notoriously hard to store and process [96]. These resists require doses on average ten times larger than maN-2400 series resists[97], dramatically increasing exposure times.

7.4.2 Overview of plasma-assisted dry etching

The working principle of Inductively Coupled Plasma Reactive Ion Etching is the vertical acceleration of ions in the direction of a target sample. In the case of Argon ions, the etching mechanism is exclusively physical, as the ions do not reach chemically with the sample. The parameters available in the main ICP-RIE tool used in this project are shown in Figure 7.11.

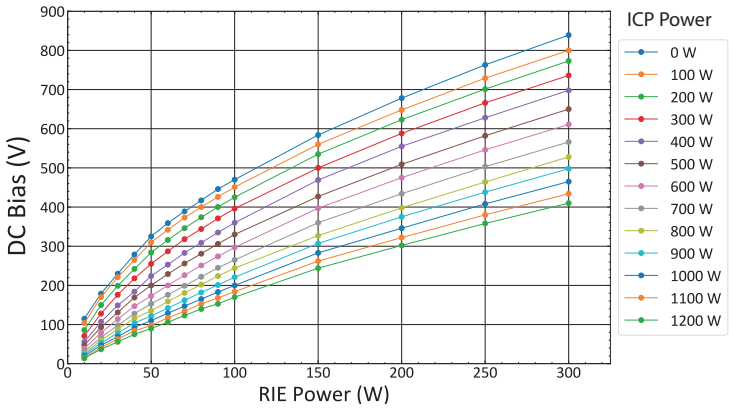

Parameter	Minimum	Maximum
RIE Power	10 W	250 W
ICP Power	10 W	1250 W
Mass Flow	5 sccm	50 sccm
Pressure	5 mTorr	100 mTorr
Temperature	25°C	60°C

Figure 7.11: Characterization of the DC bias of the Oxford Plasmalab tool at CCSNano (data acquired in collaboration with Frederico Hummel Cioldin). On the right, a table showing the range of parameters allowed by the equipment. Not all combinations are realizable.

The independent control of ICP and RIE power is a major feature of ICP-RIE tools. RIE power will control the strength of the field accelerating the ions anisotropically toward the sample. As shown in Figure 7.11, RIE power is strongly correlated with the resulting DC Bias voltage measured between the chamber and substrate. ICP power will control the strength of the RF field used to increase the plasma density. As shown in Figure 7.11, for a fixed RIE power, ICP power will generally result in a lower DC bias.

As shown in the next section, the ideal range of ICP/RIE power for high-selectivity etching of Lithium Niobate with maN-2400 series resist mask was found largely through trial and error. A balance between plasma density and ion accelerating energy must be found to favor the etching of lithium niobate compared to the resist. Other factors such as chamber cleaning

and condition and resist hardbake were also tested and optimized. These results are shown in detail in the subsequent section.

The effect of all parameters in the resulting etch rates and selectivity is extremely hard to predict. Looking exclusively at etch rates, we found that the lowest pressure yields the greatest etch rates for lithium niobate. This is likely related to the increase in the mean free path length of the ions as a function of the vacuum level. This increased etch rate was greater for Lithium Niobate compared to the maN-2400 series resist. Thus, in the final recipe, minimum achievable pressure is used.

Physical etching is much less sensitive to temperature compared with chemical etching [98]. Indeed, we found that temperature has negligible influence on the etch rate of lithium niobate, while our experiments with the chemical etching of silicon and silicon dioxide showed great sensitivity to temperature. On the other hand, we found that high temperature decreased the etch resistance of the resist, a result also reported in the literature [89]. Thus, our final recipe employs the lowest achievable temperature, which in our case is limited to room temperature.

7.4.3 Characterization of recipes

The most relevant recipes characterized during this project are shown in Table 7.4 in the chronological order in which they were tested. Changes in the parameters across iterations were generally motivated by analogous processes in the literature, physical intuition, or direct experimentation. There is a clear upwards trend in both selectivity and etch rate, culminating in the optimized recipe L. A more careful and detailed characterization of this optimized recipe is shown in Figure 7.12.

Table 7.4 does not exhaust the etching attempts conducted for this project. Due to several limitations, not all attempts could be fully characterized, and only qualitative assessments were made to inform the subsequent steps.

The search for high etch rates and selectivity is ubiquitous in microfabrication. The maximum achievable etching depth is limited by the selectivity of the resist and the thickness of the spin-coated layer, as in

$$\text{maximum etch depth} = \text{selectivity} \times \text{resist thickness}. \tag{7.1}$$

#	ICP (W)	RIE (W)	Bias (V)	Press. (mTorr)	Flow (sccm)	Prebake temp. (°C)	Etch rate (nm/min)	Sel.
A	1250	10	24	100	5	none	5.0	-
B	100	70	360	5	20	none	2.7	0.22
C	100	70	340	5	20	none	2	-
D	100	70	185	5	20	100 (5 min)	4.6	0.12
E	100	200	380	15	20	100 (10 min)	10	0.10
F	100	200	370	15	20	110 (10 min)	10	0.07
G	600	210	315	85	5	110 (10 min)	<1	0.00
H	150	50	172	15	50	110 (10 min)	12	0.16
I	100	70	190	10	20	135 (10 min)	7.5	0.25
J	100	80	340	10	50	140 (10 min)	7.0	0.40
K	800	105	240	9	50	none	35	0.63
L	800	105	240	9	50	135 (8 min)	35	0.85

Table 7.4: Most relevant characterized recipes for Inductively Coupled Plasma Reactive Ion Etching (ICP-RIE) of z-cut thin-film Lithium Niobate exclusively using Argon ions. Selectivity (Sel.) is defined as the ratio between the etch rates of Lithium Niobate and of maN-2405 resist. All processes were run with the minimum achievable temperature of 25°C, except for recipe A, run at 60°C. The recipes are presented here in the chronological order in which they were tested.

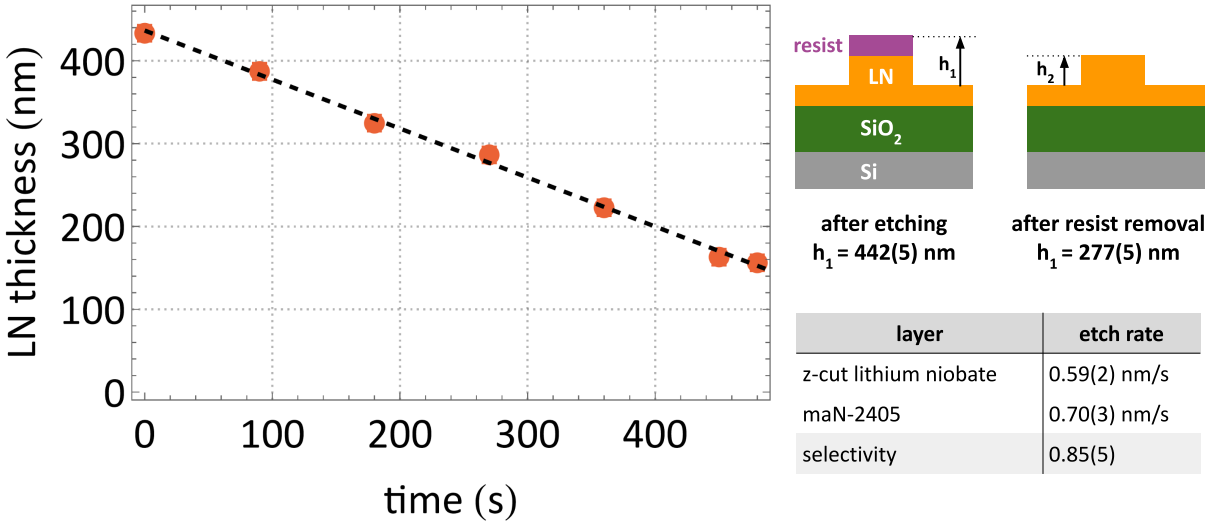

Figure 7.12: Detailed characterization of the best ICP-RIE process (recipe "L" in Table 7.4. Error bars (10 nm) in the plot are too small to see.

As we have shown in Figure 7.4, the latter can not be arbitrarily changed for a given resist, such that selectivity must be increased in order to fabricate deeper devices.

There are several important reasons why a wide range of achievable etch depths is desirable. First, etching depth is an important degree of freedom for photonic design and dispersion engineering. Second, deep-etched photonic devices offer higher mode confinement due to the increased refractive index contrast, enhancing nonlinear optical effects. Third, in a partially-etched device, the remaining "slab" will have its own set of modes interacting with the waveguide modes, leading to undesirable effects. Finally, we found that fiber-to-chip edge coupling of light is extremely challenging in shallow-etched devices, due to huge spatial mode mismatch between the optical fiber and the transverse section of the waveguide. Not coincidentally, our first successful coupling trials only occurred after substantial improvements to the etching depth.

Equation 7.1, however, is limited by one major caveat. If achieving the maximum etch depth requires long etching times, the resist is likely to incur significant damage, as demonstrated in Figure 7.13. Thus, an optimal etching recipe should exhibit both high etch rates and high selectivity. We found that this problem can be greatly mitigated by adding cooling steps (3 minutes) in between short etching iterations (90s). Nevertheless, the constraint still stands,

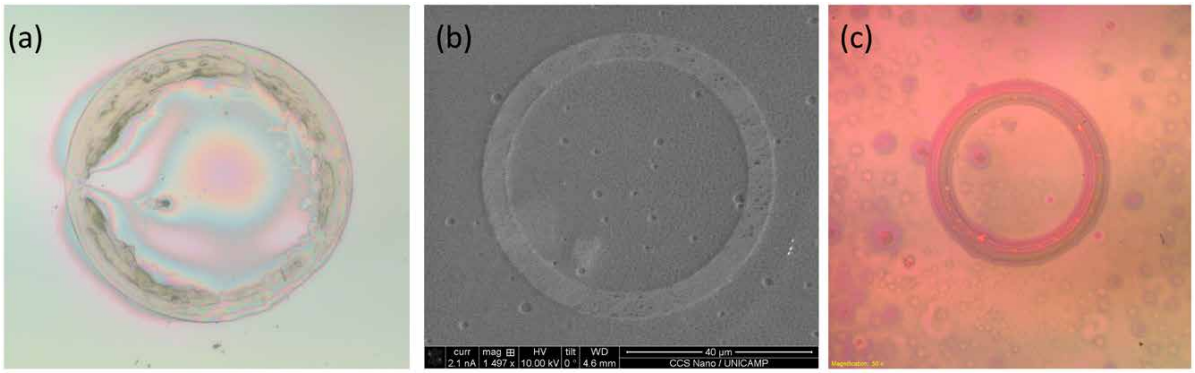

Figure 7.13: Failures of dry-etching demonstrate the need for strict optimization. (a) A resist mask for a 30μm (radius) disk that has been continuously etched in Argon for 40 minutes. The resist can not withstand long continuous etch times without significant damage. (b) A lithium niobate ring resonator etched for 40 minutes, in 5-minute intervals. The device becomes wider than intended and micro-masking effects are visible on the top. (c) A similar ring resonator after etching in a contaminated ICP-RIE chamber. Regular manual cleaning of the chamber is crucial.

Figure 7.13 also illustrates the importance of chamber cleaning. In our final process, as shown in Table 7.4, the conditioning and etching steps are preceded by a 20-minute long O_2 based cleaning. It is also crucial for the chamber to be periodically opened and manually

cleaned, especially for multiuser equipment where multiple different processes are carried out. In one case, we found that etch rates and device contamination dramatically improved after a round of manual cleaning.

In addition to the use of organic resist for the physical etching of TFLN, there are several other major reasons why the optimization of etching was a significant challenge for this project:

- Unlike EBL, etching is a destructive process, in the sense that samples can not be reused, making large-scale trials impractical for costly samples such as TFLN.
- To conduct a single etching trial, a round of EBL must be executed beforehand. EBL is a very time-consuming process, both due to the nature of the technique, and to scheduling limitations in multiuser facilities.
- Our main cleanroom facility (CCSNano) does not have the appropriate equipment for the characterization of etch rates. Namely, contact surface profilers and atomic force microscopes. Thus, each measurement required the samples to be moved to other facilities, which also had their own scheduling limitations. Removing samples from the cleanroom also leads to contamination and reduces reproducibility.
- The Oxford ICP-RIE Plasmalab 100 at CCSNano (Unicamp) was shut down for maintenance for several months, and the processes had to be conducted at the ICP-RIE OXford Plasma Pro NGP80 at LNNano (CNPEM). We found that the processes are generally not reproducible between the two machines, such that our processes had to be recalibrated multiple times.

Post-etching SEM images of our first optically measured photonic integrated devices in TFLN are shown in Figure 7.14. In this case, sidewall roughness is well above the desired levels (ideally, roughness should be unnoticeable at this range of magnification). It is crucial to realize that this is not an inherent limitation of maN-2400 series resist, as indicated by an extremely recent external pre-print result [94], achieving $4.8{\times}10^6$ intrinsic Q-factor resonators with maN-2400 series resist.

Thus, the high level of roughness is likely due to a sub-optimal EBL process conducted during etching and coupling trials in the interest of time efficiency. Although this result is already satisfactory, fulfills the goals of this research project, and enables important exper-

imental achievements, future fabrication rounds should already yield significantly superior results.

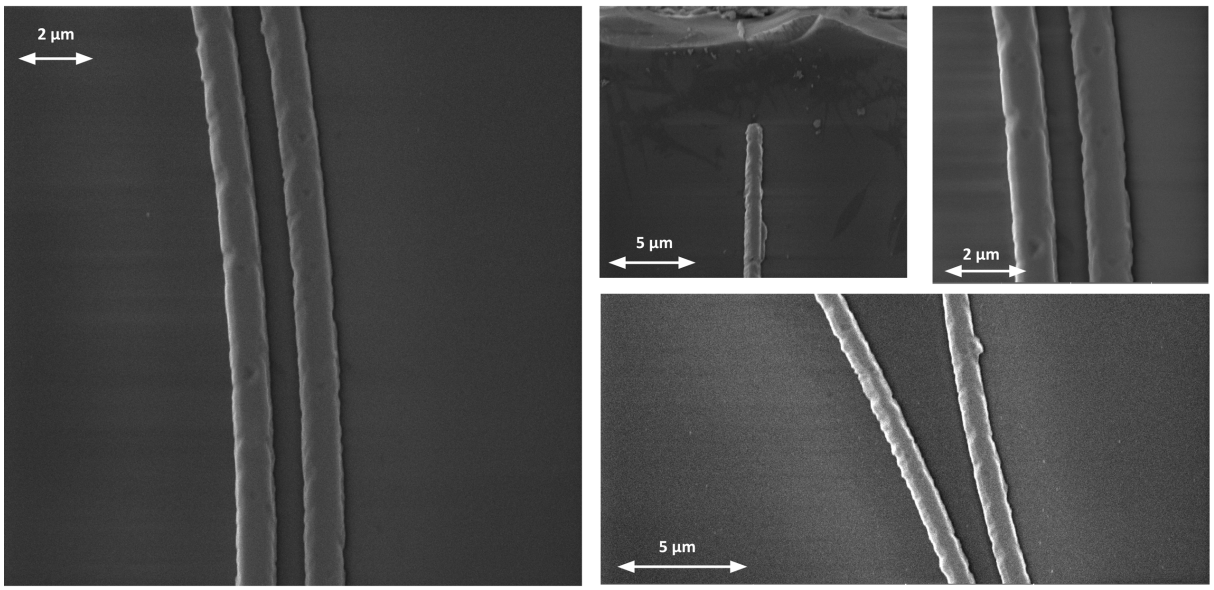

Figure 7.14: Scanning Electron Microscope(SEM) images of the first measured lithium niobate photonic device, also shown in Figure 8.2. In the interests of time efficiency, this device was etched following a sub-optimal EBL process, which has already been improved, as shown in the previous section. The improved process is expected to yield much better roughness results, pending implementation.

7.4.4 Redeposition and cleaning

We found that physical etching leads to the redeposition of a thin layer of lithium niobate (confirmed via Energy Dispersive X-Ray Spectroscopy) around the device sidewalls, which can lead to substantial scattering losses. This can be most easily seen as the "snow-like" dust in Figure 7.15(c). This phenomenon has been reported in the literature [92], and the redeposition can be removed using a 2:2:1 mixture of hydrogen peroxide (H_2O_2), ammonium hydroxide (NH_4OH) and DI water.

It is important to note that this mixture is an etchant of lithium niobate. In fact, it was recently demonstrated that this mixture can be used as a wet-etching alternative for high-Q TFLN devices, using silicon dioxide as a high-selectivity mask [99]. We independently verified this result, estimating an etch rate of 1 nm/min in z-cut TFLN, compared to 4 nm/min in [99]. In future processes, enabled by the deposition of silicon dioxide, this constitutes an important alternative for high-quality and easy fabrication.

Full $LiNbO_3$ Etching Recipe	
First round of cleaning	O_2 (50 sccm) and CF_4 (5 sccm) 1200 W ICP, 120 W RIE 15 mTorr average DC bias 292V 20 minutes
Conditioning	Ar (50 sccm) 800 W ICP, 105 W RIE 9 mTorr average DC bias 240V 10 minutes
Etching	Same parameters Etch in steps of 90s, with 3 min cooling time between steps LN etch rate of 0.59(2) nm/s Selectivity 0.85(5) with respect to maN-2405

Table 7.5: Summary of the complete etching recipe summarized in Figure 7.12, including cleaning and conditioning steps

Figure 7.15 shows a demonstration of redeposition cleaning using the H_2O_2/NH_4OH/water solution at 100°C. Note that the third round, corresponding to a total cleaning/etching time of 120 minutes [3], clearly shows the undesired effect of etching. Here, the redeposited layer acts as a soft mask for the etching solution, adding significant roughness to the device sidewalls. The cleaning procedure should therefore be limited to about 60 minutes, and checked in an SEM.

7.4.5 Etched facets

Additional etching tests were also carried out for deep-etching of silicon dioxide and silicon. Here, the goal is to add an alternative to the post-processing steps 12 and 13 in Figure 7.2. In this case, the dicing of the sample would be replaced by direct dry etching of the facets, eliminating the need for dicing saw cuts and potentially yielding higher-quality facets.

A recipe for silicon dioxide etching was characterized and optimized, as shown in Figure 7.6. Here, the main challenge is to have the resist withstand the 20 minutes of etching time required to etch 2μm of silicon dioxide, plus any remaining lithium niobate from the first

[3] The solution must be replaced and restarted periodically (20 minutes) due to evaporation of the solvents.

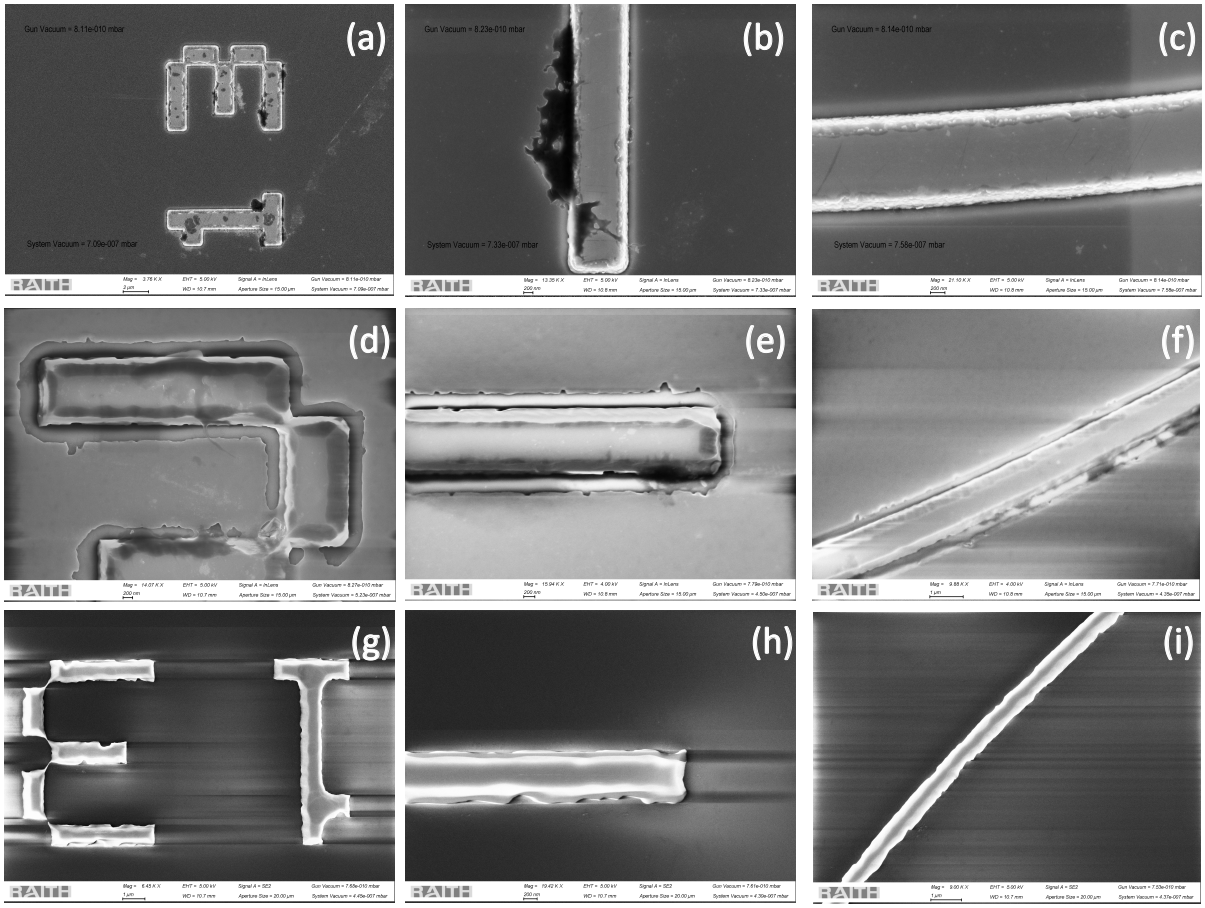

Figure 7.15: Post-etching cleaning of redeposition in TFLN waveguides using 2:2:1 mixture of ammonium hydroxide, hydrogen peroxide and DI water at 100°C. The results shown are SEM images after (a)-(C) 0 min; (d)-(f) 60 min; (g)-(i) 120 min. The last case shows a clear "overcleaning" of the redeposited material, and extreme roughness induced by the softmask effect of the redeposited material under the etchant mixture.

etching step. We found that AZ3312 fulfills this requirement once the chamber is properly cleaned (with a standard O_2 cleaning and periodic manual cleaning) and cooling steps are added after every five minutes of etching.

While this process can, in principle, make high-quality facets for fiber-to-chip coupling, this has not yet been realized experimentally, as good results were obtained using dicing saw cuts. Once the silicon dioxide layer is removed, the silicon layer is exposed and can be manually cleaved with good precision.

7.5 Periodic poling of Thin-Film Lithium Niobate

Periodic poling has become a well-established and widely implemented technique to achieve quasi-matching in thin-film lithium niobate PICs. [100, 31].

SiO_2 Etching Recipe	
Composition and flow	O_2 (3 sccm) and CHF_3 (52 sccm)
ICP/RIE power	1200 W / 45 W
Average DC bias	53 V
Temperature/Pressure	25°C / 10 mTorr
Average etch rate	100 nm/min (~1.62 selectivity relative to AZ3312)

Table 7.6: ICP-RIE etching recipe for silicon dioxide.

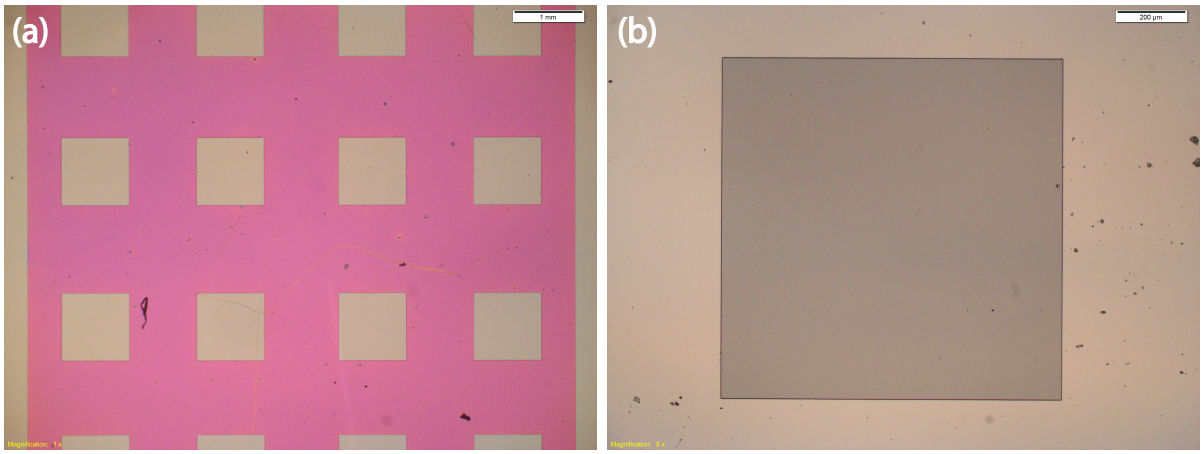

Figure 7.16: Deep consecutive etching of lithium niobate and silicon dioxide with photoresist mask using 2μm-thick AZ3312 resist. Each of the squares in the image is 500μm in side. (a) After 15 minutes of etching, (b) after 20 minutes of etching. The image shows a very good tolerance of the resist to long etching, making the process suitable for the fabrication of optical-grade facets. Images acquired by group member Dr. Melissa Mederos Vidal.

In the electric-field-induced periodic poling of lithium niobate, a high coercive field of around 20kV/mm (corresponding to a high-voltage pulse of around 600 V for our z-cut samples) is applied to invert the orientation of ferroelectric domains in the crystal. In order to ensure quasi-phase matching, the inversion must occur in a spatially periodic fashion along the propagation direction. This process is facilitated by raising the sample to high temperatures (in our case, we found that 250°C was sufficient for the parameters mentioned).

As shown in Figure 6.1, this inversion must have a period equal to $2\pi/2\Delta\beta$, where $\Delta\beta$ is the phase mismatch between the interacting waves. Each electrode must therefore have a width of $\pi/2\Delta\beta$, with an equally sized interval separating it from the adjacent electrode. The microfabrication step was successfully implemented and shown in Figure 7.10. In this section, we will discuss the field-induced crystalline inversion process. Periodic poling in TFLN was achieved in close collaboration with Ph.D. candidate Rafael Carbat Miranda.

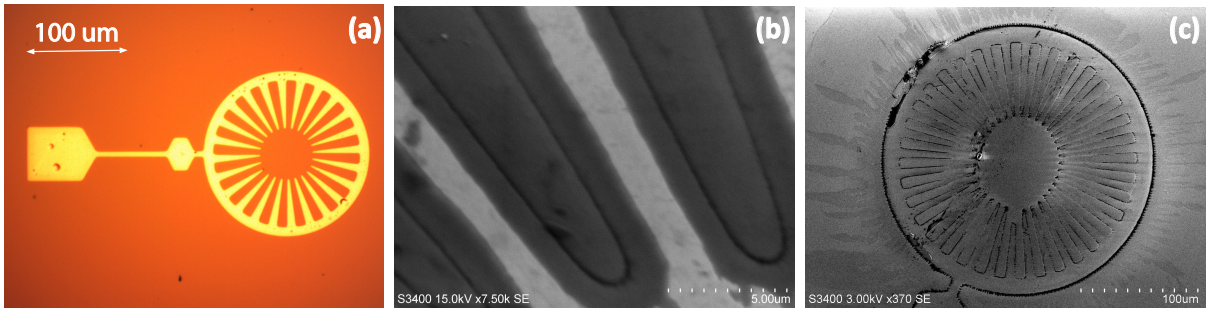

Figure 7.17: First round of results in Periodic Poling of TFLN.(a) An example of a gold electrode pattern used for poling trials (in this case, third-party fabricated), (b)-(c) SEM images of the poled region after electrode removal and HF acid etching, the apparent contrast defines regions with a height difference around 100 nm.

A setup (partially shown in Figure 7.18) was constructed to generate pulses with adjustable duration and shape, including a custom-made high-voltage amplifier circuit and a precision contact probe. The high-voltage is supplied by an arrangement of eight 8 DC power sources in series, each supplying up to 120 volts. A maximum temperature of 250°C is maintained by a hotplate and monitored with a thermocouple. Pulse shape parameters were extensively tested to identify a procedure capable of yielding the necessary spatial control of the inverted domains.

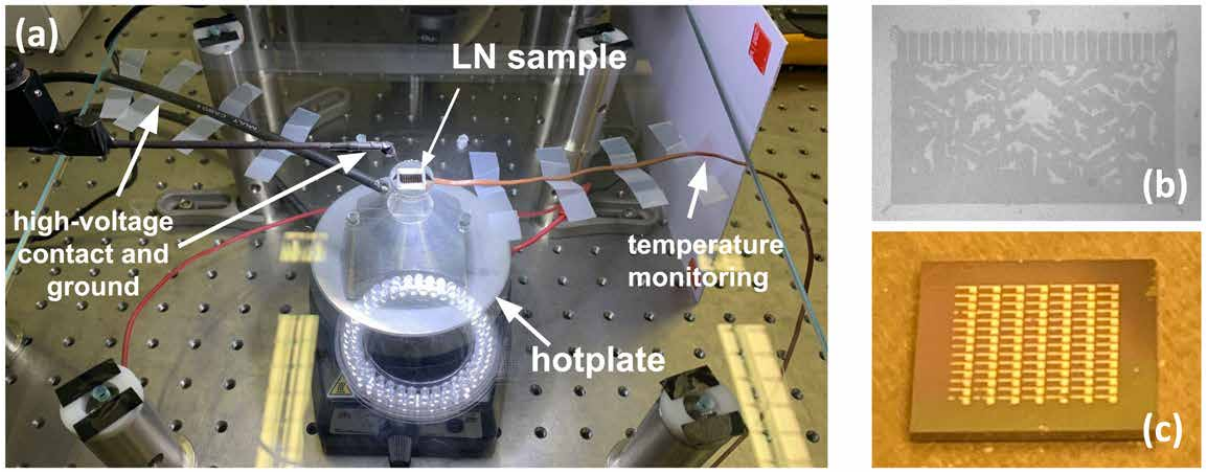

Figure 7.18: (a) Setup for implementation of field-induced periodic poling using high-voltage pulses at elevated temperatures; (b) optical microscope image of a TFLN sample after periodic poling followed by hydrofluoric acid etching, demonstrating good spatial control of the poled regions; (c) picture of a sample after gold electrode deposition using EBL and lift-off.

The results of the first round of periodic poling trials is seen in Figure 7.17. Here, Hydrofluoric Acid (HF) etching is used as a technique to verify the realization of domain inversion. The etch rate of lithium niobate with respect to HF is highly anisotropic, such that etch rates in the

z-direction are much larger than the original z+ orientation (which is exposed in the original, "unpoled" sample). Thus, if a sample is immersed in HF after periodic poling, the inverted regions will be etched much faster.

The specific value of the z+ and z- etch rates in HF is not clear or consistent in the literature, as some details about the precise composition of the acid solution and the TFLN sample are often omitted [101]. Furthermore, periodic poling is more often verified via direct measurement of nonlinear optical phenomena, which had not yet been achieved during this stage of the project.

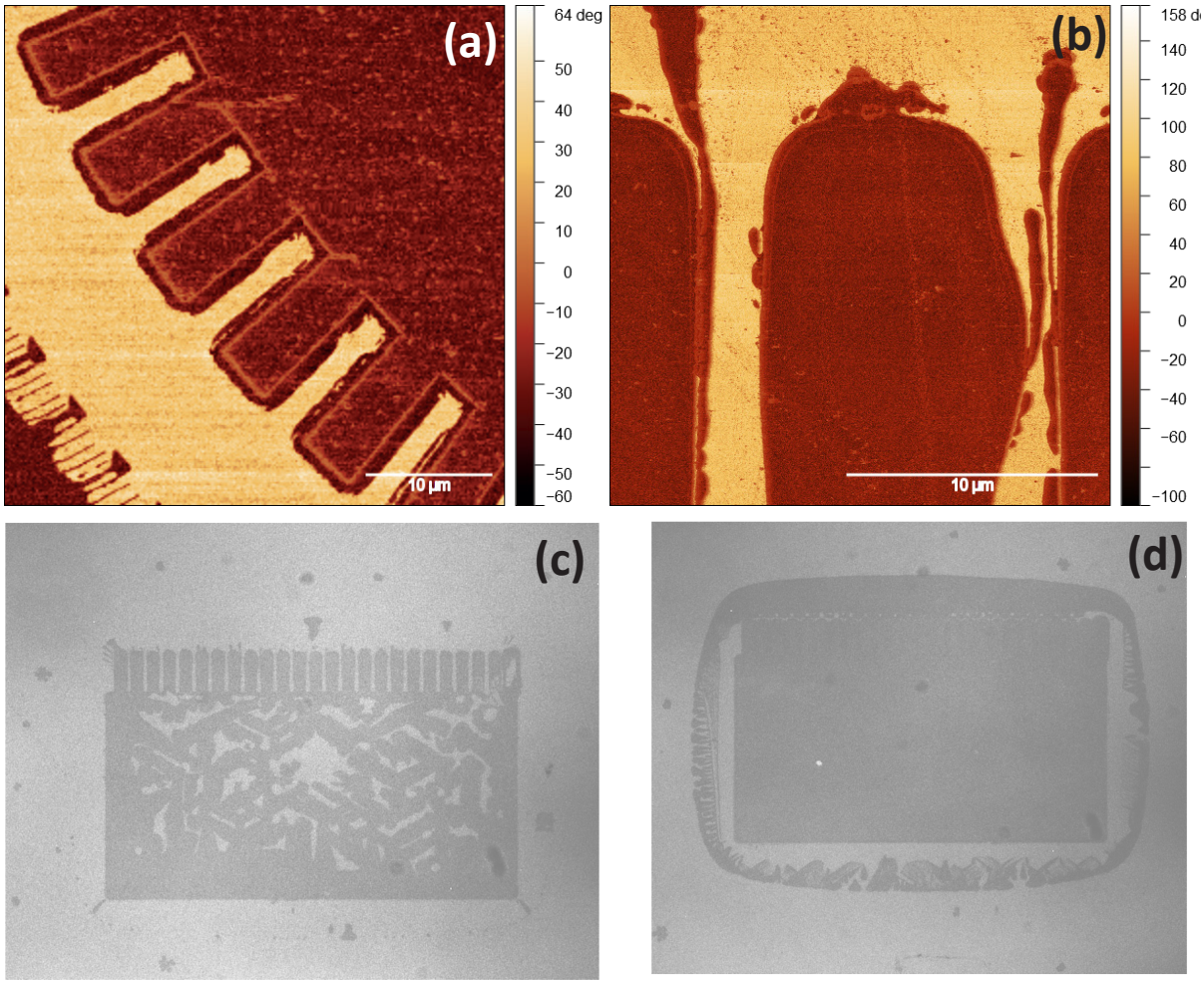

Figure 7.19: (a)-(b) Phase-information of piezoresponse atomic force microscopy over periodically poled regions in TFLN, demonstrating spatial resolution of a few microns (Images acquired by group member Rafael Miranda). In an optical microscope, this corresponds to a completely plain image, with no visible topographic features. (c) Optical microscope image of a periodically poled region after HF etching using the optimal poling recipe. (d) A similar structure, with a pulse amplitude above the optimal value.

An often-cited reference in HF etching of LN [102] reports an etch rate ratio of 1:20 between z+ and z-, thus predicting around 483 nm/min for z- and 17 nm/min for z+. However, this is based on an "ad hoc" correction, not a direct measurement. We have found that the etch ratios for z+ and z- in our samples are around 17 nm/min and 43 nm/min, respectively.

While this may have initially suggested a failure to achieve domain inversion, the experiment was validated using Piezoresponse Atomic Force Microscopy (PAFM) in our poled samples. This is also a method commonly used in the literature to verify the periodic poling of ferroelectric materials[103].

Within the explored range, we found that the best results (in terms of spatial resolution) were obtained by applying 6 voltage pulses with an amplitude of 550V and duration of 160ms, with a 10ms rise time, and separated by 2000ms each. The PAFM results for the Periodically Poled Lithium Niobate (PPLN) samples yielded by our final process are shown in Figure 7.19, demonstrating an achieved spatial resolution in the order of a few microns, which fulfills our benchmark for all intended applications.

Chapter 8

Coupling Light into Photonic Chips

The linking of integrated photonic circuits to off-chip systems is an essential requirement for the practical use of PICs. Integrated light sources and photodetectors are often unsuitable or impractical for specific materials and applications, such that external lasers and detection or transmission schemes must be used. External coupling systems often impose major limitations on the environmental stability and performance of photonic integrated circuits and are therefore a major point of interest for current research [104, 105, 106]. In this chapter, we discuss a series of post-processing steps conducted to prepare our fabricated samples for fiber-to-chip coupling of light.

8.1 Fiber-to-chip edge coupling of light

The fundamental challenge of coupling light from external sources into photonic chips is shown in Figure 8.1, which represents an "edge coupling" scheme (also called "butt-coupling"). The optical fibers used to transmit light from sources or toward detectors have mode-field diameters in the order of approximately 10μm, while integrated waveguides have cross sections in the range of 500nm to a few microns. The coupling efficiency is therefore limited by the spatial mode mismatch between waveguide and optical fiber.

A simple model for the coupling efficiency can be derived by applying a continuity condition for the transverse electric and magnetic fields at an interface. If the two fields are approximated by Gaussian profiles with beam radii given by w_i, and effective indices given by n^i_{eff},

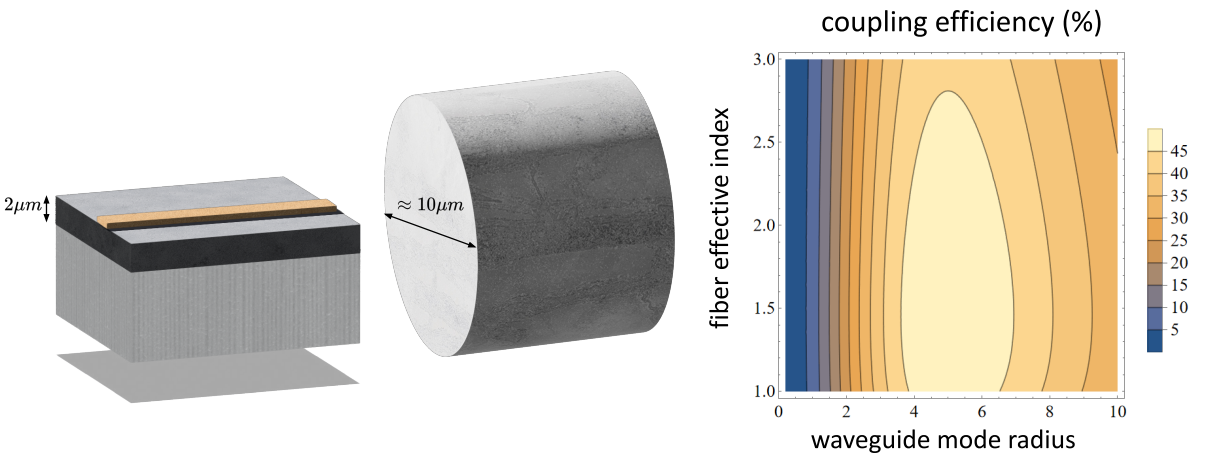

Figure 8.1: A representation of the fundamental challenge of fiber-to-chip coupling. SiO_2 slab thickness is not to scale. On the right, an approximate calculation of coupling efficiency based on Equation 8.1.

the coupling efficiency (in terms of transmitted power) will be [22]

$$\eta = \frac{2n^i_{eff}n^t_{eff}}{(n^i_{eff}+n^t_{eff})^2}\left(4\frac{w_1^2w_2^2}{(w_1^2+w_2^2)^2}\right). \tag{8.1}$$

A plot of equation 8.1 is shown in Figure 8.1. For example, we can calculate that a waveguide with w_1=500 nm and n^1_{eff}=2.3, and an optical fiber with w_2=5μm and n^2_{eff}=1.46 will have a maximum coupling efficiency of 1.8% (~17 db loss at the interface). Notice that propagation losses in TFLN devices can be as low as 0.002 dB/cm [74], such that total losses are often dominated by those related to the insertion process. Crucially, several techniques have been implemented to increase the efficiency of edge coupling.

In inversely tapered waveguides, the cross-section width is slowly reduced as the waveguide approaches the coupling edge. The inverse taper usually extends along several tens of micrometers, as the width is reduced to a few hundred nanometers. As the width is reduced, the mode-field diameter of the waveguide will increase, and the mode will become less confined in the waveguide core, improving the modal overlap between waveguide and fiber modes. This technique has been employed at least since 2003 for silicon-on-insulator devices, yielding losses as low as 3dB/facet [107].

Similar results have been demonstrated for TFLN, with 200 nm-inverse tapers resulting in losses as low as 6 dB/facet at 1550 nm [104, 108]. More complex schemes combining inverse tapers with ultra-high numerical aperture fibers [109] and passive mode size converters based on tapered LN bilayers [110] have achieved coupling losses below 2dB/facet for TFLN. In the

absence of such specific design, typical values reported in the literature still range between 8 and 11dB/facet [111]. For competing photonic materials like aluminum nitride (AlN), silicon nitride (Si_3N_4), silicon-on-insulator (SOI), and aluminum gallium arsenide on insulator (AlGaAsOI), the typical edge coupling insertion losses are also on the range of 2-3dB/facet [112, 113].

8.2 Facet preparation

For this project, we optimized a series of post-processing steps to enable efficient edge coupling, as shown in Figure 7.2. In order to expose the waveguide facets, we investigated four main methods: (1) cleaving of the sample with a diamond-tip scriber; (2) Cutting with a diamond-blade dicing saw; (3) Deep dry etching with ICP-RIE equipment preceded by aligned photolithography; (4) Mechanical polishing using micrometer-roughness sandpaper, generally used for polishing of optical fibers.

We found that cleaving the samples often leads to undesired cracking of the lithium niobate layer, for which the cleaving direction often does not follow a straight line. Thus, the process has very low reproducibility and a high risk of compromising samples. This problem could be mitigated by fabricating very long coupling waveguides, such that the design would be tolerant to uneven cleaving. However, this solution requires very precise alignment of neighboring write-fields during EBL, and is likely to introduce major losses.

The development of a process for the fabrication of etched facets was discussed in Section 7.4.5. A process capable of fully etching the 2 μm-thick silicon dioxide layer was developed, using optical lithography and dry etching. Processes of this kind are well known to produce high-quality facets with very low roughness, greatly limiting losses induced by scattering [114]. To enable edge coupling, it is still necessary to remove the silicon layer underneath, making room for the optical fiber, either by manual cleaving or further etching. Therefore, the full development of a coupling method via etched facets was not completed for this project, as it imposes additional fabrication steps compared to dicing-saw cutting. As multiple methods were developed in parallel for this project, the latter was chosen as a priority for its simplicity and effectiveness.

We found that efficient edge coupling could be achieved by exposing the waveguide facets using diamond-blade dicing saw cuts. We found that cutting through the waveguides leads

to major shattering of the facets and makes optical coupling unattainable. Through extensive trial and error, we found that an offset distance of approximately 3μm must be left between the cut direction and waveguide entrance. Then, a lensed optical fiber can be used to efficiently couple light into the photonic chip, as shown in Figure 8.2. Using this setup, we achieved coupling losses as low as 9dB/facet when using a 300 nm inversely tapered waveguide, which rises to 12dB/facet in the absence of inverse tapering (1μm wide waveguide). An image of the alignment marks used for such dicing saw cuts, as well as an SEM image of an inversely-tapered waveguide tip are shown in Figure 8.3.

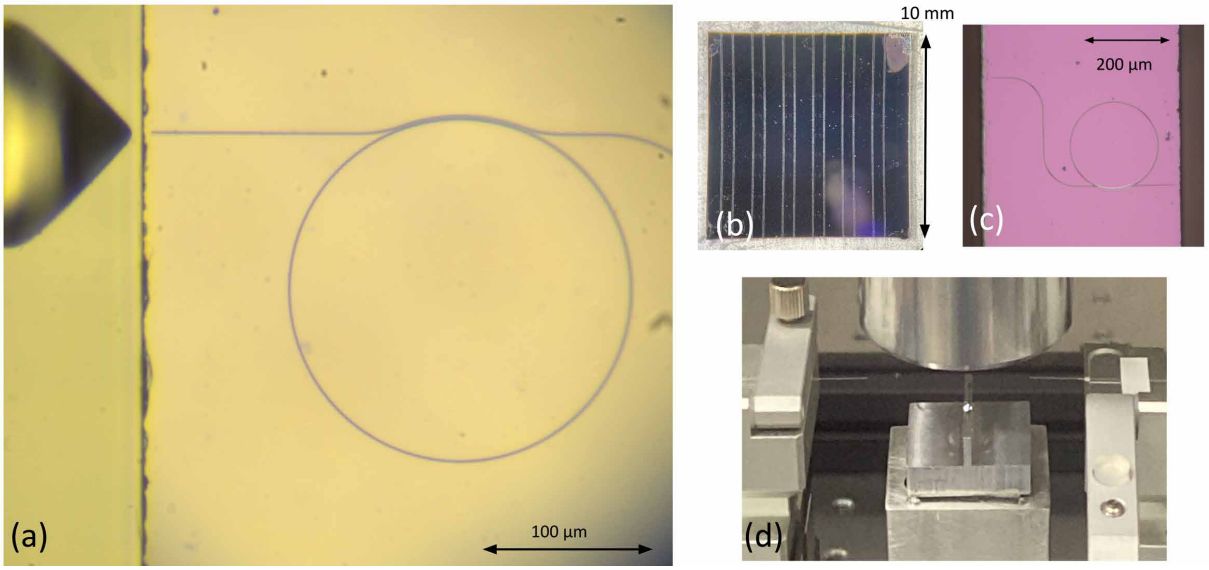

Figure 8.2: Fiber-to-chip edge coupling of light into a lithium niobate chip. (a) Optical microscope view of the final coupling scheme; (b) picture of the 10x10mm sample immediately after dicing with the DAD3220 dicing saw; (c) a single strip of the diced sample, with both edges exposed; (d) a larger view of the setup, with lensed fibers placed on each side of the sample, and positioned on precise motor stages for fine alignment.

It is important to stress that successful coupling was only achieved once the optimization of plasma etching processes enabled etching depths above 200 nm. This is likely due to the very large spatial mode mismatch between optical fibers and shallow-etched waveguides of this kind. Additionally, shallow-etching implies a relatively thick leftover LN layer, which can act as a "slab" waveguide whose modes will interact undesirably with the fabricated rectangular waveguide.

Mechanical polishing of the sample edges was also extensively tried, both as a stand-alone process and as a complementary one to the dicing-saw cuts. Here, the samples are glued to an aluminum holder using thermally sensitive crystal wax, such that the facet to be etched faces upward. The sample is then pressed against fiber-polishing sandpaper (with micrometer

roughness) by ~1kg aluminum cylinders placed on top of the holder. The sandpaper is attached to a rotation motor, thereby achieving the mechanical polishing and etching of the sample. We found that this process does not lead to measurable improvement in coupling efficiency, and very often damages the sample.

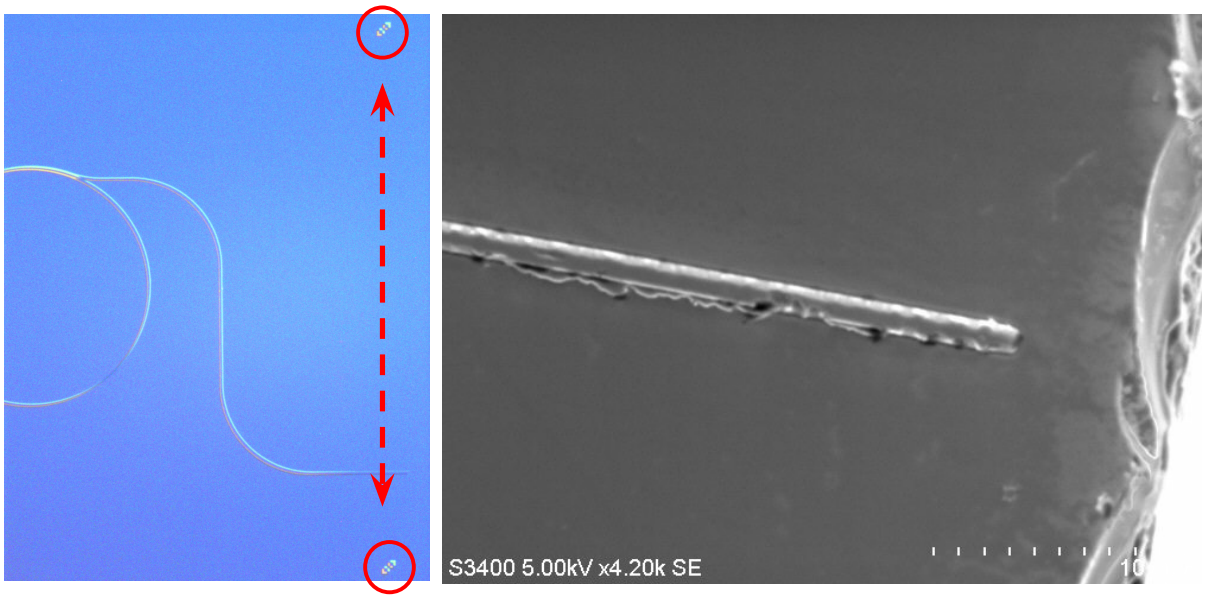

Figure 8.3: Optical microscope image of a photonic device, where highlighted alignment marks are used as a reference for dicing saw cuts. On the right, an SEM image of the diced waveguide (visible contamination is due to the protective resist layer coated prior to dicing, an additional cleaning step is required before optical measurement).

8.3 Measuring Q-factors

The results of this first measurement are shown in Figure 8.5, where a frequency sweep was conducted with a TOPTICA diode laser between 1530 nm and 1550 nm. The image shows the expected Lorentzian resonances associated with the ring resonators. Lorentzian curves were fitted to the results to obtain estimates for the quality factor of the optical cavities, which range from 2 to 6×10^3. These are plotted as functions of geometrical features in Figure 8.4. As expected, smaller gap sizes are associated with smaller quality factors, due to increased coupling between ring resonator and waveguide. So far, the highest quality factor measured in one of our devices has been $Q\approx2.0\times10^4$.

By itself, the measurement shown in Figure 8.5 is not sufficient to separate the contributions of internal and coupling losses to the quality factor. Nevertheless, the results in Figure 8.4, where the quality factor reliably increases as the gap size (between waveguide and

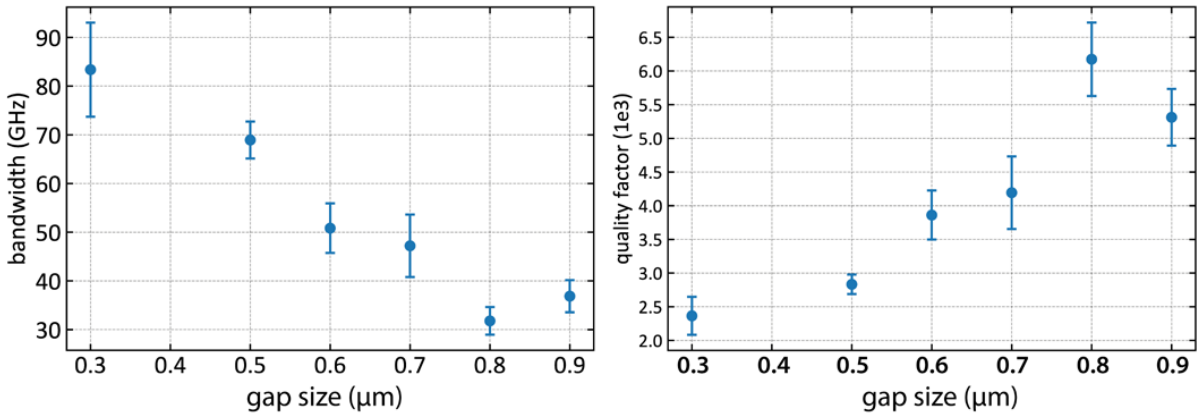

Figure 8.4: Estimated quality factor of a subset of the characterized ring resonators as a function of the gap size (defined as the distance between the outer radius of the ring and the closest waveguide sidewall in the coupler region).

ring) increases, strongly indicate that the optical resonators measured so far are strongly over-coupled. Indeed, these devices were fabricated with very large coupling regions (subtending a 40° arc along the ring), such that the coupling strength can greatly be reduced by simple design adjustments.

Thus, the $Q=2.0\times10^4$ value must be seen as a lower bound for the quality factor yielded by this process. In addition to the over-coupling indicated by the measurements in Figure 8.4, it must also be stressed that the devices measured do not correspond to the fully optimized recipe. [1] Nevertheless, even the lower bound levels achieved, combined with the developed processes of metal deposition and periodic poling, already enable important demonstrations in nonlinear photonics, such as second harmonic generation.

Furthermore, assuming a worst-case scenario of intrinsic $Q=2.0\times10^4$, we estimate a threshold power around 27 mW [73] to demonstrate on-chip optical parametric oscillation. Assuming coupling losses of 9dB/facet, a pump source of approximately 214 mW would be necessary to complete the demonstrations. This pump power value is reduced to a more achievable 34mW (4.3 mW threshold) for $Q=5.0\times10^4$, which is most likely well within reach.

[1] This is due to the fact that, as shown in the previous chapters, multiple steps are required before a sample is ready to be measured. Thus, not all modifications to the fabrication process could be translated to optical measurement in a timely manner.

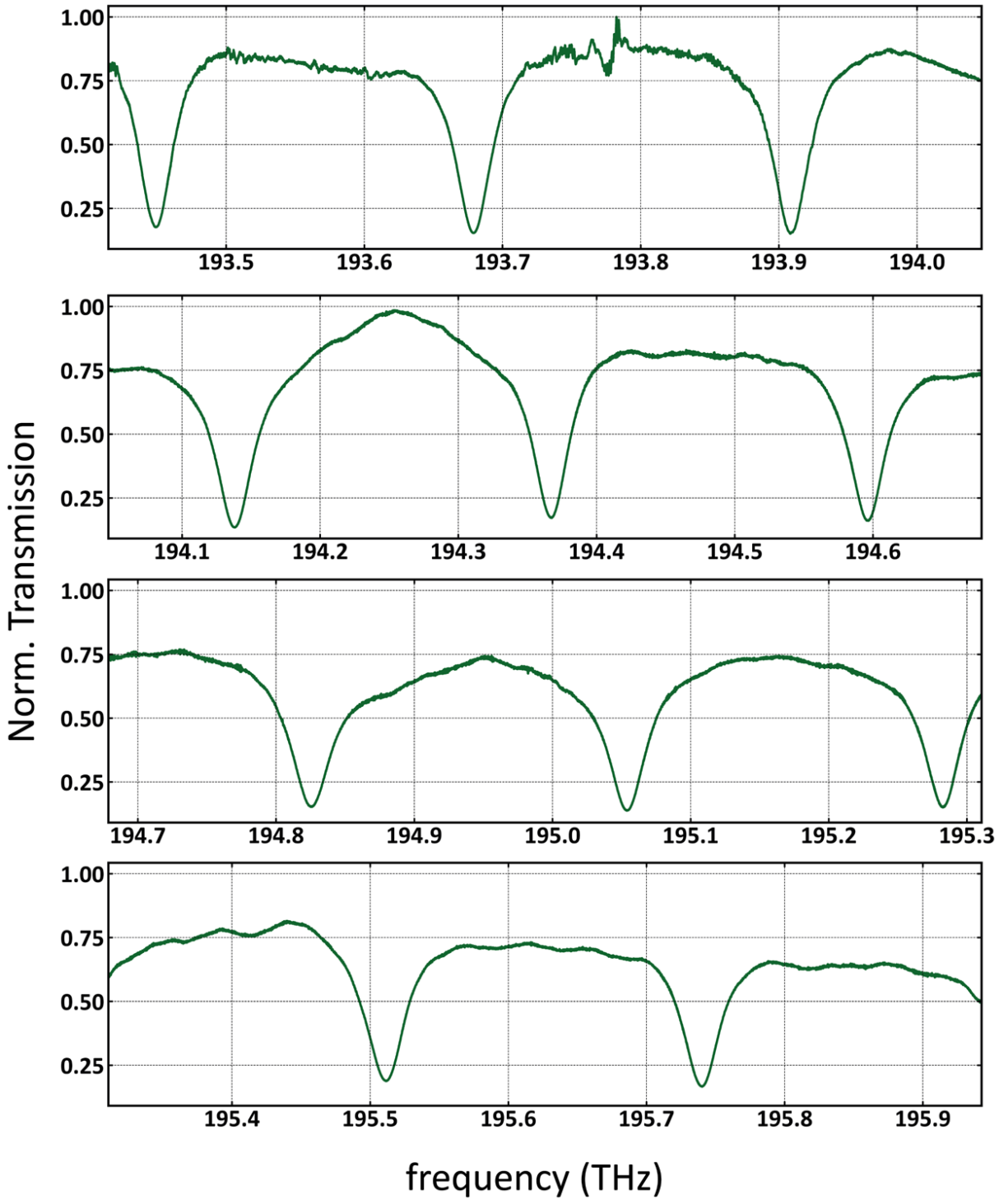

Figure 8.5: Optical Measurement of our first ring resonator in z-cut thin-film lithium niobate, fabricated at LPD (IFGW/Unicamp), CCSNNano (Unicamp) and LNNano (CNPEM). This device consisted in a 100μm-radius ring with 1μm width and 300nm height, coupled to a waveguide with the same dimensions, separated by a distance of 800 nm along a coupling length of approximately 70μm, subtending a 40° arc concentric to the ring.

Chapter 9

Conclusions and Outlook

In this project, we have worked on the design, microfabrication, and optical measurement of integrated photonic devices in thin-film lithium niobate. A complete microfabrication recipe was developed from scratch and multiple processes for TFLN were extensively characterized, enabling high feature resolution, deep-etching of the lithium niobate film, and the preparation of facets for edge coupling. In collaboration with group members, a setup for fiber-to-chip coupling was constructed and tested, and a recipe for periodic poling of lithium niobate with high spatial resolution was optimized. The process is validated by the successful optical measurement of integrated ring resonators, with coupling losses of 9dB/facet and quality factors around 2.0×10^4 in the worst-case scenario. Several complementary cleanroom processes were also developed, including the fabrication of lensed fibers, deep etching of silicon and silicon dioxide, several cleaning procedures, and metal deposition.

These results constitute a robust toolbox for the realization of a wide range of devices and experiments. And in many cases, such experiments correspond to results achieved only very recently in the literature, as seen in Table 5.3. Most notably, on-chip second harmonic generation can be readily implemented in a periodically-poled lithium niobate waveguide using the processes shown in this text.

Subsequent rounds of fabrication are likely to yield significantly higher quality factors, either by implementing the fully optimized fabrication process or simply by removing the devices from the over-coupled regime. In such a scenario, the threshold power for the demonstration of optical parametric oscillation will sit comfortably within reach. Finally, below-threshold operation of the OPO is a benchmark requirement for the on-chip generation of squeezed states of light.

References

[1] E. Pelucchi et al. “The potential and global outlook of integrated photonics for quantum technologies”. en. In: *Nat. Rev. Phys.* (Dec. 2021), pp. 1–15. ISSN: 2522-5820.

[2] T. Rudolph. “Why I am optimistic about the silicon-photonic route to quantum computing”. In: *APL Photonics* 2.3 (Mar. 2017), p. 030901.

[3] G. Moody et al. “2022 Roadmap on integrated quantum photonics”. In: *J. Physics: Photonics* 4.1 (Jan. 2022), p. 012501. ISSN: 2515-7647.

[4] Z. Ma et al. “Ultrabright Quantum Photon Sources on Chip”. In: *Phys. Review Lett.* 125.26 (Dec. 2020), p. 263602.

[5] H. Jin et al. “On-Chip Generation and Manipulation of Entangled Photons Based on Reconfigurable Lithium-Niobate Waveguide Circuits”. en. In: *Phys. Review Lett.* 113.10 (Sept. 2014), p. 103601. ISSN: 0031-9007, 1079-7114.

[6] R. Nehra et al. “Few-cycle vacuum squeezing in nanophotonics”. en. In: *Science* 377.6612 (Sept. 2022), pp. 1333–1337. ISSN: 0036-8075, 1095-9203.

[7] P.-K. Chen, I. Briggs, S. Hou, and L. Fan. “Ultra-broadband quadrature squeezing with thin-film lithium niobate nanophotonics”. en. In: *Opt. Lett.* 47.6 (Mar. 2022), p. 1506. ISSN: 0146-9592, 1539-4794.

[8] V. D. Vaidya et al. “Broadband quadrature-squeezed vacuum and nonclassical photon number correlations from a nanophotonic device”. en. In: *Sci. Adv.* 6.39 (Sept. 2020), eaba9186. ISSN: 2375-2548.

[9] A. Acín et al. “The quantum technologies roadmap: a European community view”. en. In: 20.8 (Aug. 2018), p. 080201. ISSN: 1367-2630.

[10] S. Bogdanov, M. Y. Shalaginov, A. Boltasseva, and V. M. Shalaev. “Material platforms for integrated quantum photonics”. en. In: *Opt. Mater. Express* 7.1 (Jan. 2017), p. 111. ISSN: 2159-3930.

[11] D. Zhu et al. “Integrated photonics on thin-film lithium niobate”. en. In: *Adv. Opt. Photonics* 13.2 (June 2021), p. 242. ISSN: 1943-8206.

[12] A. Boes et al. “Lithium niobate photonics: Unlocking the electromagnetic spectrum”. en. In: *Science* 379.6627 (Jan. 2023), eabj4396. ISSN: 0036-8075, 1095-9203.

[13] D. J. Griffiths. *Introduction to electrodynamics*. Fourth edition. Cambridge, United Kingdom ; New York, NY: Cambridge University Press, 2018. ISBN: 9781108420419.

[14] H. A. Lorentz. *The theory of electrons and its applications to the phenomena of light and radiant heat*. Dover books on physics. New York: Dover Publications, 2011. ISBN: 9780486495583.

[15] R. W. Boyd. *Nonlinear optics*. eng. 3. ed. Amsterdam Heidelberg: Elsevier, Academic Press, 2008. ISBN: 9780080485966 9780123694706.

[16] J. Bergman and S. Kurtz. "Nonlinear optical materials". en. In: *Mater. Sci. Eng.* 5.5 (May 1970), pp. 235–250. ISSN: 00255416.

[17] P. A. Franken, A. E. Hill, C. W. Peters, and G. Weinreich. "Generation of Optical Harmonics". In: *Phys. Review Lett.* 7.4 (Aug. 1961), pp. 118–119.

[18] T. H. Maiman. "Stimulated Optical Radiation in Ruby". en. In: *Nature* 187.4736 (Aug. 1960), pp. 493–494. ISSN: 1476-4687.

[19] B. Corcoran et al. "Ultra-dense optical data transmission over standard fibre with a single chip source". en. In: *Nat. Commun.* 11.1 (May 2020), p. 2568. ISSN: 2041-1723.

[20] P. Marin-Palomo et al. "Microresonator-based solitons for massively parallel coherent optical communications". en. In: *Nature* 546.7657 (June 2017), pp. 274–279. ISSN: 1476-4687.

[21] H. Telle et al. "Carrier-envelope offset phase control: A novel concept for absolute optical frequency measurement and ultrashort pulse generation". en. In: *Appl. Phys. B* 69.4 (Oct. 1999), pp. 327–332. ISSN: 1432-0649.

[22] C. R. Pollock and M. Lipson. *Integrated photonics*. Boston: Kluwer Academic, 2003. ISBN: 9781402076350.

[23] E. A. J. Marcatili. "Dielectric Rectangular Waveguide and Directional Coupler for Integrated Optics". en. In: *Bell System Tech. J.* 48.7 (Sept. 1969), pp. 2071–2102. ISSN: 00058580.

[24] G. Lifante. *Integrated photonics: fundamentals*. Hoboken, NJ: J. Wiley, 2003. ISBN: 9780470848685.

[25] T. Suhara and M. Fujimura. *Waveguide nonlinear-optic devices*. English. Berlin; London: Springer, 2011. ISBN: 9783642056857.

[26] R. Eckardt, H. Masuda, Y. Fan, and R. Byer. "Absolute and relative nonlinear optical coefficients of KDP, KD*P, BaB/sub 2/O/sub 4/, LiIO/sub 3/, MgO:LiNbO/sub 3/, and KTP measured by phase-matched second-harmonic generation". In: *IEEE J. Quantum Electron.* 26.5 (May 1990), pp. 922–933. ISSN: 00189197.

[27] Y. Zheng, H. Ren, W. Wan, and X. Chen. "Time-reversed wave mixing in nonlinear optics". en. In: *Sci. Reports* 3.1 (Nov. 2013), p. 3245. ISSN: 2045-2322.

[28] M. Yamada and M. Saitoh. "Fabrication of a periodically poled laminar domain structure with a pitch of a few micrometers by applying an external electric field". en. In: *J. Appl. Phys.* 84.4 (Aug. 1998), pp. 2199–2206. ISSN: 0021-8979, 1089-7550.

[29] M. Younesi et al. "Periodic poling with a micrometer-range period in thin-film lithium niobate on insulator". EN. In: *JOSA B* 38.3 (Mar. 2021), pp. 685–691. ISSN: 1520-8540.

[30] B. N. Slautin, H. Zhu, and V. Y. Shur. "Submicron periodical poling in Z-cut lithium niobate thin films". In: *Ferroelectrics* 576.1 (May 2021), pp. 119–128. ISSN: 0015-0193.

[31] S. E. Smith. "Investigation of nanoscale etching and poling of lithium niobate". en. Thesis. Montana State University - Bozeman, College of Engineering, 2014.

[32] R. Loudon. *The quantum theory of light*. 3rd ed. Oxford science publications. Oxford ; New York: Oxford University Press, 2000. ISBN: 9780198501770 9780198501763.

[33] G. S. Agarwal. *Quantum optics*. Cambridge, UK: Cambridge University Press, 2013. ISBN: 9781107006409.

[34] J. J. Sakurai. *Modern Quantum Mechanics*. 3rd. Reading, Mass.: Addison-Wesley, 1994.

[35] M. O. Scully and M. S. Zubairy. *Quantum Optics*. Cambridge: Cambridge University Press, 1997. ISBN: 9780521435956.

[36] J. D. Jackson. *Classical electrodynamics*. 3rd ed. New York: Wiley, 1999. ISBN: 9780471309321.

[37] R. J. Glauber. "Coherent and Incoherent States of the Radiation Field". In: *Phys. Review* 131.6 (Sept. 1963), pp. 2766–2788.

[38] R. J. Glauber. "The Quantum Theory of Optical Coherence". In: *Phys. Review* 130.6 (June 1963), pp. 2529–2539.

[39] M. Fox. *Quantum optics: an introduction*. Oxford master series in physics 15. Oxford ; New York: Oxford University Press, 2006. ISBN: 9780198566724 9780198566731.

[40] H. P. Robertson. "The Uncertainty Principle". en. In: *Phys. Review* 34.1 (July 1929), pp. 163–164. ISSN: 0031-899X.

[41] V. Vedral. *Introduction to quantum information science*. Oxford graduate texts. OCLC: ocm70173203. Oxford: Oxford University Press, 2006. ISBN: 9780199215706 9780198571193.

[42] M. A. Nielsen and I. L. Chuang. *Quantum computation and quantum information*. 10th anniversary ed. Cambridge ; New York: Cambridge University Press, 2010. ISBN: 9781107002173.

[43] C. W. Gardiner and P. Zoller. *Quantum noise: a handbook of Markovian and non-Markovian quantum stochastic methods with applications to quantum optics*. eng. Third edition. OCLC: 903068139. Berlin: Springer, 2010. ISBN: 9783642060946.

[44] J. Aasi et al. "Enhanced sensitivity of the LIGO gravitational wave detector by using squeezed states of light". en. In: *Nat. Photonics* 7.8 (Aug. 2013), pp. 613–619. ISSN: 1749-4885, 1749-4893.

[45] T. Aoki et al. "Quantum error correction beyond qubits". en. In: *Nat. Phys.* 5.8 (Aug. 2009), pp. 541–546. ISSN: 1745-2473, 1745-2481.

[46] T. Kashiwazaki et al. "Over-8-dB squeezed light generation by a broadband waveguide optical parametric amplifier toward fault-tolerant ultra-fast quantum computers". en. In: *Appl. Phys. Lett.* 122.23 (June 2023), p. 234003. ISSN: 0003-6951, 1077-3118.

[47] U. L. Andersen, T. Gehring, C. Marquardt, and G. Leuchs. "30 years of squeezed light generation". In: *Physica Scripta* 91.5 (May 2016), p. 053001. ISSN: 0031-8949, 1402-4896.

[48] A. I. Lvovsky. "Squeezed Light". en. In: *Photonics*. John Wiley & Sons, Ltd, 2015, pp. 121–163. ISBN: 9781119009719.

[49] R. E. Slusher et al. "Observation of Squeezed States Generated by Four-Wave Mixing in an Optical Cavity". In: *Phys. Review Lett.* 55.22 (Nov. 1985), pp. 2409–2412.

[50] L.-A. Wu, H. J. Kimble, J. L. Hall, and H. Wu. "Generation of Squeezed States by Parametric Down Conversion". In: *Phys. Review Lett.* 57.20 (Nov. 1986), pp. 2520–2523.

[51] L.-A. Wu, M. Xiao, and H. J. Kimble. "Squeezed states of light from an optical parametric oscillator". EN. In: *JOSA B* 4.10 (Oct. 1987), pp. 1465–1475. ISSN: 1520-8540.

[52] C. Couteau. "Spontaneous parametric down-conversion". en. In: *Contemp. Phys.* 59.3 (July 2018), pp. 291–304. ISSN: 0010-7514, 1366-5812.

[53] J. A. Giordmaine and R. C. Miller. "Tunable Coherent Parametric Oscillation in LiNbO3 at Optical Frequencies". In: *Phys. Review Lett.* 14 (June 1965), pp. 973–976. ISSN: 0031-9007.

[54] N. Ismail, C. C. Kores, D. Geskus, and M. Pollnau. "Fabry-Pérot resonator: spectral line shapes, generic and related Airy distributions, linewidths, finesses, and performance at low or frequency-dependent reflectivity". en. In: *Opt. Express* 24.15 (July 2016), p. 16366. ISSN: 1094-4087.

[55] F. A. S. Barbosa. "Robustez do emaranhamento em variáveis contínuas e fotodetecção de feixes intensos no domínio espectral". pt-br. text. Universidade de São Paulo, June 2013.

[56] G. Brooker. *Modern classical optics*. Oxford master series in physics 8. OCLC: ocm52829216. Oxford ; New York: Oxford University Press, 2003. ISBN: 9780198599654 9780198599647.

[57] C. R. Locke, D. Stuart, E. N. Ivanov, and A. N. Luiten. "A simple technique for accurate and complete characterisation of a Fabry-Perot cavity". en. In: *Opt. Express* 17.24 (Nov. 2009), p. 21935. ISSN: 1094-4087.

[58] T. Debuisschert, A. Sizmann, E. Giacobino, and C. Fabre. "Type-II continuous-wave optical parametric oscillators: oscillation and frequency-tuning characteristics". EN. In: *JOSA B* 10.9 (Sept. 1993), pp. 1668–1680. ISSN: 1520-8540.

[59] A. Marandi, N. C. Leindecker, K. L. Vodopyanov, and R. L. Byer. "All-optical quantum random bit generation from intrinsically binary phase of parametric oscillators". en. In: *Opt. Express* 20.17 (Aug. 2012), p. 19322. ISSN: 1094-4087.

[60] L. S. Madsen et al. "Continuous variable quantum key distribution with modulated entangled states". en. In: *Nat. Commun.* 3.1 (Sept. 2012), p. 1083. ISSN: 2041-1723.

[61] T. Inagaki et al. "Large-scale Ising spin network based on degenerate optical parametric oscillators". en. In: *Nat. Photonics* 10.6 (June 2016), pp. 415–419. ISSN: 1749-4885, 1749-4893.

[62] Y. Yamamoto et al. "Coherent Ising machines—optical neural networks operating at the quantum limit". en. In: *npj Quantum Inf.* 3.1 (Dec. 2017), p. 49. ISSN: 2056-6387.

[63] B. T. Matthias and J. P. Remeika. "Ferroelectricity in the Ilmenite Structure". In: *Phys. Review* 76.12 (Dec. 1949), pp. 1886–1887.

[64] M. Manzo, F. Laurell, V. Pasiskevicius, and K. Gallo. "Lithium Niobate: The Silicon of Photonics!" In: *Nano-Optics for Enhancing Light-Matter Interactions on a Molecular Scale*. Ed. by B. Di Bartolo and J. Collins. Dordrecht: Springer Netherlands, 2013, pp. 421–422. ISBN: 9789400753129 9789400753136.

[65] X. Liu, A. W. Bruch, and H. X. Tang. "Aluminum nitride photonic integrated circuits: from piezo-optomechanics to nonlinear optics". en. In: *Adv. Opt. Photonics* 15.1 (Mar. 2023), p. 236. ISSN: 1943-8206.

[66] F. Boitier et al. "Electrically Injected Photon-Pair Source at Room Temperature". In: *Phys. Review Lett.* 112.18 (May 2014), p. 183901.

[67] I. Kaminow and J. Carruthers. "Optical waveguiding layers in LiNbO3 and LiTaO3". en. In: *Appl. Phys. Lett.* 22.7 (Apr. 1973), pp. 326–328. ISSN: 0003-6951, 1077-3118.

[68] J. L. Jackel, C. E. Rice, and J. J. Veselka. "Proton exchange for high-index waveguides in LiNbO3". en. In: *Appl. Phys. Lett.* 41.7 (Oct. 1982), pp. 607–608. ISSN: 0003-6951, 1077-3118.

[69] P. Rabiei and P. Gunter. "Optical and electro-optical properties of submicrometer lithium niobate slab waveguides prepared by crystal ion slicing and wafer bonding". en. In: *Appl. Phys. Lett.* 85.20 (Nov. 2004), pp. 4603–4605. ISSN: 0003-6951, 1077-3118.

[70] H. Hu, R. Ricken, and W. Sohler. "Lithium niobate photonic wires". en. In: *Opt. Express* 17.26 (Dec. 2009), p. 24261. ISSN: 1094-4087.

[71] A. Rao et al. "Second-harmonic generation in periodically-poled thin film lithium niobate wafer-bonded on silicon". en. In: *Opt. Express* 24.26 (Dec. 2016), p. 29941. ISSN: 1094-4087.

[72] Q. Wang and J. Xiao. "Compact and efficient polarization rotator using laterally asymmetric rib waveguides on a lithium-niobate-on-insulator platform". en. In: *Appl. Opt.* 62.18 (June 2023), p. 5042. ISSN: 1559-128X, 2155-3165.

[73] J. Lu, A. A. Sayem, et al. "Ultralow-threshold thin-film lithium niobate optical parametric oscillator". EN. In: *Optica* 8.4 (Apr. 2021), pp. 539–544. ISSN: 2334-2536.

[74] A. Shams-Ansari et al. "Reduced material loss in thin-film lithium niobate waveguides". en. In: *APL Photonics* 7.8 (Aug. 2022), p. 081301. ISSN: 2378-0967.

[75] E. Wooten et al. "A review of lithium niobate modulators for fiber-optic communications systems". In: *IEEE J. Sel. Top. Quantum Electron.* 6.1 (Jan. 2000), pp. 69–82. ISSN: 1077-260X, 1558-4542.

[76] T.-C. Lee et al. "Surface acoustic wave applications of lithium niobate thin films". en. In: *Appl. Phys. Lett.* 82.2 (Jan. 2003), pp. 191–193. ISSN: 0003-6951, 1077-3118.

[77] M. A. Fakhri et al. “Lithium niobate – Based sensors: A review”. In: Chiang Mai, Thailand, 2022, p. 020124.

[78] G. E. Moore. “Cramming more components onto integrated circuits, Reprinted from Electronics, volume 38, number 8, April 19, 1965, pp.114 ff.” In: *IEEE Solid-State Circuits Soc. Newsl.* 11.3 (Sept. 2006), pp. 33–35. ISSN: 1098-4232.

[79] M. J. Madou. *Fundamentals of microfabrication: the science of miniaturization*. eng. 2. ed. Boca Raton, Fla.: CRC Press, 2002. ISBN: 9780849308260.

[80] L. Song et al. “Fully adiabatic polarization rotator-splitter based on thin-film lithium niobate platform”. en. In: *Opt. Express* 31.12 (June 2023), p. 19604. ISSN: 1094-4087.

[81] H. Han and B. Xiang. “Simulation and analysis of electro-optic tunable microring resonators in silicon thin film on lithium niobate”. en. In: *Sci. Reports* 9.1 (Apr. 2019), p. 6302. ISSN: 2045-2322.

[82] D. Jundt, M. Fejer, and R. Byer. “Optical properties of lithium-rich lithium niobate fabricated by vapor transport equilibration”. In: *IEEE J. Quantum Electron.* 26.1 (Jan. 1990), pp. 135–138. ISSN: 00189197.

[83] D. H. Jundt. “Temperature-dependent Sellmeier equation for the index of refraction, n_e, in congruent lithium niobate”. en. In: *Opt. Lett.* 22.20 (Oct. 1997), p. 1553. ISSN: 0146-9592, 1539-4794.

[84] A. E. Tekkaya and C. Soyarslan. “Finite Element Method”. en. In: *CIRP Encyclopedia of Production Engineering*. Ed. by L. Laperrière and G. Reinhart. Berlin, Heidelberg: Springer, 2014, pp. 508–514. ISBN: 9783642206177.

[85] S. G. Johnson. “Notes on Perfectly Matched Layers (PMLs)”. In: (2021).

[86] M. Zhang et al. “Monolithic ultra-high-Q lithium niobate microring resonator”. en. In: *Optica* 4.12 (Dec. 2017), p. 1536. ISSN: 2334-2536.

[87] L. Martin et al. “Multiple pass exposure in e-beam lithography: application to the sub-22nm nodes”. In: ed. by D. J. C. Herr. San Jose, California, Mar. 2010, 76370E.

[88] Z. Ren et al. “Etching characteristics of LiNbO3 in reactive ion etching and inductively coupled plasma”. en. In: *J. Appl. Phys.* 103.3 (Feb. 2008), p. 034109. ISSN: 0021-8979, 1089-7550.

[89] G. Ulliac, V. Calero, et al. “Argon plasma inductively coupled plasma reactive ion etching study for smooth sidewall thin film lithium niobate waveguide application”. en. In: *Opt. Mater.* 53 (Mar. 2016), pp. 1–5. ISSN: 09253467.

[90] H. Hu, A. P. Milenin, et al. “Plasma etching of proton-exchanged lithium niobate”. en. In: *J. Vac. Sci. & Technol. A: Vacuum, Surfaces, Films* 24.4 (July 2006), pp. 1012–1015. ISSN: 0734-2101, 1520-8559.

[91] J. Deng, G. Si, and A. J. Danner. “Dry etching of LiNbO3 using inductively coupled plasma”. In: *2010 Photonics Global Conference*. Dec. 2010, pp. 1–5.

[92] G. Ulliac, B. Guichardaz, et al. "Ultra-smooth LiNbO3 micro and nano structures for photonic applications". en. In: *Microelectron. Eng.* Proceedings of the 36th International Conference on Micro- and Nano-Engineering (MNE) 88.8 (Aug. 2011), pp. 2417–2419. ISSN: 0167-9317.

[93] C.-M. Chang et al. "A parametric study of ICP-RIE etching on a lithium niobate substrate". In: *10th IEEE International Conference on Nano/Micro Engineered and Molecular Systems*. Apr. 2015, pp. 485–486.

[94] Y. Gao et al. *Compact lithium niobate photonic integrated circuits*. Mar. 2023.

[95] S. Benchabane et al. "Highly selective electroplated nickel mask for lithium niobate dry etching". en. In: *J. Appl. Phys.* 105.9 (May 2009), p. 094109. ISSN: 0021-8979, 1089-7550.

[96] *HSQ / FOX16 resists*. en-GB.

[97] *HSQ essential tips | Yale Institute for Nanoscience and Quantum Engineering*.

[98] A. A. Osipov et al. "Deep Etching of LiNbO3 Using Inductively Coupled Plasma in SF6-Based Gas Mixture". In: *J. Microelectromechanical Syst.* 30.1 (Feb. 2021), pp. 90–95. ISSN: 1941-0158.

[99] R. Zhuang, J. He, Y. Qi, and Y. Li. "High- Q Thin-Film Lithium Niobate Microrings Fabricated with Wet Etching". en. In: *Adv. Mater.* 35.3 (Jan. 2023), p. 2208113. ISSN: 0935-9648, 1521-4095.

[100] J. Zhao. "Periodic poling of thin-film lithium niobate for second-harmonic generation and entangled photon-pair generation". en. PhD thesis. UC San Diego, 2020.

[101] C. L. Sones et al. "Differential etch rates in z-cut LiNbO3 for variable HF/HNO3 concentrations". In: *J. Mater. Chem.* 12.2 (Jan. 2002), pp. 295–298. ISSN: 09599428, 13645501.

[102] A. B. Randles, M. Esashi, and S. Tanaka. "Etch rate dependence on crystal orientation of lithium niobate". In: *IEEE Trans. on Ultrason. Ferroelectr. Freq. Control* 57.11 (Nov. 2010), pp. 2372–2380. ISSN: 0885-3010.

[103] J. Lu, J. B. Surya, et al. "Periodically poled thin-film lithium niobate microring resonators with a second-harmonic generation efficiency of 250,000%/W". EN. In: *Optica* 6.12 (Dec. 2019), pp. 1455–1460. ISSN: 2334-2536.

[104] I. Krasnokutska, J.-L. J. Tambasco, and A. Peruzzo. "Nanostructuring of LNOI for efficient edge coupling". en. In: *Opt. Express* 27.12 (June 2019), p. 16578. ISSN: 1094-4087.

[105] R. Marchetti et al. "Coupling strategies for silicon photonics integrated chips [Invited]". EN. In: *Photonics Research* 7.2 (Feb. 2019), pp. 201–239. ISSN: 2327-9125.

[106] B. Chen et al. "Low-loss fiber grating coupler on thin film lithium niobate platform". en. In: *APL Photonics* 7.7 (July 2022), p. 076103. ISSN: 2378-0967.

[107] V. R. Almeida, R. R. Panepucci, and M. Lipson. "Nanotaper for compact mode conversion". en. In: *Opt. Lett.* 28.15 (Aug. 2003), p. 1302. ISSN: 0146-9592, 1539-4794.

[108] N. Yao et al. “Efficient light coupling between an ultra-low loss lithium niobate waveguide and an adiabatically tapered single mode optical fiber”. en. In: *Opt. Express* 28.8 (Apr. 2020), p. 12416. ISSN: 1094-4087.

[109] C. Hu et al. “High-efficient coupler for thin-film lithium niobate waveguide devices”. en. In: *Opt. Express* 29.4 (Feb. 2021), p. 5397. ISSN: 1094-4087.

[110] L. He et al. “Low-loss fiber-to-chip interface for lithium niobate photonic integrated circuits”. en. In: *Opt. Lett.* 44.9 (May 2019), p. 2314. ISSN: 0146-9592, 1539-4794.

[111] Lu, Juanjuan et al. “Supplementary document for Ultralow-threshold thin-film lithium niobate optical parametric oscillator - 5149061.pdf”. In: (2021), 6716217 Bytes.

[112] F. Baboux, G. Moody, and S. Ducci. “Nonlinear integrated quantum photonics with AlGaAs”. en. In: *Optica* 10.7 (July 2023), p. 917. ISSN: 2334-2536.

[113] X. Mu, S. Wu, L. Cheng, and H. Fu. “Edge Couplers in Silicon Photonic Integrated Circuits: A Review”. en. In: *Appl. Sci.* 10.4 (Feb. 2020), p. 1538. ISSN: 2076-3417.

[114] J. Cardenas et al. “High Coupling Efficiency Etched Facet Tapers in Silicon Waveguides”. In: *IEEE Photonics Technol. Lett.* 26.23 (Dec. 2014), pp. 2380–2382. ISSN: 1041-1135, 1941-0174.

Appendix A

Perturbative Nonlinear Rectangular Waveguide

We begin by considering a mode propagating in a waveguide not exhibiting nonlinearity and write it as

$$\mathbf{E}^{(0)} = \mathbf{E}_m(x,y)\exp(-i\beta_m z) \quad \text{and} \quad \mathbf{H}^{(0)} = \mathbf{H}_m(x,y)\exp -i\beta_m z \tag{A.1}$$

ignoring the normalization for now. Additionally, we consider the guided modes

$$\mathbf{E}(\mathbf{r}) = \sum_m A_m(z,\omega)\mathbf{E}_m(x,y)\exp -i\beta_m z \quad \text{and} \quad \mathbf{H}(\mathbf{r}) = \sum_m A_m(z,\omega)\mathbf{H}_m(x,y)\exp -i\beta_m z \tag{A.2}$$

where the $A(z,\omega)$ is a dimensionless factor used to account for the z dependence of the electric and magnetic fields, since we anticipate that the presence of the nonlinearity will cause different modes to become coupled.

The set of equations obeyed by these quantities is similar to the previous example, but now we add the polarization, such that

$$\begin{cases} \nabla\times\mathbf{E}^{(0)^*} = i\omega\mu_0\mathbf{H}^{(0)^*} \\ \nabla\times\mathbf{H}^{(0)^*} = -i\omega\epsilon_0\epsilon\mathbf{E}^{(0)^*} \\ \nabla\times\mathbf{E} = -i\omega\mu_0\mathbf{H} \\ \nabla\times\mathbf{H} = i\omega\left(\epsilon_0\epsilon\mathbf{E}+\mathbf{P}_{NL}\right) \end{cases} \Rightarrow \begin{cases} \mathbf{H}\cdot(\nabla\times\mathbf{E}^{(0)^*}) = i\omega\mu_0\mathbf{H}^{(0)^*}\cdot\mathbf{H} \\ \mathbf{E}\cdot(\nabla\times\mathbf{H}^{(0)^*}) = -i\omega\epsilon_0\epsilon\mathbf{E}^{(0)^*}\cdot\mathbf{E} \\ \mathbf{H}^{(0)}\cdot(\nabla\times\mathbf{E}) = -i\omega\mu_0\mathbf{H}\cdot\mathbf{H}^{(0)} \\ \mathbf{E}^{(0)}\cdot(\nabla\times\mathbf{H}) = i\omega\left(\epsilon_0\epsilon\mathbf{E}+\mathbf{P}_{NL}\right)\cdot\mathbf{E}^{(0)} \end{cases} \tag{A.3}$$

A quick comment is due on the P_{NL} notation. Note that

$$\mathbf{D} = \varepsilon_0\mathbf{E} + \mathbf{P} = \varepsilon_0(1+\chi_e)\mathbf{E} = \varepsilon_0\varepsilon\mathbf{E} \quad \text{s.t.} \quad \mathbf{P} = \varepsilon_0\left(\chi^{(1)}\mathbf{E}(t) + \chi^{(2)}\mathbf{E}^2(t) + \dots\right) \tag{A.4}$$

which is to say that one may either write

$$\mathbf{D} = \varepsilon_0\mathbf{E} + \mathbf{P} \quad \text{OR} \quad \mathbf{D} = \varepsilon_0\varepsilon\mathbf{E} + \mathbf{P}_{NL} \tag{A.5}$$

And following the same procedure as before, we get to

$$\nabla \cdot \left(\mathbf{E} \times \mathbf{H}^{(0)^*} + \mathbf{E}^{(0)^*} \times \mathbf{H}\right) = -i\omega\mathbf{E}^{(0)^*} \cdot \mathbf{P}_{NL}. \tag{A.6}$$

Integrating this result in a volume parallel to the xy plane with infinitely small thickness and infinite area, we get

$$\iiint_V \nabla \cdot \left(\mathbf{E} \times \mathbf{H}^{(0)^*} + \mathbf{E}^{(0)^*} \times \mathbf{H}\right)\, dV = -i\omega \iiint_V \mathbf{E}^{(0)^*} \cdot \mathbf{P}_{NL}\, dV \tag{A.7}$$

Separating the divergence in two terms,

$$\iiint_V \left[\nabla_{(x,y)} \cdot \left(\mathbf{E} \times \mathbf{H}^{(0)^*} + \mathbf{E}^{(0)^*} \times \mathbf{H}\right)_{(x,y)}\right] + \iiint_V \frac{\partial}{\partial z}\left(\mathbf{E} \times \mathbf{H}^{(0)^*} + \mathbf{E}^{(0)^*} \times \mathbf{H}\right) \cdot \hat{\mathbf{z}}\, dV = \\ = -i\omega \iiint_V \mathbf{E}^{(0)^*} \cdot \mathbf{P}_{NL}\, dV$$

And applying the divergence theorem to the integral containing the (x, y) components,

$$\oiint_{\partial V} \left[\left(\mathbf{E} \times \mathbf{H}^{(0)^*} + \mathbf{E}^{(0)^*} \times \mathbf{H}\right)_{(x,y)}\right] \cdot d\mathbf{S} + \iiint_V \frac{\partial}{\partial z}\left(\mathbf{E} \times \mathbf{H}^{(0)^*} + \mathbf{E}^{(0)^*} \times \mathbf{H}\right) \cdot \hat{\mathbf{z}}\, dV = \\ = -i\omega \iiint_V \mathbf{E}^{(0)^*} \cdot \mathbf{P}_{NL}\, dV$$

Since the guided modes go to zero at infinity, the first integral will vanish, for the same reason as before. And considering infinitely small thickness, we may rewrite the equation as

$$\iint_S \frac{\partial}{\partial z}\left(\mathbf{E} \times \mathbf{H}^{(0)^*} + \mathbf{E}^{(0)^*} \times \mathbf{H}\right) \cdot \hat{\mathbf{z}}\, dS = -i\omega \iint_S \mathbf{E}^{(0)^*} \cdot \mathbf{P}_{NL}\, dS \tag{A.8}$$

The only fields that will contribute to the cross product so as not to get a zero projection on $\hat{\mathbf{z}}$ will be transverse, so

$$\iint_S \frac{\partial}{\partial z}\left(\mathbf{E}_T \times \mathbf{H}_T^{(0)^*} + \mathbf{E}_T^{(0)^*} \times \mathbf{H}_T\right) \cdot \hat{\mathbf{z}}\, dS = -i\omega \iint_S \mathbf{E}^{(0)^*} \cdot \mathbf{P}_{NL}\, dS \tag{A.9}$$

Notice that T subscript is just a short notation for the (x, y) argument. And by substituting the definitions of the fields, denoting the non-perturbed mode by n and the perturbed mode by m,

$$\sum_m \frac{\partial}{\partial z}\left(A_m(z,\omega)e^{-i(\beta_m-\beta_n)z} \iint \left[\left(\mathbf{E}_{T,m} \times \mathbf{H}_{T,n}^* + \mathbf{E}_{T,n}^* \times \mathbf{H}_{T,m}\right) \cdot \hat{\mathbf{z}}\right] dx\, dy\right) = \\ = -i\omega \iint_S \mathbf{E}_m^*(x,y)e^{i\beta_m z} \cdot \mathbf{P}_{NL}\, dS \tag{A.10}$$

and using the mode orthogonality condition, all terms in the summation will vanish, except for when $m = n$,

$$\frac{\partial}{\partial z}A_m(z,\omega) = -\frac{i\omega}{4P_m}e^{i\beta_m z} \iint_S \mathbf{E}_m^*(x,y,\omega) \cdot \mathbf{P}_{NL}(x,y,\omega)\, dx\, dy \tag{A.11}$$